A COMPARISON BETWEEN UAV-RGB AND ALOS-2 PALSAR-2 IMAGES FOR THE ASSESSMENT OF ABOVEGROUND BIOMASS IN A TEMPERATE FOREST

HASAN AHMED

June, 2021

SUPERVISORS:

Ir. L.M. van Leeuwen – de Leeuw
Dr. M. Schlund

ADVISOR:

Dr. Y. A. Hussin

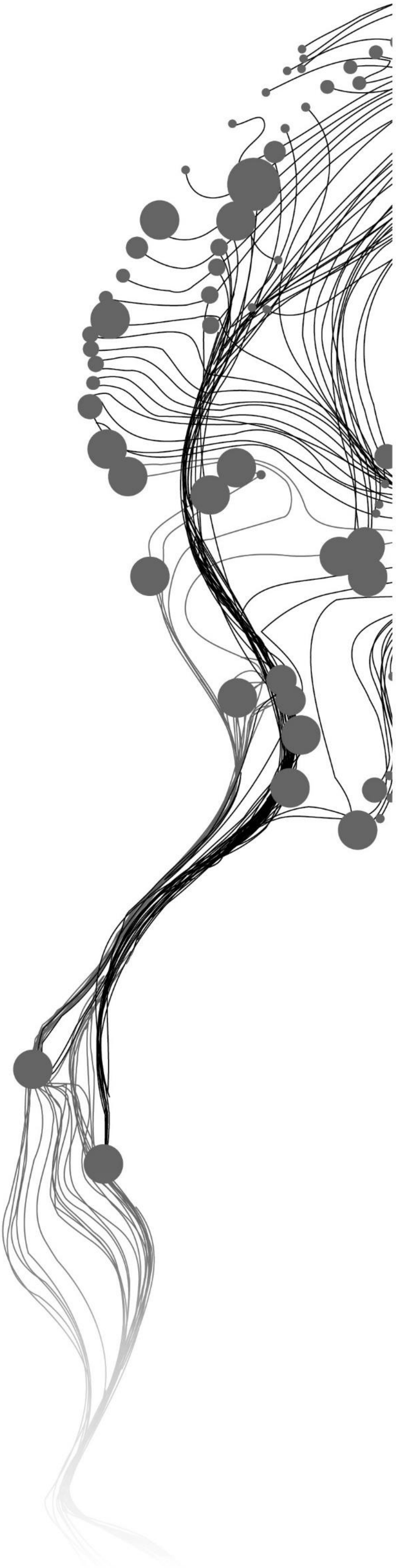

A COMPARISON BETWEEN UAV-RGB AND ALOS-2 PALSAR-2 IMAGES FOR THE ASSESSMENT OF ABOVEGROUND BIOMASS IN A TEMPERATE FOREST

HASAN AHMED

Enschede, The Netherlands, [June, 2021]

Thesis submitted to the Faculty of Geo-Information Science and Earth Observation of the University of Twente in partial fulfilment of the requirements for the degree of Master of Science in Geo-information Science and Earth Observation.
Specialization: Natural Resources Management

SUPERVISORS:
Ir. L.M. van Leeuwen – de Leeuw
Dr. M. Schlund

ADVISOR:
Dr. Y. A. Hussin

THESIS ASSESSMENT BOARD:
Prof. Dr. A.D. Nelson (Chair)
Dr. T. Kauranne (External Examiner, Lappeenranta-Lahti University of Technology, Finland)

ABSTRACT

Forests play a significant role in global warming mitigation strategies. The Netherlands and other nations committed to reducing global warming must assess and monitor forest biomass/carbon. National forest carbon inventories are mostly based on the estimation of the aboveground biomass (AGB). Remote sensing methods, in addition to field-based approaches, are applied to assess forest AGB. UAV RGB Orthomosaic and ALOS-2 PALSAR-2 images are two of many remote sensing data to estimate forest AGB. UAV RGB images provide very-high-resolution images that are used to identify tree crowns. Related parameters such as DBH are modeled from those tree crowns, and finally, the AGB of the tree is estimated. However, the UAV RGB sensor is a passive sensor that cannot penetrate the surface of the canopy and does not include trees suppressed by taller trees. Conversely, ALOS-2 PALSAR-2 is an active remote sensing sensor (L-band SAR) that can penetrate the forest's canopy and sometimes reach the top of the soil layer. Therefore, PALSAR-2 backscatter contains information from the forest canopy, trunks and soil. The method to estimate AGB from PALSAR-2 backscatter is straightforward by developing a regression model between the AGB and backscatter coefficients. However, PALSAR-2 provides AGB information in low resolution, and the backscatter saturates with increasing AGB value. Both of the sensors have limitations in assessing area-based AGB of the forest; UAV does not include suppressed trees, and PALSAR-2 gives biomass information at low resolution and is limited by backscatter saturation. In this regard, this study aimed to compare the plot-based forest biomass estimated from UAV and ALOS-2 PALSAR-2 in a temperate forest and assess their accuracy. Forest parameters such as DBH and the height of 1584 trees have been collected from 94 sample plots. AGB of each individual tree was calculated from the parameters collected parameters by using species-specific allometric equations. Plot AGB was derived from the individual tree AGBs. This study used two standard methods of AGB estimation from UAV RGB and ALOS-2 PALSAR-2 images. In the case of UAV RGB images, we delineated the CPA of trees manually and then used the CPA-DBH relationship grouped into conifers and broadleaves to model DBH. Modeled DBH was used in species-specific allometric equations to obtain UAV estimated individual tree AGB. Then the individual tree AGB modeled from UAV RGB images was transformed into plot AGB. On the other hand, HH and HV polarization backscatter coefficients of the PALSAR-2 image were extracted for each plot by setting a 9-pixels (3x3) window and taking the average of the coefficients. Then a regression between field-measured AGB and backscatter coefficients was established to model AGB from the backscatter coefficients. The study found a positive correlation between CPA delineated from UAV RGB and DBH at a coefficient of determination of 0.89 for broadleaves and 0.92 for conifers with RMSE of 4.28 cm and 2.44 cm accordingly. Individual tree AGB estimated from UAV RGB images depicted a strong correlation with biometric AGB (R^2 = 0.81). However, the plot-based AGB estimation resulted in a high amount of underestimation and overestimation in several plots. UAV RGB images modeled plot AGB had a poor correlation with biometric AGB (R^2 = 0.35, RMSE= 57.18 tons/ha). In the case of PALSAR-2, HV backscatter had a better relationship with AGB. The logarithmic relationship between AGB and HV backscatter represented a high correlation at R^2 = 0.85 with RMSE = 40.9 tons/ha. Moreover, this study also found that plot AGB is better estimated from both UAV RGB and ALOS-2 PALSAR-2 images in coniferous forest stand compared to broadleaves and mixed forest stands. Based on our analysis, we concluded that ALOS-2 PALSAR-2 is a better choice over UAV RGB to estimate the area-based AGB of a temperate forest with intermingling crowns and dense canopy. However, we also remarked that UAV RGB could be better in individual tree-based assessment in a non-intermingling crown forest stands and assessing how PALSAR-2 backscatter estimates AGB of an open forest with non-intermingling crowns could lead to a comprehensive conclusion.

Keyword: AGB, UAV, SAR, SfM, CPA, ALOS-2 PALSAR-2

ACKNOWLEDGEMENTS

I would like to express my gratitude to the Faculty of Geo-information Science and Earth Observation (ITC), the University of Twente for the ITC Excellence Scholarship and the Holland Scholarship that supported the finance of my MSc program. I also extend my gratitude to Faculty ITC for providing the financial support for the research and acquiring ALOS-2 PALSAR-2 data from JAXA.

I am deeply thankful to my supervisor, Ir. L.M. van Leeuwen-de Leeuw and Dr. M. Schlund for their cordial guidance and support during the entire research period. It has been a privilege to work under their supervision. Moreover, I extend my gratitude to my advisor Dr. Y.A. Hussin for his continuous support and guidance throughout the research period.

I would like to acknowledge the help of Remote Sensing and GIS Lab, Faculty ITC, in obtaining the ALOS-2 PALSAR-2 image. Moreover, I am deeply thankful to the ITC Geoscience Laboratory (especially Timothy and Camilla) and Dr. P. Nyktas for assisting with the UAV image acquisition.

I extend my earnest gratitude to Dr. E.H. Kloosterman for his guidance and care during the fieldwork period. In addition, I have been incredibly honored and privileged to accompany a group of amazing people: Srilakshmi, Luis, Mishech, Efia, and Euphrasia, during the fieldwork.

Finally, I express my thanks to my beloved wife, Jinat Rezwana, for her unconditional support during the moments of stress and for providing me the courage to fight all the way through. It would have been challenging to handle the setbacks without her encouragement.

Hasan Ahmed
June 2021
Enschede

TABLE OF CONTENTS

LIST OF FIGURES

LIST OF TABLES

ACRONYMS

AAT	Automatic Angula Triangulation
AGB	Above Ground Biomass
ALOS-2	Advanced Land Observation Satellite-2
BBA	Bundle Block Adjustment
BGB	Below Ground Biomass
CD	Crown Diameter
CHM	Canopy Height Model
CO2	Carbon Dioxide
CPA	Crown Projection Area
CPs	Check Points
DBH	Diameter at the Breast height
DGNSS	Differential Global Navigation Satellite System
DSM	Digital Surface Model
DTM	Digital Terrain Model
EU	European Union
GCPs	Ground Control Polints
HH	Horizontal Send, Horizontal Receive
HV	Horizontal Send, Vertical Receive
IPCC	International Panel on Climate Change
MRV	Measurement, Reporting, and Verification
NFMS	National Forest Monitoring System
NMO	National Monuments Organisation
NMO	National Monuments Organisation
NRCS	Nornalized Radar Cross Section
PALSAR-2	Phased Array Syntectic Aperture Radar-2
RADAR	Radio Detection and Ranging
REDD	Reducing Emissions from Deforestation and Forest Degradation
RGB	Red, Green, and Blue
RMSE	Root Mean Square Error
RS	Remote Sensing
SAR	Synthetic Aperture RADAR
SfM	Structure from Motion
SLC	Single Look Complex
SNAP	Sentinel Application Platform
SRTM	Shuttle Radar Topography Mission
UAV	Unmanned Aerial Vehicle
UAVs	Unmanned Aerial Vehicles
UN	United Nations
UNFCCC	United Nations Framework Convention on Climate Change

1 INTRODUCTION

Climate change is one of the most frequently discussed and argued global challenges (European Environment Agency, 2019; Perkins et al., 2018; Urry, 2015). Deforestation is one of the significant anthropogenic reasons for climate change (Gibbs et al., 2007; IPCC, 2014). Forest is considered as a sink and source of carbon dioxide (IPCC, 2014). When forest land is degraded or altered, CO_2 is released into the atmosphere (Gibbs et al., 2007). The state of forests has been altered in many places worldwide for resources to convert into other land-use, e.g., agriculture (IPCC, 2014). Consequently, carbon dioxide (CO2) emission from the forest has been happening continuously over a long period. According to Smith et al. (2015), the forest accounts for about one-third of global carbon dioxide emission caused by human interaction, such as deforestation, degradation, and land-use change, from 1750 to 2011.

The Forest sector plays a significant role in the mitigation strategies to reduce carbon dioxide emissions(Brown, 1997; Rizvi et al., 2015). Forests are the world's largest terrestrial carbon pool (Gibbs et al., 2007). The significant carbon pools in the forest are the above-ground biomass (AGB), below-ground biomass (BGB), understory, litter, and deadwood (FAO, 2020; Gibbs et al., 2007). Afforestation or reforestation leads to the sequestration of carbon, and when the forest grows young to the old state, it works as a carbon sink (Smith et al., 2015) because CO2 is stored through the photosynthesis process. Four main mitigation strategies have been formed for world forests; these strategies are: reducing emission from deforestation, reducing emission from forest degradation, enhance carbon sink, and product substitution (Rizvi et al., 2015).

A global initiative was taken by the United Nations Framework Convention on Climate Change (UNFCCC) with its member nations to reduce carbon emissions from forests and to enhance the global carbon sink (UNEP, 2018a). The initiative is known as "Reducing Emissions from Deforestation and Forest Degradation" (REDD+). The REDD+ initiative encourages the developing countries to manage their forest sustainably in a conservative manner, reduce deforestation and degradation, and enhance carbon sink (Gibbs et al., 2007; UNEP, 2018b). REDD+ developed the concept of carbon trading and the international carbon market, in which a country with reduced emission as compared to their baseline carbon emission can sell their carbon credits to other countries who failed to reduce emission from its baseline (Gibbs et al., 2007; UNEP, 2018a).

As a prerequisite of participation in this REDD+ initiative for reduced emission and carbon trading, partner countries should develop a National Forest Monitoring System, in short, NFMS (UNEP, 2018a). NFMS has two functions: 1) forest monitoring and 2) measurement, reporting, and verification (MRV) of forest resources (UNEP, 2018a). MRV is an essential and specifically relevant mechanism to REDD+, emphasizing transparency in carbon trading. The MRV mechanism of REDD+ measures the change in forest area, quality of the forest, and forest carbon stock using various field measurements and remote sensing techniques (UNEP, 2018a). In the case of carbon assessment, the most measured forest carbon is from AGB because it is a good indicator for the overall biomass of the tree (Lucas et al., 2015), and approximately 50% of forest AGB is above-ground carbon stock (Næsset et al., 2020).

In April 2016, the Dutch ministry of environment signed the UN Climate Agreement to limit temperature rise below 2^{o} C and make efforts for not more than 1.5^{o} C global warming (Government of the Netherlands, 2021). As a part of this agreement, a yearly report, The Climate and Energy Report, is published, which requires an updated reference scenario every year (Klimaatakkoord, 2019). Moreover, the Dutch government must make a carbon and biomass inventory for every year's carbon emission forecasting (Klimaatakkoord, 2019). The carbon accounting approach in the Netherlands is based on wood stand stock calculated from the total yearly increase of wood volume/biomass and harvested wood that may not be accurate. It is expensive to conduct a full-scale survey in-field since it requires labor and time (Workie, 2011).

Moreover, in December 2019, the European Commission came up with a new set of policy initiatives for the European Union (EU) nations named 'A European Green Deal' (European Commission, 2020). The main goal of this Green Deal is to make the EU carbon neutral by 2050. As a consequence of the initiative, in January 2020, the European Commission came up with an action plan named 'New EU Forest Strategy' (European Commission, 2020). The action plan aims to increase the potential of forests to absorb CO_2, protect biodiversity and improve the bio-economy of the EU through effective afforestation, forest restoration and preservation. According to this Green Deal, EU nations increased their target to reduce carbon emission from 40% to 55% by 2030. It will be essential to measure and monitor forest carbon stock and carbon sequestration for the implementation of such an action plan. Remote sensing techniques may be used for cost-effective and accurate assessment of carbon stock, carbon emission, and carbon sequestration.

There are a couple of ways to measure the AGB of a forest. The estimation of AGB can be done either using a destructive or a non-destructive method. Destructive methods involve cutting down of the trees to oven-dry them, which is quite the opposite of the motive of REDD+, Dutch Carbon Accounting, or the EU Green Deal. Besides, the destructive method of AGB estimation has many limitations regarding time, labor, expenses and sampling biases (Stovall et al., 2017). The field measurement-based non-destructive method using the allometric equation is typically used for AGB estimation on a national level (Næsset et al., 2020; Stovall et al., 2017). The field-based allometric equation method requires biophysical data of trees such as height, diameter at breast height (DBH), wood density (Djomo & Chimi, 2017; Næsset et al., 2020; Stovall et al., 2017). Remote sensing methods to estimate AGB are also non-destructive. UNFCCC recommends a combination of field measurement and remote sensing for forest carbon monitoring and MRV at the national and sub-national level (FFPRI, 2012; Lucas et al., 2015; UNEP, 2018a).

For the monitoring of forest biomass and MRV, accurate, inexpensive, operational, and technically less complicated remote sensing methods are recommended (UNEP, 2018b). However, finding a universal method of remote sensing to estimate AGB is complicated since forests exist in different biomes and with different types of trees (Lucas et al., 2015). A couple of field based and remote sensing based techniques have been used to estimate forest AGB (Lu, 2006). The use of passive (e.g., optical) and active (e.g., RADAR, LiDAR) remote sensing has been observed in many AGB estimation studies (Cutler et al., 2012; Du et al., 2012; Hirata et al., 2014; Kaasalainen et al., 2015; Rahman et al., 2017). In the case of optical remote sensing, it was observed that medium and low-resolution optical imagery have higher uncertainty in estimating forest AGB (Boisvenue et al., 2016; Lu, 2006). High-resolution satellite imagery can estimate AGB with less uncertainty (Hirata et al., 2014). As a consequence, in the last 5-7 years, the use of the unmanned aerial vehicle (UAV) has appeared in AGB estimation literature (Berhe, 2018; Ota et al., 2015).

UAV is considered inexpensive to collect data multiple times and obtain accurate Biomass/Carbon information (Lin et al., 2018) but challenging to use in a large area. The processing of UAV images to generate orthophoto mosaic is also complicated thus requires expert knowledge of photogrammetry. The larger the area, the higher the processing time; therefore, a powerful and expensive computer is required for faster processing. Moreover, flying UAVs is restricted in many places most relevant to military interest, which consequently resulted in a limitation in image acquisition. Even though the UAV is not affected by the cloud, the flight might be difficult in places with windy weather or rainy days. Moreover, to estimate AGB/carbon stock from UAV, a couple of sources of the error must be considered, such as the error in estimating DBH from crown projection area (CPA), error in canopy height model (CHM) derived from the point cloud, and the error relevant to the allometric equation used to calculate AGB.

Furthermore, the technique using UAV detects biomass of a single tree which is further generalized to the area typically tons per ha. RGB images taken by UAV cannot detect trees underneath the top canopy layer, which makes the AGB estimation inaccurate for forest stand with large predominant or suppressed trees. *Figure 1* depicts trees that cannot be assessed using UAV RGB imagery. Despite having those limitations, UAV images can estimate AGB more accurately than any other optical remote sensing technique (Lin et al., 2018; Ota et al., 2015). A study conducted by Poley & McDermid (2020) reviewed 46 peer-reviewed studies relevant to the estimation of AGB using UAV data. The study found that the standard approach of estimating AGB using UAV data is by delineating crown areas or individual trees. They also found that UAVs can be of moderate to excellent accuracy (50% – 99%) to estimate AGB. The approach of AGB estimation from UAV is mainly based on canopy structure such as crown diameter, crown projection area (Komárek, 2020; Poley & McDermid, 2020).

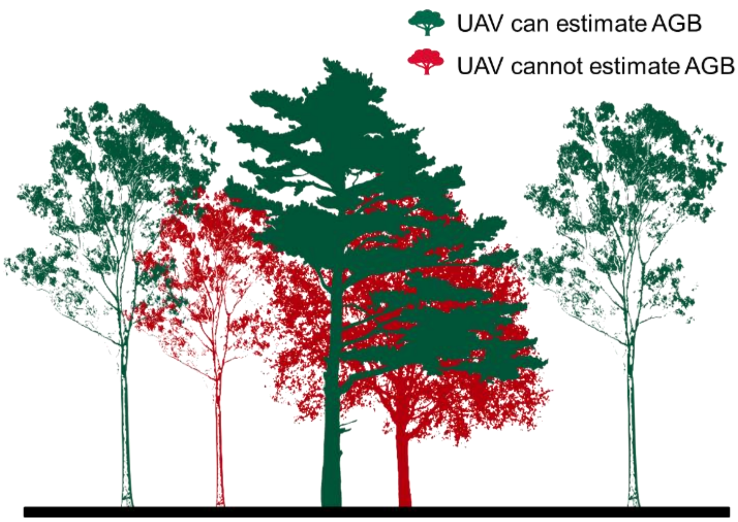

Figure 1: Limitation of UAV on estimating AGB of trees in an interlocked forest area.

On the other hand, Synthetic Aperture RADAR (SAR) data is available from various sensors, e.g., Sentinel-1, ALOS PALSAR, Radarsat, COSMO-Skymed, TerraSAR-X, ICEYE and Gofen-7. SAR is an active sensor that uses its own microwave radiation to map the surface of the earth. SAR is not significantly affected by the cloud, wind, or time of the day, making the SAR imagery operational during day and night in the all-weather situation (Parker, 2013). Therefore, it makes SAR a reasonable sensor for monitoring AGB in vast areas with clouds and rain, primarily tropical forests.

AGB from SAR can be estimated in various ways. Many studies have estimated the AGB of forest from the backscatter coefficients of SAR (Golshani et al., 2019; Masolele et al., 2018; Nguyen, 2010; Odipo et al., 2016). The Simple Cloud Water Model is also used to model AGB from SAR images (Huang et al., 2018). Moreover, nowadays, machine learning techniques have been used in modeling AGB from SAR imagery (Santi et al., 2020, 2021; Stelmaszczuk-Górska et al., 2018). However, estimation of AGB from backscatter is a widely used approach (Hojo et al., 2020; Imhoff, 1995; Mitchard et al., 2009; Nesha et al., 2020; Ningthoujam et al., 2017). AGB estimated from SAR has been found to be accurate (Liao et al., 2020; Lucas et al., 2015).

The estimation of biomass or carbon from SAR backscatter is straightforward; through a regression model with average backscatter of a set of pixels corresponding with the sample plot and the sample plot biomass (Nesha, 2019). The use of C-band, L-band, and P-band is increasing in estimating the AGB of forests (Beaudoin et al., 1994; Imhoff, 1995; Liao et al., 2020; Sandberg et al., 2011; Stelmaszczuk-Górska et al., 2018). C-band and L-band satellite SAR imagery is currently available and widely used across the world to estimate AGB (Nesha, 2019; Nguyen, 2010; Odipo et al., 2016). In addition, the L-band SAR microwave can penetrate through the crowns better compared to C-band due to its longer wavelength than the C-band microwave (Eineder et al., 2014). *Figure 2* presents the penetration of C-band and L-band SAR microwave in forest vegetation. Therefore, the L-band of SAR is used to estimate forest AGB since it is relevant to the volume scattering of trees and canopy (Nesha, 2019).

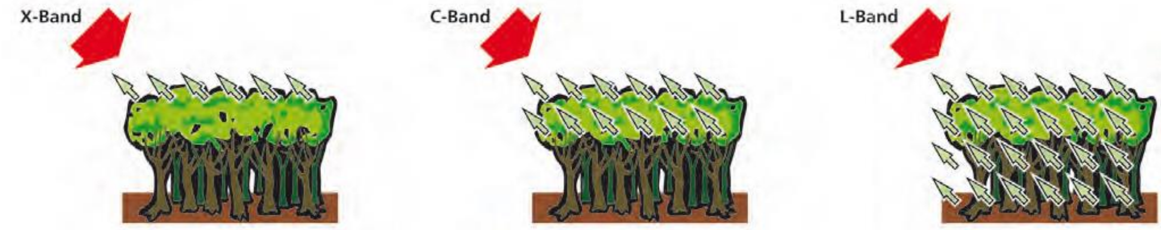

Figure 2: The penetration of X-band, C-band, and L-band SAR in forest vegetation. (as adapted from Eineder et al., 2014)

Moreover, AGB detected from SAR has comparatively fewer sources of error than UAV images. Unlike UAV RGB images, L-band SAR backscatter can penetrate the canopy, which also includes suppressed trees under the dominant or top layer. However, the resolution of SAR images is much lower compared to UAV images. Moreover, many studies found that the backscatter of SAR images saturates at a certain amount of AGB, meaning AGB beyond that amount could not be assessed by SAR backscatter (Hamdan et al., 2014; Joshi et al., 2015; Schlund et al., 2018; Yu & Saatchi, 2016). Nevertheless, the L-band SAR image requires a cost to avail. Due to the cost, it can be challenging to acquire SAR images to assess or monitor forest AGB. However, considering the area covered by an L-band SAR image, the cost is low if measured in price per area unit.

SAR images have been used to assess AGB in various biomes: tropical, boreal, temperate, mangrove (Golshani et al., 2019; Imhoff, 1995; Lucas et al., 2015; Rodríguez-Veiga et al., 2019; Stelmaszczuk-Górska et al., 2018; Watanabe et al., 2006). The use of UAV to estimate AGB has also been increasing nowadays in different biomes (d'Oliveira et al., 2020; Dash et al., 2018; Lee et al., 2020; Poley & McDermid, 2020). UAV has been used widely to estimate AGB in temperate forests (Brovkina et al., 2018; Dandois et al., 2015; Grüner et al., 2020; Mtui et al., 2017; Torres Rodriguez, 2020).

This study was conducted in a temperate forest. The temperate forest has unique characteristics and vegetation structure. It is the second-largest biome globally; temperate forests cover about 25% global forest area (Tyrrell et al., 2012). Temperate forests are distributed over some regions of North America, South America, Europe, Asia, and Oceania. Temperate forests are the world's primary source of timber and forest produce (de Gouvenain & Silander, 2017). In a temperate forest, widespread tree species types are both coniferous and broadleaf. The canopy layer in a typical temperate forest is simple, mostly consisting single canopy layer compared to the tropical or mangrove forests where those forests have multiple canopy layers. In a temperate forest with a less complicated canopy structure, tree data from UAV Orthomosaic, e.g., CPA and height, could be assessed with fewer complications than a complex tropical or mangrove forest. The relationship between AGB and ALOS-2 PALSAR-2 backscatter is also straightforward in a temperate forest.

1.1 Research Problem

According to the requirements of MRV, the remote sensing technique to estimate biomass over a forest area should be accurate, operational, reasonably less expensive, and technically less complicated (FFPRI, 2012; UNEP, 2018a, 2018b). Different sensors mounted on UAV can provide 2D and 3D information of the forest (González-Jaramillo et al., 2019; Mlambo et al., 2017b). However, UAVs also have several limitations. UAVs can be challenging to observe a large area due to their limited battery capacity (González-Jaramillo et al., 2019). Even though UAVs can be flown close to the forest, the effect of time of the day, sun angle, wind speed cannot be ignored. Moreover, UAV images require high computation power and expert training to process and obtain 3D information. Besides, the AGB estimation methods have a couple of potential errors due to different models (e.g., quality of point cloud, CPA-DBH relationship, CHM tree height accuracy). In addition, UAVs cannot assess trees intermingling with each other accurately. As mentioned before, trees that are suppressed and cannot be seen from UAV images are also missed in AGB estimation.

On the other hand, PALSAR-2 is an L-band SAR that can penetrate through the forest's canopy, containing backscatter information of suppressed trees that UAV cannot see. It is also operational in all weather conditions, independent of time of the day and sun angle. Moreover, the AGB estimation methodology from SAR backscatter coefficients is also much less complicated than UAVs. And it can estimate AGB with reasonable accuracy. However, the resolution of the image is much lower compared to UAVs. Besides, SAR backscatter saturates at a certain amount of AGB, which makes it underestimating AGB in some forests. Many studies to estimate AGB from SAR backscatter contains information on the saturation point (Brovkina et al., 2018; Grüner et al., 2020; Manakos & Lavender, 2014; Nuthammachot et al., 2020; Schlund et al., 2018; Zhu et al., 2020).

Both sensors, UAV RGB and L-band SAR, have their advantages and disadvantages. UAV has the limitation for overall AGB estimation due to the exclusion of suppressed trees, while SAR has the disadvantage of its resolution. In this regard, we have studied the AGB estimation of a temperate forest on plot level to assess the AGB estimation gap from UAV and L-band SAR as compared to biometric data.

The finding of this study may prove whether L-band SAR can make up for the uncertainty in AGB information from UAV-based assessment. Coniferous and broadleaf trees have different canopy and crown structures. Since the crown area is required to assess AGB from UAV images using the relationship between CPA and DBH, the CPA-DBH relationship from coniferous and broadleaf trees is different (Shimano, 1997). Moreover, volume backscatter from L-band SAR imagery is different for coniferous and broadleaf canopy structures, and thus information on cover types could help estimate AGB accurately (Joshi et al., 2015; Yu & Saatchi, 2016). Therefore, this study also investigated the AGB estimation from different forest stand types (coniferous, broadleaf, and mixed).

1.2 Research Objectives and Research Questions

This study aims to compare the plot-based forest biomass estimated from UAV and ALOS-2 PALSAR-2 in a temperate forest and assess their accuracy. This study also intends to assess AGB estimation of UAV and PALSAR-2 based on coniferous, broadleaves and mixed forest types.

The specific objectives of the study with relevant research questions are:

Objective 1: To estimate forest AGB using UAV RGB images.

RQ 1: What is the relationship between crown projection area from UAV and field measured DBH?

RQ 2: What is the modeled AGB from UAV RGB images?

Objective 2: To estimate forest AGB using ALOS-2 PALSAR-2 co-polarized (HH) and cross-polarized (HV) images.

RQ 3: What is the relationship between ALOS-2 PALSAR-2 backscatter and field measured AGB?

RQ 4: What is the saturation point of AGB estimation in relation to the ALOS-2 PALSAR-2 backscatter coefficient?

RQ 5: What is the modeled AGB from ALOS-2 PALSAR-2 image?

Objective 3: To assess the accuracy of AGB estimation from UAV and ALOS-2 PALSAR-2 images.

RQ 6: What is the accuracy of AGB estimation from UAV?

RQ 7: What is the accuracy of AGB estimation from ALOS-2 PALSAR-2?

Objective 4: To compare the accuracies of ALOS-2 PALSAR-2 and UAV RGB images for AGB estimation.

RQ 8: Is there a significant difference between estimated AGBs from backscatter images of ALOS-2 PALSAR-2 and UAV RGB images?

RQ 9: What is the difference in the accuracy of estimated AGB from UAV and ALOS-2 PALSAR-2 on coniferous, broadleaf, and mixed forest stand?

2 MATERIALS AND METHODS

This chapter includes sections on the description of the study area, study design, sampling design, study materials, data collection, data processing and data analysis.

2.1 Study Area

For this study, a forest area named Haagse Bos, located near Losser and about 7 km away from the city Enschede of Overijssel province, has been chosen. Haagse Bos is a small forest with an area of about 334 hectares (Workie, 2011). The forest area lies between 52.283° - 52.246°N and 6.938° - 6.975°E. A part of Haagse Bos is managed by The Dutch National Monuments Organisation (NMO) and the rest by a private company named Takkenkamp (Natuurmonumenten, 2021). The forest is a combination of semi-natural and production forests (Natuurmonumenten, 2021). The forest has both coniferous and broadleaf trees. It also has large trees under the canopy top layer in some places, making it suitable to explore the uncertainty of AGB estimation from UAV and PALSAR-2 images for more complex forest stands. *Figure 3* presents the study area with UAV flight blocks and fieldwork sample plot locations.

Common coniferous tree species of Haagse Bos are Scots Pine (*Pinus sylvestris*), Douglas Fir (*Pseudotsuga menziesii*), European larch (*Larix decidua*), and Norway Spruce (*Picea abies*). Furthermore, common broadleaf species are Oak (*Quercus robur*), European White Birch (*Betula pendula*), and European Beech (*Fagus sylvatica*). Broadleaf trees are dominant in the nature monument forest area, where coniferous trees are common in the production forest area.

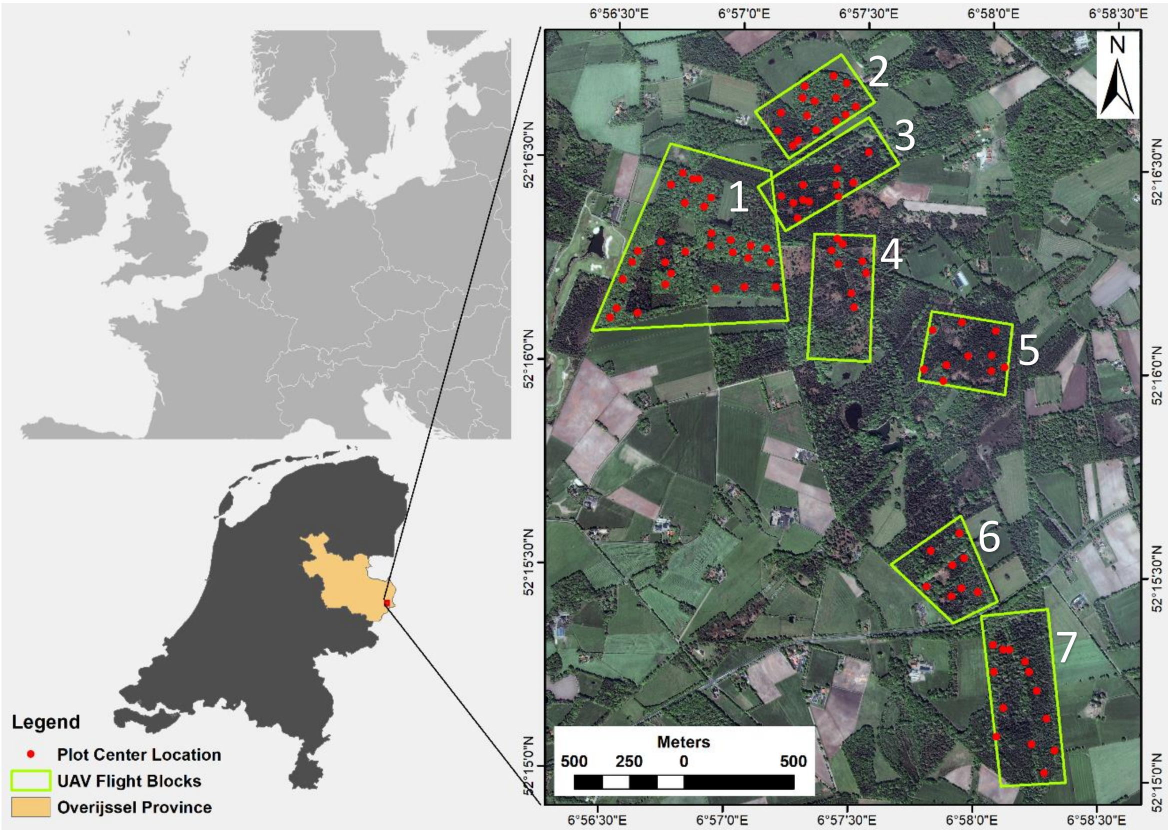

Figure 3: Study area with UAV flight blocks and sample plot locations. The green polygons indicate the flight blocks and the red points indicate the field data sample plot centers. Flight block number is indicated with the white number labels. (Source: Base map from ESRI, Netherlands Boundary from PDOK, 50 cm Superview image from Netherlands Space office taken on 08 May 2020.)

2.2 Study Design

This study was designed to estimate AGB from backscatter of ALOS-2 PALSAR-2 image and UAV RGB images, and then compare the estimated AGB from both sensor types in Haagse Bos, Enschede, the Netherlands. The study has been conducted in several steps. The main steps of the research are briefly described below in *Table 3*. Moreover, the flowchart in *Figure 4* also visualizes the methodological steps of the study involving data collection and data processing.

Table 1: List of steps and involved activities for the research.

Steps	Activities
Reconnaissance	1. Reconnaissance field visits, creating field interpretation and Google Images interpretation based maps with coniferous and broadleaf forest classes.
UAV Flight Planning	1. Selecting forest patches for UAV flights and creating flight plans to collect UAV RGB images.
Remote Sensing Data Collection	1. Conducting UAV flights and collecting 2D RGB images. This step also included fieldwork relevant to collect GCPs for UAV images.
	2. Collecting or purchasing ALOS-2 PALSAR-2 images.
Field Data Collection	1. Tree biometric data such as DBH, Tree Height, and Canopy Density from field sample plots have been collected.
Processing UAV RGB Images	1. Photogrammetric processing in creating a 3D dense point cloud from UAV RGB Images.
	2. DTM, DSM, and Orthomosaic have been created from the point cloud.
	3. CHM has been created from the DTM and DSM.
Estimating AGB from UAV RGB images	1. Manual digitization of crown projection area (CPA) of trees from UAV RGB Orthomosaic.
	2. CPA-DBH relationship has been developed using digitized CPA and field-measured DBH, and the DBH of all trees in UAV Orthomosaic has been modeled. This step answered research question 1.
	3. The total heights of trees have been identified from the CHM using delineated CPAs.
	4. AGBs of all trees have been estimated and mapped using allometric equations where tree height and DBH from UAV RGB Orthomosaic analysis have been used. This step answered research question 2.
Processing of ALOS-2 PALSAR-2 image	1. Radiometric calibration of the HH and HV polarisation ALOS-2 PALSAR-2 images has been done to retrieve HH and HV polarization backscatter.
	2. HH and HV polarization backscatter images have been georeferenced after applying Range-Doppler Terrain Correction using SRTM 30m DEM.

	3. Extracting HH and HV backscatter coefficients from the image by overlaying field plots on the images.
Estimating AGB from HV backscatter ALOS-2 PALSAR-2 image.	1. Regression models between HH and HV backscatter coefficients and field-plot AGBs have been established and validated. This step answered research question 3. 2. The saturation point of AGB estimation has been determined to answer research question 4. 3. AGB of the coniferous, broadleaf, and mixed forest stand has been modeled by using the regression equation and the saturation point. This step answered research question 5.
Accuracy Assessment of estimated AGB	1. Accuracy assessment of AGB estimation from UAV RGB images as well as HH and HV backscatter ALOS-2 PALSAR-2 image. This step answered research questions 6 and 7.
Comparing AGB estimated from UAV RGB and HV polarisation ALOS-2 PALSAR-2 image.	1. Estimated AGB from UAV RGB images and HV polarisation ALOS-2 PALSAR-2 image have been compared to answer research question 8. 2. AGB estimation accuracy from UAV RGB and HV polarisation ALOS-2 PALSAR-2 images have been compared to answer research question 9.

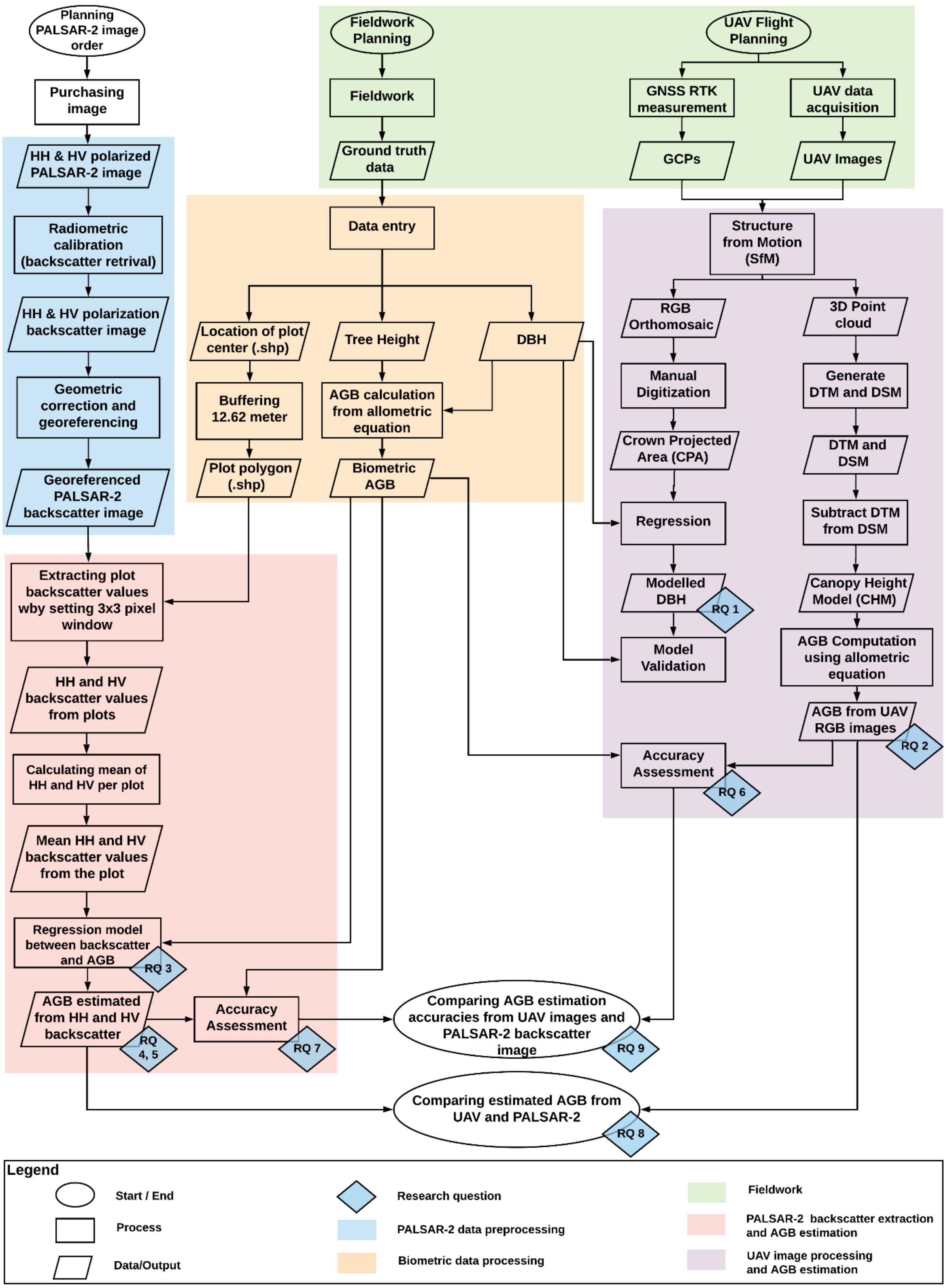

Figure 4: Flowchart of the research methods.

2.3 Sampling Design

Field data has been collected using sample plots. The sampling design should be in such a way that it is representative of coniferous and broadleaf tree species or stand in the study area. The selection of potential sample plot locations in the field is based on a stratified sampling approach. The study area was stratified into broadleaves, coniferous, and mixed stand based on visual interpretation from Google Earth. Then plots were generated randomly for each forest type. If a plot previously stratified as broadleaf had conifers in the plot or vice versa, the plot type was considered mixed during fieldwork depending on the number of broadleaf and coniferous trees in the plot. A total of 94 sample plots have been collected, of which 31 are coniferous, another 31 are broadleaf, and the remaining 32 are coniferous-broadleaf mixed forest stand.

The plot shape and size depend on the purpose of the study. In the case of AGB estimation, a plot size of 500 m^2 was preferred. It does not significantly improve the AGB estimation with a plot size of over 500 m^2 (Gobakken & Næsset, 2008; Ruiz et al., 2014). Therefore, the area of each sample plot was approximately 500 m^2. The plot shape was circular, following standard forest inventory field manuals (Bonham, 2013). A circular plot of a 500 m^2 area has a 12.62 m radius. *Figure 5* below depicts a schematic representation of a circular plot established in the field. In fieldwork, circular plots with a 12.62 m radius were established by using meter tape.

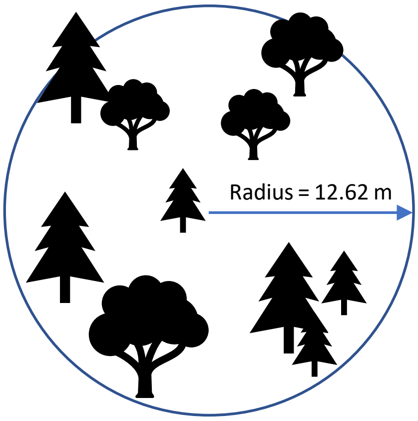

Figure 5: Schematic representation of a circular plot of 500 m2 with a 12.62 m radius.

2.4 Study Materials

For this study, two-stage fieldwork has been conducted, fieldwork for UAV flights and image collection and fieldwork for biometric data collection. Flight planning and flying zone selection were required to collect UAV images from the field. Seven flying blocks have been selected to represent the variety in the whole forest. Ground Control Points (GCPs) were recorded using a Differential Global Navigation Satellite System (DGNSS). *Table 1* provides a list of all equipment with their purposes in UAV image collection fieldwork. Orthomosaic for each flying block has been created and used to identify plot centers and trees during field data collection.

Table 2: List of equipment used for UAV image collection fieldwork.

Equipment	Purpose
UAS Phantom 4 DJI	UAS for flying and capturing 2D images.
DJI RGB Camera	Collect 2D image snapshots.
Android or iOS Device	Create flight-plan and conduct flights.
GCP Markers/Board	Place GCP marks in the fields.
DGNSS Device	Record geolocation of GCPs.

The fieldwork for biometric data collection was conducted from 03 September to 10 October. Several types of equipment were used to collect various field data. The equipments and their purposes are described in *Table 2*.

Table 3: List of field equipment used to collect tree/plot biometric data.

Equipment	Purpose
Tree tag	Tag the tree with a number
Measuring tape (30 m)	Delineate the boundary of Sample Plots
Diameter Tape (5m or 3m)	Measure the DBH of trees.
Range Finder	Measure the tree height and distance of trees from the plot center.
Sunnto Compass	Measure the North bearing of trees from the center of the plot.
Sunnto Clinometer	Measure tree height.
Datasheets and Pencil	Record field-measured data.
Tablet/Mobile	Navigation and plot center identification.

2.5 Data

As mentioned earlier, the fieldwork for data collection took place in two stages: UAV image collection and tree biometric data collection. Moreover, ALOS-2 PALSAR-2 images have been acquired for this study. Acquisition of field data, UAV image, and ALOS-2 PALSAR-2 images have been described in the following.

2.5.1 UAV Data Collection

UAV RGB images were collected in September 2020. Flights were conducted over seven blocks on different days. However, the flights were conducted by following similar weather conditions to avoid clouds and at the same time each day to have a similar sun angle. Flight plans for each block were done. *Figure 6* below represents a flight plan for one of the blocks covered in the study. *Table 4* shows the overview of flight planning parameters and camera characteristics.

Figure 6: UAV double grid Flight plan with camera position and GCP marker locations.

Table 4: Flight plan and aerial photo parameters for the UAV image collection.

Parameters	Conditions / Characteristics
Sensor	DJI FC330_3.6_4000x3000 (RGB)
Flight Mission	Double Grid (north-south, east-west)
Flying speed	slow
Overlap	90% front overlap, 80% side overlap
Camera angle	Nadir-view (90^{o})
Photo format	JPEG
Image Coordinate System	WGS 84 (EGM 96 Geoid)
CGPs	8-15 per block
GCP Coordinate System	Amersfoort / RD new (EGM 96 Geoid)

2.5.2 Field Data Collection

Fieldwork was conducted in September and October 2020. The plot center was identified and located using the Orthomosaic created from collected UAV images. 'Avenza Map' mobile application was used to determine the plot center on Orthomosaic. The application used mobile GNSS and the internet to find locations. Moreover, positions were verified using distance and north bearing from identifiable permanent objects such as trees, buildings, poles, and benches. Then the boundary of the plots was delineated using a measuring tape. Biometric data for all trees with 10 cm or above DBH was collected. Trees with less than 10 cm DBH were not measured because they are often not considered in the assessment of volume or biomass for global or commercial inventory measurements (Brown, 2002). *Table 5* below contains the list of data collected from fieldwork. A sample of the field data collection sheet is provided in *Appendix A*.

Table 5: List of data collected from fieldwork and their purposes.

Data	Purpose
Plot Center Location	To identify plots and to calculate geolocation of each tree
Tree species name	To identify and use species-specific allometric equations
DBH of Trees (DBH > 10 cm)	To calculate AGB using allometric equation
Tree Height (DBH > 10 cm)	To calculate AGB using allometric equation
Bearing of the tree from plot center	To calculate tree geolocation (X and Y coordinates)
Distance of tree from plot center	To calculate tree geolocation (X and Y coordinates)

2.5.3 ALOS-2 PALSAR-2 Data Acquisition

ALOS-2 is a satellite launched by the Japan Aerospace Exploration Agency (JAXA). It carries a sensor called Phase Array L-band Synthetic Aperture Radar (PALSAR-2) on board. A dual-polarization (HH and HV) ALOS-2 PALSAR-2 image was acquired from JAXA through Geoserve B.V., a distributor of PALSAR-2 images in the Netherlands. The ITC Faculty of Geo-information Science and Earth Observation, University of Twente, acquired the image on 14 November 2020. *Table 6* below contains the specifications of the acquired ALOS-2 PALSAR-2 image.

Table 6: Detailed specification of ALOS-2 PALSAR-2 image.

Specification of ALOS-2 PALSAR-2	Description
Scene ID	ALOS-2_PALSAR-2_ALOS2324081040-200523
Scene Observation Date and Time	23 May 2020 at 23:13:14 (UTC), Local Amsterdam time 1:13 AM
Product Type	FBDR 1.1
Product format	CEOS
Observation mode	Strip map (SM3)
Observation swath wide	70 km
Process level	1.1
Calibration factor	– 83.0
Off-nadir angle	32.9
Range spacing	4.29 m
Azimuth Spacing	3.96 m
Wavelength	0.242425 m (24 cm)
Polarization	HH and HV
Range looks x Azimuth looks	1.0 x 1.0
Observation direction	Right
PASS	Ascending
Sample type	Complex

2.6 Data Processing

After collecting biophysical data from the field and remote sensing data using UAV and ALOS-2 PALSAR-2 images, the data were processed for analysis and estimating AGB. Data processing included field data processing, UAV image processing and ALOS-2 PALSAR-2 image processing steps. The description of each processing step is provided below.

2.6.1 Field Data Processing

The forest tree biometric data have been transferred to an Excel sheet after field data collection. The locations of individual trees in a plot have been calculated in a separate Excel sheet using the bearing and distance from the center coordinate of the sample plot. Then the allometric equations have been used to calculate AGB using DBH, tree height data. Plot AGB as tons/ha has been calculated from individual tree AGB in Excel sheet as well. Further details on AGB calculation are provided in the following section.

2.6.2 Plot AGB Calculation

Calculation of AGB can be done using allometric equations. There are a plethora of allometric equations available for tree species based on their age, location, ecological zone. The allometric equations used in the analysis were selected based on their accuracy, age range, geolocation, and biome type, representing the study forest as closely as possible. *Table 7* below depicts the allometric equations used for different species to calculate species-specific tree AGB. The most suitable species-specific allometric equations to represent the age and DBH range of the trees have been found to have DBH as the only variable except Beech (Fagus sylvatica). Besides, many literatures argued that DBH is sufficient to estimate AGB accurately (Brown, 1997a; Chave et al., 2005). On the other hand, the allometric equations for beech with DBH as the only variable do not represent the age class and field data DBH range. Therefore, we used the allometric equation of beech with DBH and height as the variable.

Table 7: Allometric equations used to calculate above-ground biomass of species.

Species	AGB allometric equation	R^2	Reference
Beech *Fagus sylvatica,* Netherlands	$AGB_{[kg]} = 0.0306 * DBH_{[cm]}^{2.347} * H_{[m]}^{0.59}$	0.99	(Zianis et al., 2005)
Birch Betula pendula, United Kingdom	$AGB_{[kg]} = 0.2511 * DBH_{[cm]}^{2.29}$	0.99	(Zianis et al., 2005)
Douglas-fir *Pseudotsuga menziesii,* Netherlands	$AGB_{[kg]} = 0.111 * DBH_{[cm]}^{2.397}$	0.99	(Zianis et al., 2005)
European Ash *Fraxinus excelsior*, United Kingdom	$\ln(AGB_{[kg]}) = -2.4598 + 2.4882 * \ln(DBH_{[cm]})$	0.99	(Zianis et al., 2005)
Larch *Larix decidua,* Czech Republic	Needles branches$_{[kg]} = 0.02794 * DBH_{[cm]}^{1.80041}$ Dead branches$_{[kg]} = 0.11828 * DBH_{[cm]}^{1.4912}$ Live Branches$_{[kg]} = 0.02796 * DBH_{[cm]}^{2.19824}$ Stem wood$_{[kg]} = 0.05438 * DBH_{[cm]}^{2.420242}$ Stem bark$_{[kg]} = 0.006588 * DBH_{[cm]}^{2.42044}$ $AGB_{[kg]}$ = (Needles + Dead branches + Live branches + Stem wood + Stem bark)	0.98 0.85 0.99 0.99	(Novák et al., 2011)
Norway Spruce *Pieca abies,* Germany	$AGB_{[kg]} = -43.13 + (2.25*DBH) + (0.425*DBH_{[cm]}^2)$	0.99	(Zianis et al., 2005)

Oak *Quercus robur,* United Kingdom	$\ln(AGB_{[kg]}) = -2.3223 + 2.4029 * \ln(DBH_{[cm]})$	0.99	(Bunce, 1968)
Scots Pine *Pinus sylvestris,* Czech Republic	$AGB_{[kg]} = 0.1182 * DBH_{[cm]}^{2.3281}$	0.98	(Cienciala et al., 2006)
Norway Maple *Acer platanoides,* Canada	$AGB_{[kg]} = 0.50183 * DBH_{[cm]}^{2.0444}$	0.97	(Morrison, 1991)

After calculating AGB in kilogram for each tree from allometric equations, the AGB per plot was calculated and converted into tons/ha. In order to do that, we have summed the AGB of trees in a plot in kg then divided the sum with 1000 to convert the kg into tons. That gave us the AGB in ton for each plot (500 m^2 area). Then we divided the AGB by 0.05 to retrieve AGB in tons per hectare.

2.6.3 UAV Image Processing

After collecting 2D UAV RGB images, they have been processed using a photogrammetry software Pix4Dmapper. A 3D dense point cloud was generated in Pix4Dmapper software from each flight block, and then DSM, DTM, and Orthomosaic were generated from that 3D point cloud. Pix4Dmapper used the technique Structure from Motion (SfM) to create a 3D point cloud from 2D images with front and side overlaps. Pix4Dmapper used all the overlapping images and identified key points for various objects. Then it matched the common key points from multiple photos of the same object feature (Brovkina et al., 2018; Mlambo et al., 2017b; Westoby et al., 2012). The 3D point cloud was georeferenced using GCPs. GCPs were imported and marked in images before starting the processing of point cloud generation. The generation of the 3D point cloud in Pix4Dmapper took two steps; the initial step where Pix4Dmapper computed matching key points. In the initial processing step, the software runs Automatic Aerial Triangulation (AAT) and the Bundle Block Adjustment (BBA) techniques to find matching key points. After completing initial processing and importing GCPs, the process for the densification of the 3D point cloud started. From the 3D Dense Point Cloud, DSM, DTM, and Orthomosaic were generated. The resolution and quality of DSM, DTM, and Orthomosaic depended on the quality of the 3D point cloud.

2.6.3.1 UAV Image Processing Results

Each flight block has been processed separately. *Figure 7* below depicts the overview of processing steps in Pix4D software for block 5. All the spatial data products have been produced in the 'Amersfoort / RD_New' projection system, local coordinate systems of the Netherlands.

3D Ground Control Points (GCPs) and Check Points (CPs) were marked manually on the UAV images in the software. Minimum 5 to 15 GCPs were used to process the images. The number of GCPs depends on the size of the flight area. GCPs were located in different locations inside the flight block representing all areas. CPs were used to assess the geolocation and reprojection quality obtained by GCPs. High output quality was obtained for each block with minimum geolocation RMSE and reprojection error.

Table 10 presents the overview of image processing quality from SfM. Detailed quality reports are presented in *Appendix B*. In all flight blocks, 100% of the images have been oriented correctly and used for SfM. The density of point cloud for all blocks ranged from 32.11 per m^3 to 49.72 per m^3. GCPs have been used for each flight block, and the mean RMS ranged from 0.004m to 0.0161m. Moreover, the ground sampling distances also ranged from 4.3 cm to 5.24 cm.

The quality of the point cloud depends on the image overlap and the processing options used in the software (Dash et al., 2018; Guerra-Hernández et al., 2016; Shen et al., 2019). The average density of point cloud ranged from 32.11 to 49.72 m^{-3}, which represents a good quality allowing Orthomosaic with good detail (from 4.4 x 4.4 cm to 5.24 x 5.24 cm resolution).

The resolution of DSM ranged from 4.3 cm (0.043 m) to 5.24 cm (0.0052 m). Similarly, DTM output resolution was from 22 cm (0.22m) to 25.7 cm (0.25m). The resolution of DTM affects the resolution of CHM. All the DSMs have been resampled to 25 cm (0.25 m) resolution to match the lowest DTM resolution prior to creating CHM. Therefore, the final resolution of CHM obtained from the UAV was 25 cm (0.25m).

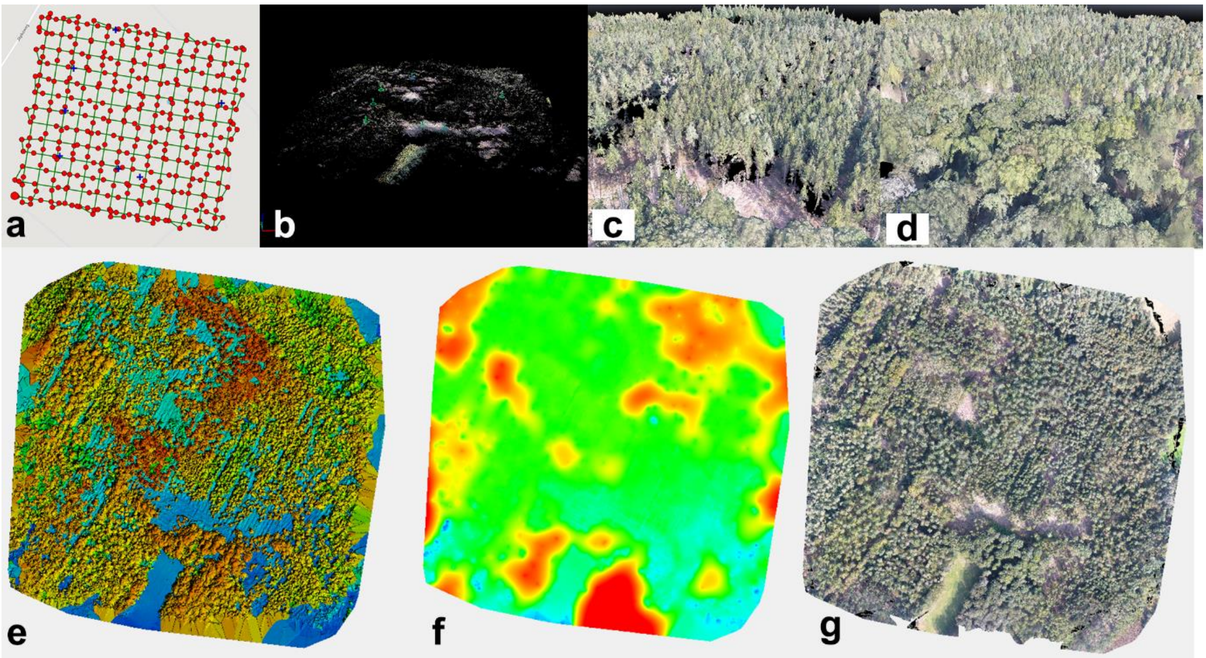

Figure 7: Overview of UAV RGB image processing in Pix4D software. (a) images from the UAV camera and their positions with GCPs, (b) matching tie points obtained from initial processing, (c) 3D point cloud after densification, (d) 3D triangulation process, (e) DSM obtained from the 3D point cloud, (f) DTM generated from the point cloud, and (g) Orthomosaic generated from the point cloud.

Table 8: Summary of UAV image processing Quality from SfM.

	Block 1	Block 2,3	Block 4	Block 5	Block 6	Block7
Average GSD (cm)	5.24	4.49	4.4	4.46	4.41	4.61
Total Area (ha)	99.73	57.54	32.24	26.44	27.44	52.05
georeferencing mean RMS (m)	0.005	0.011	0.004	0.016	0.006	0.007
Bundle Block Adjustment						
Mean reprojection error (pixels)	0.125	0.246	0.272	0.241	0.209	0.241
Point Cloud densification						
Number of 3D densified points	97675305	78684624	20621494	22868055	28796000	22759113

Average point cloud density	33.48	49.72	32.11	32.84	43.59	37.64
DSM, Orthomosaic, and DTM						
DSM and Orthomosaic resolution	5.24	4.49	4.4	4.46	4.41	4.61
DTM resolution	25.7	22.45	22	22.3	22.05	23.05

2.6.3.2 Canopy Height Model generation

The canopy height model is used to identify tree height from UAV images. It was derived from the DSM and DTM generated from the 3D point cloud of UAV images. CHM was generated by subtracting DTM from DSM in the raster calculator. Figure 8 below shows the CHM of the study area calculated from a UAV point cloud generated DSM and DTM.

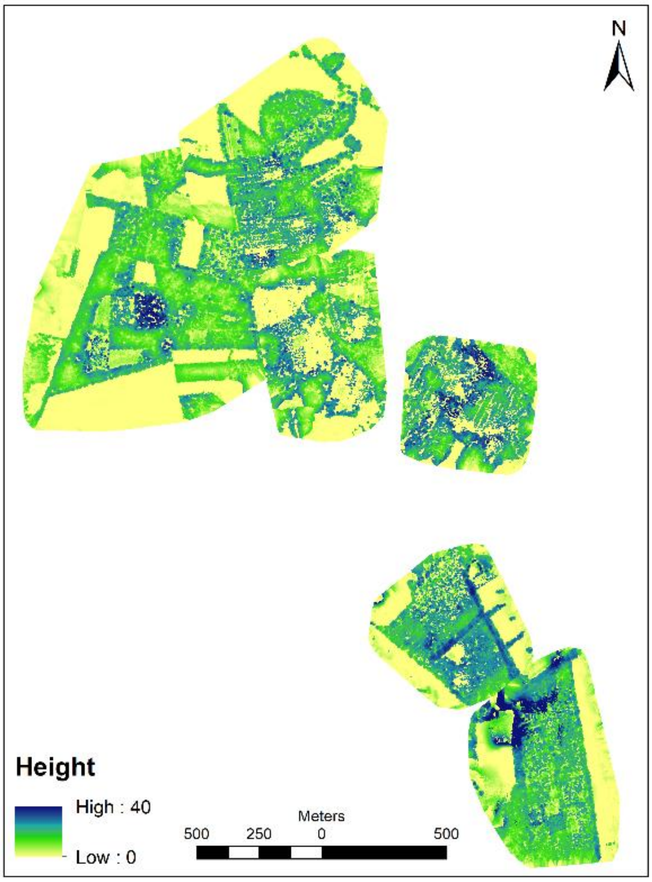

Figure 8: Canopy height model obtained from UAV DSM and DTM.

2.6.3.3 Crown Projection Area Digitization

Accurate delineation of the crown projection area is crucial for the CPA-DBH relationship model. Previous studies proved that on-screen manual digitization provides the most accurate CPA of trees (Gaden, 2020; González-Jaramillo et al., 2019; Grznárová et al., 2019; Guerra-Hernández et al., 2016; Torres Rodriguez, 2020). For this reason, this study also used on-screen manually digitized CPA of trees visible from the UAV images to develop the CPA-DBH relationship model.

The UAV Orthomosaic was loaded on ArcMap software, and the CPA of individual trees was digitized on-screen manually. Polygon shapefile was created for the manually digitized CPAs, and the area of each polygon/CPA was calculated using the calculate geometry function in ArcMap. CPA area was calculated in m^2 unit. To identify the trees and the shape of the tree, UAV images, plot photos, and tree information from field data were used.

The accuracy of the crown projection area depends on the quality and detail of the UAV Orthomosaic. Since the UAV flights were conducted on different blocks on different days, the Orthomosaic were not uniform; there were some blurs or shift on the Orthomosaic of block 4, block 5, and block 7. Therefore, we did not include plots from those locations in the manual digitization and excluded these plots from UAV-based analysis. To ensure the accuracy in CPA delineation, the digitization was conducted with caution so that crowns of multiple trees are not delineated as one crown, and the branches of one tree are perceived as multiple crowns. *Figure 9* present a plot with manually digitized CPAs of trees. Total 57 plots were digitized manually, and a total of 562 CPAs were delineated.

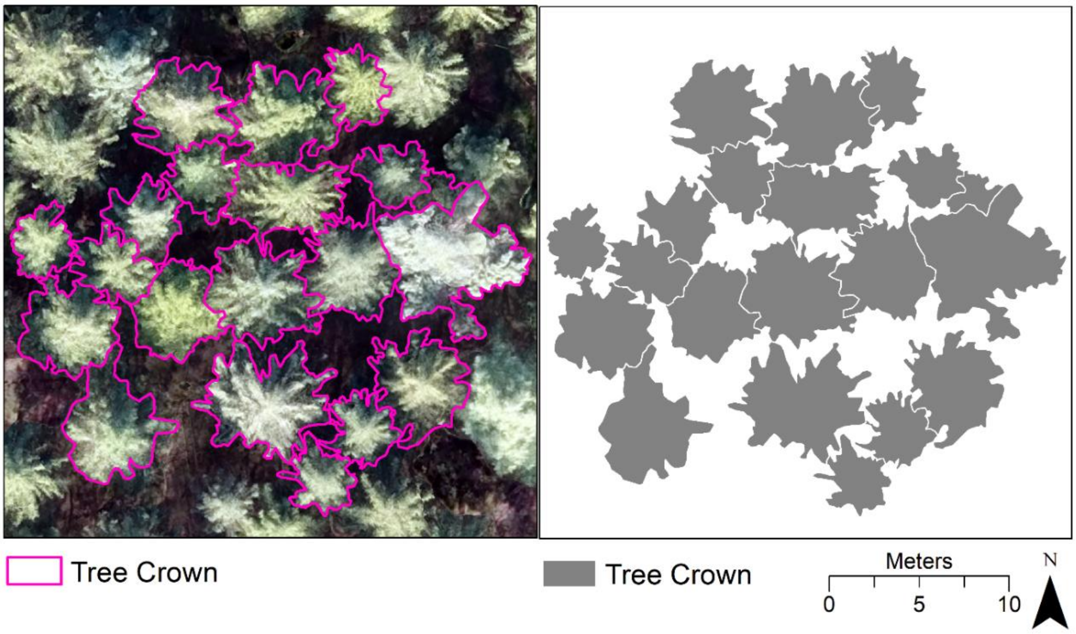

Figure 9: Examples of tree crowns manually digitized on-screen from UAV Orthomosaic.

2.6.3.4 Obtaining tree height from CHM

Height information was used in the allometric equation of Beech (Fagus sylvatica) species. Therefore, the height of trees from UAV CHM was also derived. We use manually digitized CPAs to determine the maximum value of CHM inside the polygons as tree height. The accuracy of CHM tree height also depends on the quality of the 3D point cloud, DSM, and the DTM (Dandois et al., 2015).

2.6.4 ALOS-2 PALSAR-2 Image Processing

The ALOS-2 PALSAR-2 image was obtained as CEOS level 1.1 product. Pre-processing of the image was required to obtain HH and HV polarization backscatter coefficients. First, a radiometric calibration was performed to convert the DN values into HH and HV backscatter values. Then geometric correction and georeferencing were conducted.

2.6.4.1 Radiometric calibration to retrieve backscatter

Radiometric calibration was applied to convert radar DN values into backscatter coefficients expressed in decibels (dB), also known as Normalized Radar Cross Section (NRCS). Equation 1 was used to retrieve backscatter coefficients, which was proposed by Shimada et al. (2009). The equation was applied using band math in SNAP software. Backscatter coefficients for co-polarization (HH) and cross-polarization (HV) images were obtained. The backscatter images obtained after conducting radiometric calibration are presented in Appendix C. The backscatter coefficients in the whole scene for HV polarization ranged from -8.5 dB to -43 dB, and for HH polarization, it ranged from -1.9 dB to -34.2 dB.

Equation 1: Retrieval of PALSAR-2 backscatter coefficients

$$\boldsymbol{\sigma 01.1\ product} = \mathbf{10.}\boldsymbol{log}\mathbf{10}(\boldsymbol{I2} + \boldsymbol{Q2}) + \boldsymbol{CF} - \boldsymbol{A}$$

Where,

$\boldsymbol{\sigma 01.1\ product}$ = Normalized Radar Cross Section of level 1.1 product in (dB)
I = Real part of Single Look Complex (SLC) level 1.1 product
Q = Imaginary part of SLC level 1.1 product
CF = Calibration Factor = -83.0 dB
A= Constant, 32.0

2.6.4.2 Geometric correction and georeferencing

After obtaining NRCS using Equation 1, the geometric correction of the images was done using the Range-Doppler Terrain Correction method. Then the images were georeferenced. Range-Doppler Terrain Correction was used because it is one of the standard and precise techniques for geometric correction of radar images (Jiang et al., 2016). Range-Doppler Terrain Correction requires a Digital Elevation Model to shift the pixels to actual geolocation. In this study, we have used Shuttle Radar Topography Mission (SRTM) DEM of 30 m resolution. SRTM-1sec DEM (30m) can be downloaded in SNAP automatically while applying Range Doppler Terrain Correction. PALSAR-2 image was georeferenced to Amersfoort/ RD New projection system after terrain correction. After georeferencing and removing geometric distortions, the final backscatter image resolution was 7 m. Figure 10 depicts HV and HH backscatter images after terrain correction and applying georeferencing.

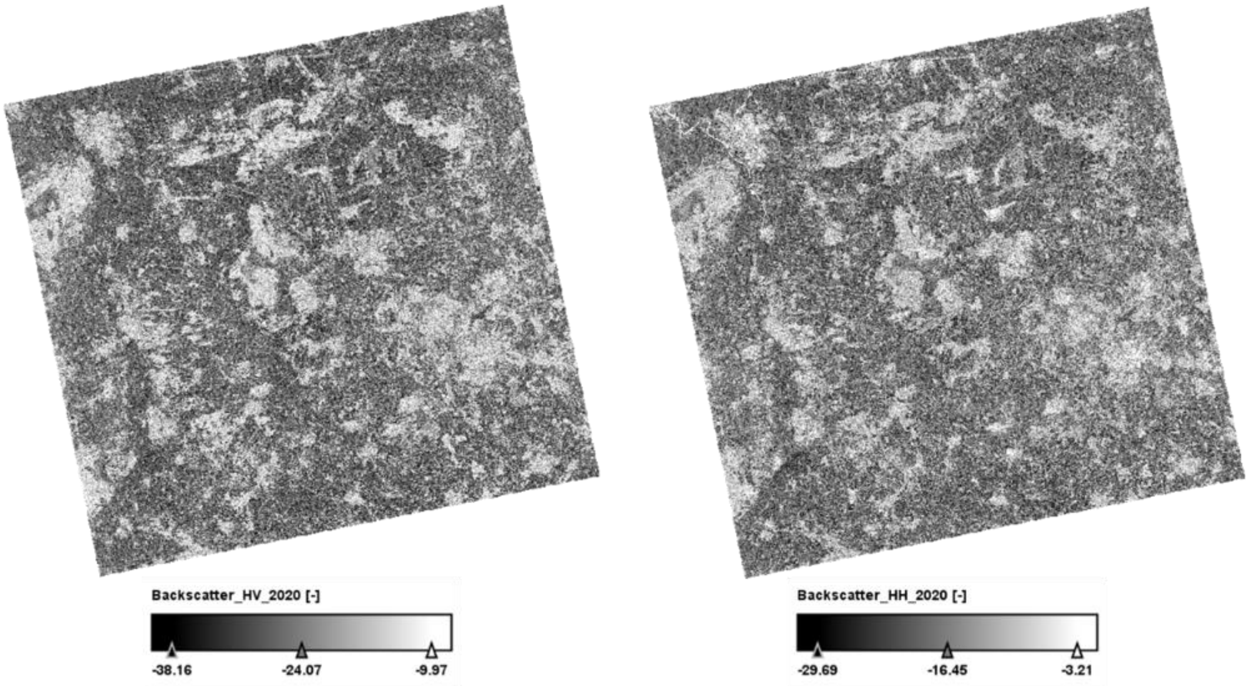

Figure 10: Geometric correction and georeferencing of PALSAR-2 backscatter images.

2.6.4.3 Noise reduction and filtering

Speckle noise is inherent in SAR images, and thus the speckle filtering has been applied after geometric correction and georeferencing. Speckle noise can affect the AGB estimation significantly from backscatter coefficients (Joshi et al., 2015; Schlund et al., 2018). In this study, a 3x3 pixels kernel Lee speckle filter was applied on HV and HH backscatter images to smooth the images and reduce speckle noise.

2.6.4.4 Backscatter coefficient extraction

The HH and HV backscatter coefficients were extracted for each plot in the study area to use in further analysis. Since the field plot is circular and has a 12.62 m radius, the diameter of the sample plot is 25.24 m. Due to the 7 m resolution of the backscatter image, fitting the sample plot with approximately 25 meters diameter was complicated. Therefore, an approach similar to Hamdan et al. (2014), Masolele et al. (2018), and Nesha et al. (2020) have been taken where a 3x3 pixel window was fitted approximately with the plots to extract the backscatter coefficients. *Figure 11* below depicts how a 3x3 pixel window was established for each plot to extract backscatter coefficients.

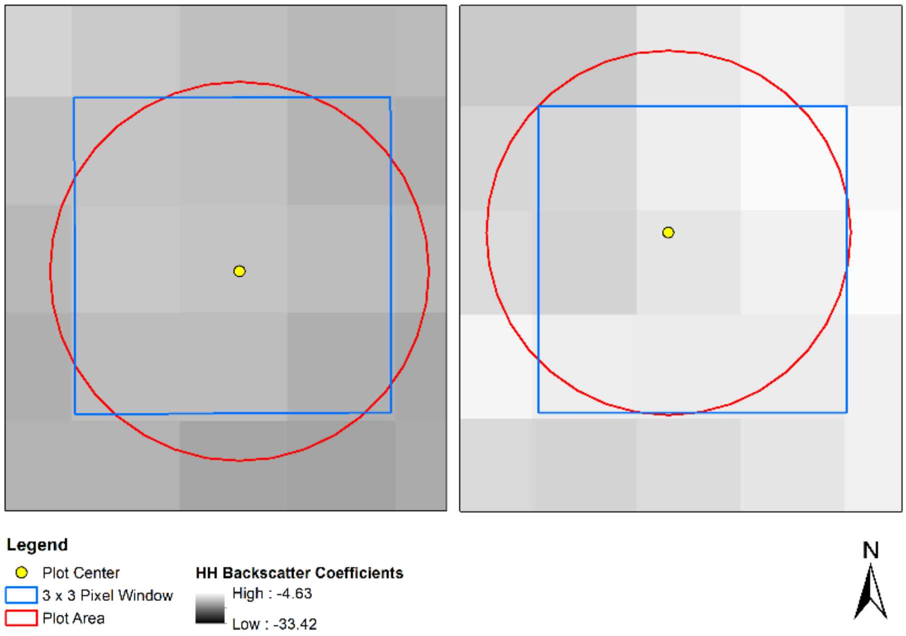

Figure 11: Fitting 3x3 pixel window to extract backscatter coefficients per plot.

2.7 Data Analysis

Data analysis included AGB calculation, development of models to predict DBH from UAV, model development to estimate AGB from UAV image and ALOS-2 PALSAR-2 backscatter coefficients, and accuracy assessment of models and AGB estimations.

2.7.1 DBH-Crown Relationship Analysis

The relationship between tree DBH and crown parameters such as the crown projection area, the crown diameter has been proven in multiple studies (Abdollahnejad et al., 2018; Brown, 2002; Fu et al., 2020; Gaden, 2020; Shashkov et al., 2019; Shimano, 1997; Torres Rodriguez, 2020; Yang et al., 2020; Yurtseven et al., 2019). The relationship between CPA and DBH has been found to be non-linear by the authors, such as Fu et al. (2020), Shimano (1997), and Yang et al. (2020). For a young open growth forest, the relationship between CPA and DBH is proportional. The growth of CPA becomes slower compared to DBH after the forest grows for a certain age due to the competition of canopy density (Chave et al., 2005; Shimano, 1997).

Regression models between Crown Projection Area (CPA) of trees obtained from the UAV Orthomosaic and field measured DBH have been created to estimate DBH of broadleaf and conifer trees. Total 121 broadleaf and 134 coniferous trees were manually digitized to obtain the most accurate CPA. For model development and model validation, the data have been split into model development and model validation sets. 91 broadleaf and 94 coniferous trees have been used to develop the CPA-DBH relationship model, 30 and 41 trees have been used accordingly to validate the models. Therefore, trees that were used for validation were independent of the model data.

To determine the relationship between CPA-DBH, different regression functions, e.g., linear, logarithmic, exponential, polynomial, and power regression functions have been applied. The best fit model was chosen based on the regression output for model development and validation. Regression parameters such as correlation coefficient (r), coefficient of determination (R^2), and Root Mean Square Error (RMSE) were used to determine the best fit model.

2.7.2 AGB Estimation from UAV Orthomosaic

After the development of the CPA-DBH relationship model, the model was used to estimate the DBH of trees all trees (562 trees) from 57 manually digitized plots. Predicted DBH for each tree was used in species-specific allometric equations provided in *Table 7*. The height of Beech was also used in the allometric equation. Therefore, the height of each tree was extracted by using the zonal statistics tool in ArcMap software, where the maximum value inside each CPA polygon was identified from the CHM raster image. Thus, applying CPA-DBH modeled DBH and CHM estimated tree height in species-specific allometric equations, individual tree AGB was calculated. Then the plot AGB was calculated by summing to AGB of all trees from the corresponding plot, and the total value was transformed into tons/ha unit.

2.7.3 Regression Analysis and AGB Estimation from ALOS-2 PALSAR-2

AGB estimation from SAR can be done using several methods (Becek, 2009; Joshi et al., 2015; Liao et al., 2020; Masolele et al., 2018; Nguyen, 2010; Schlund et al., 2018; Zhu et al., 2020). The L-band PALSAR-2 image was obtained with HH and HV polarization. Therefore, we used backscatter and biometric AGB regression analysis to model AGB from backscatter coefficients. Previous studies to model AGB from backscatter revealed that the relationship between backscatter and AGB was considered either linear or logarithmic (Hamdan et al., 2014; Joshi et al., 2015; Masolele et al., 2018; Nesha et al., 2020; Nguyen, 2010; Yu & Saatchi, 2016). In this study, the linear regression function provided in *Equation 2* has been applied to estimate AGB from backscatter coefficients.

Equation 2: Linear regression model between AGB and ALOS-2 PALSAR-2 Backscatter coefficients.

$$AGB = \beta_0\, \sigma^o + \beta_1$$

Where,

AGB = the predicted AGB
σ^o = the HH or HV backscatter coefficient in (dB)
β_0 = the model coefficient for σ°_{slc}
β_1 = the intercept of the regression model

Moreover, the logarithmic function to model AGB from backscatter coefficients is frequently used (Imhoff, 1995; Schlund et al., 2018; Yu & Saatchi, 2016). In that case, a relationship between backscatter coefficients and log(AGB) is developed, which is often denoted as the forward model (Schlund et al., 2018). Then a formula or backward model is used to calculate the AGB values from the forward model (Schlund et al., 2018). In our case, we used the formula in Equation 3 to develop a relationship between backscatter coefficients and $\log_{10}$(AGB). Then we transformed the $\log_{10}$(AGB) into AGB values by calculating the antilog.

Equation 3: Linear regression model between log_{10}(AGB) and ALOS-2 PALSAR-2 Backscatter coefficients.

$$log_{10}(AGB) = \beta_0\ \sigma^o + \beta_1$$

Where,

Log_{10}(AGB) = Logarithmic value of the predicted AGB
σ^o = the HH or HV backscatter coefficient in (dB)
β_0 = the model coefficient for σ°_{slc}
β_1 = the intercept of the regression model

The dataset was split into two sets: for model development and model validation. Fifty plots have been used in the regression model development. The rest of the plots were used for model validation. The models have been validated using field-measured AGB data. A similar regression model was developed for AGB and backscatter coefficients for plots grouped into coniferous, deciduous, and mixed forest stand.

2.7.4 Accuracy Assessment and Comparison

Accuracy assessments on estimated AGB from UAV and PALSAR-2 images have been conducted. For accuracy assessment, the same plots have been used for UAV and PALSAR-2 images. Predicted AGBs on the validation plots have been plotted against the observed AGBs from the field in a linear relationship. The accuracy has been evaluated by using statistical indicators from the relationship such as R^2, RMSE. RMSE has been calculated by using the following formula (*Equation 4*).

Equation 4: Equation for RMSE calculation.

$$RMSE = \sqrt{\frac{\sum_{i=1}^{n}\left(\hat{Y} - Y\right)^2}{n}}$$

Where,

RMSE = the Root Mean Square Error
Y = the observed AGB from field
$\hat{Y}$ = the predicted AGB from UAV or ALOS-2 PALSAR-2 using the model
n = the number of validation plots

Moreover, to assess and compare whether the AGBs estimated from the field, modeled from UAV and ALOS-2 PALSAR-2, are significantly different, a one-way ANOVA F-test among all measurements has been conducted.

2.7.5 Determination of AGB Saturation point

Previous studies found that in a backscatter-AGB regression model, backscatter coefficients saturate at a certain value of AGB. This value of AGB is recognized as the saturation point for the backscatter coefficients. Watanabe et al. (2006) determined saturation point for different polarization backscatter coefficients from L-band SAR by plotting AGB and backscatter coefficients in a logarithmic regression. Then the slope of the curve was calculated at different AGB values for corresponding backscatter coefficients. The saturation point was determined when the slope of backscatter coefficients and AGB regression converge at 0.01. The following equation (*Equation 5*) was used to calculate the slope of the curve, and the AGB value at slope = 0.01 was determined as the saturation point.

Equation 5: Determination of slope of AGB-backscatter coefficients regression to determine AGB saturation point.

$$\text{Slope} = \Delta Y / \Delta X$$

Where,

ΔY = The change in backscatter values from the minimum backscatter value.
ΔX = The change in AGB from the minimum AGB value.

3 RESULTS

The following section describes the results from the field data collection. Then, it presents the results obtained from UAV image processing and analysis: DBH – CPA relationship model development and validation, and AGB estimation from modeled DBH and tree height. Moreover, this section also includes regression analysis between AGB and PALSAR-2 backscatter coefficients followed with AGB estimation model development and validation. Finally, the comparison results between AGB estimated from UAV and ALOS-2 PALSAR-2 are presented.

3.1 Results from the Field Data Analysis

Plot and tree biometric parameters have been collected from the fieldwork. Tree species have been identified on the plot. A total of 94 plots have been collected, of which 31 plots are conifer-dominated, 31 plots are broadleaves-dominated, and 32 plots represent mixed forest stand. Details of the tree species and relevant field parameters are described in the following.

3.1.1 Description of the Tree Species

During the fieldwork, a total of 1584 trees have been recorded. Among them, 928 trees were coniferous, and 656 trees were broadleaf. From the sample plots, 470 individuals of *Pseudotsuga menziesii,* 189 individuals of *Pinus sylvestris,* 177 individuals of *Pieca abies,* and 83 individuals of *Larix decidua* trees were recorded, which are coniferous species. Broadleaf species that were found are: 279 individuals of *Fagus sylvatica*, 229 individuals of *Quercus robur,* 118 individuals of *Betula pendula,* 20 individuals of *Fraxinus excelsior,* and 20 individuals of *Acer platanoides.* Details of species and their distribution are depicted in *Figure 12* below.

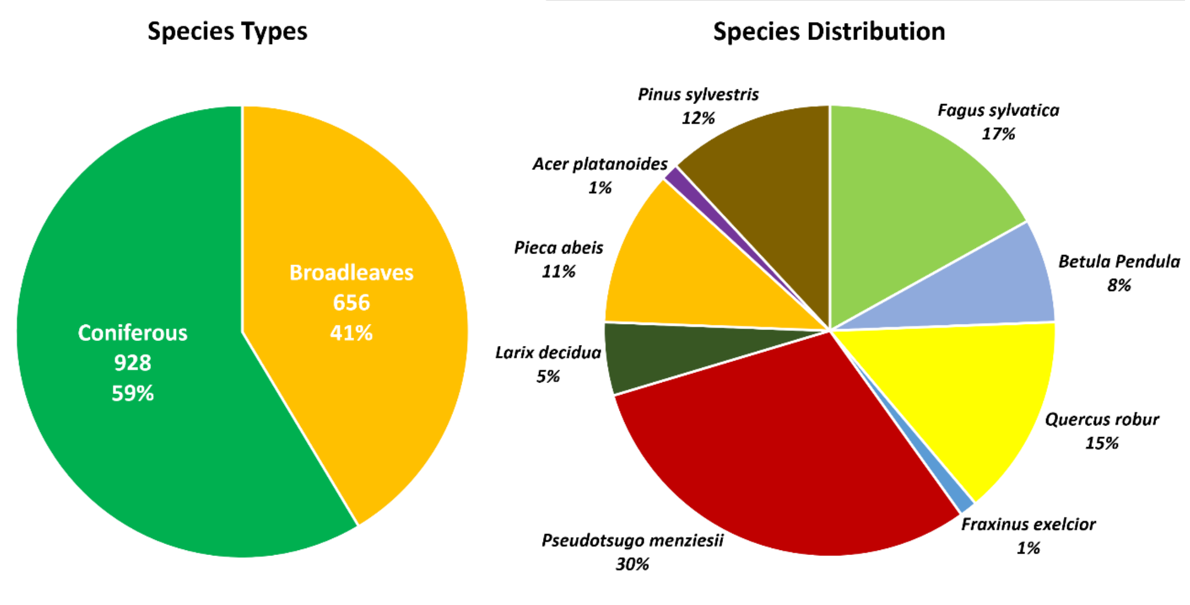

Figure 12: Details of tree species recorded from the sample plots in the fieldwork.

3.1.2 Descriptive Statistics of the Field Data Parameters

Diameter at breast height (DBH) and the total height of all trees with a minimum of 10 cm DBH have been recorded for each plot. The mean DBH of all trees recorded was 33.5; for broadleaves, the mean DBH was 36.7 and 31.2 for conifers. The largest tree recorded in the field was a broadleaf species with 101.9 cm DBH. The maximum DBH observed for conifers was 85.6 cm. *Table 9* presents the descriptive statistics of biometric DBH and total height for all trees and species represented as conifers and broadleaves.

Table 9: Summary statistics of DBH and tree height from field measured data.

	All trees		**Broadleaves**		**Conifers**	
	DBH (cm)	Height (m)	DBH (cm)	Height (m)	DBH (cm)	Height (m)
Number of trees	1584	1584	656	655	928	928
Mean	33.5	19.3	36.7	19.1	31.2	19.4
Standard Error	0.38	0.14	0.69	0.22	0.42	0.18
Standard Deviation	15.32	5.51	17.7	5.58	12.91	5.47
Minimum	10	3.4	10	3.4	10	4
Maximum	101.9	35.2	101.9	30.9	85.6	35.2
Sample Variance	234.57	30.4	313.04	31.11	166.63	29.88
Range	91.9	31.8	91.9	27.5	75.60	31.2
Kurtosis	0.51	-0.16	-0.2	-0.5	0.91	0.08
Skewness	0.74	-0.36	0.47	-0.49	0.79	-0.26
W statistics	0.958	0.985	0.962	0.971	0.96	0.989
p-value	4.79e-21	1.06e-11	3.69e-12	2.87e-10	4.49e-15	2.78e- 6
Normal Distribution	False	False	False	False	False	False

The normal Q-Q plot of biometric DBH presented in *Figure 13* shows that DBH of broadleaves and conifers are skewed to the left at both lower and higher values. The Shapiro-Wilk test (Shapiro & Wilk, 1965) also resulted in a p-value lower than 0.05; therefore, the field measured DBH for all trees and grouped into broadleaves, and coniferous was significantly different from the normal distribution. The DBH of trees resulted in a skewed distribution because trees with less than 10 cm DBH were not measured. The Shapiro-Wilk test W statistics and p-values are also presented in *Table 9*.

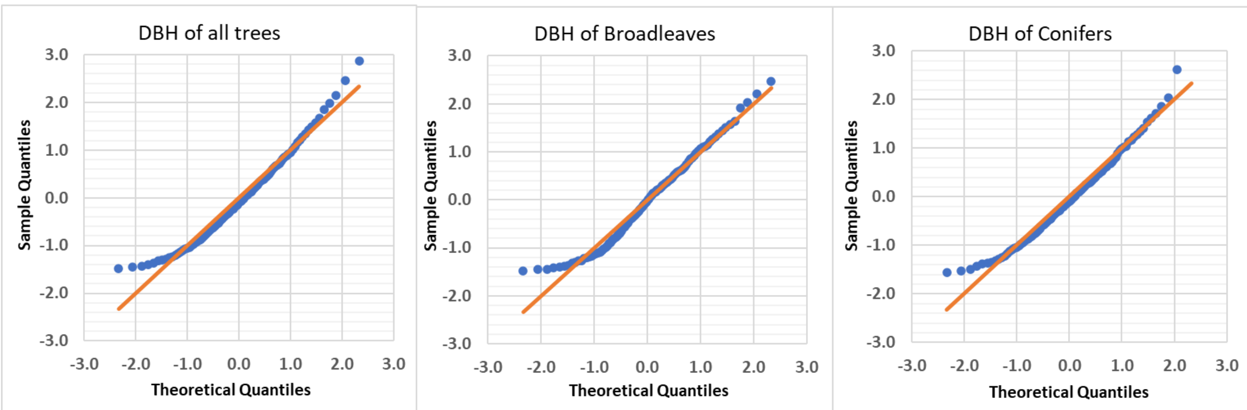

Figure 13: Normal QQ plot of DBH of all trees measured from fieldwork.

Similarly, we have also tested the normality of biometric tree height. The normal Q-Q distribution plot in *Figure 14* shows that tree heights are skewed to the right at higher values. The Shapiro-Wilk normality test also showed W statistics of 0.985, 0.971, and 0.989 respectively for all trees, broadleaves, and conifers with a p-value lower than 0.05 in all cases; p-values are presented in *Table 9*. Therefore, the biometric heights for all trees, broadleaves, and conifers were also statistically significantly different from the normal distribution.

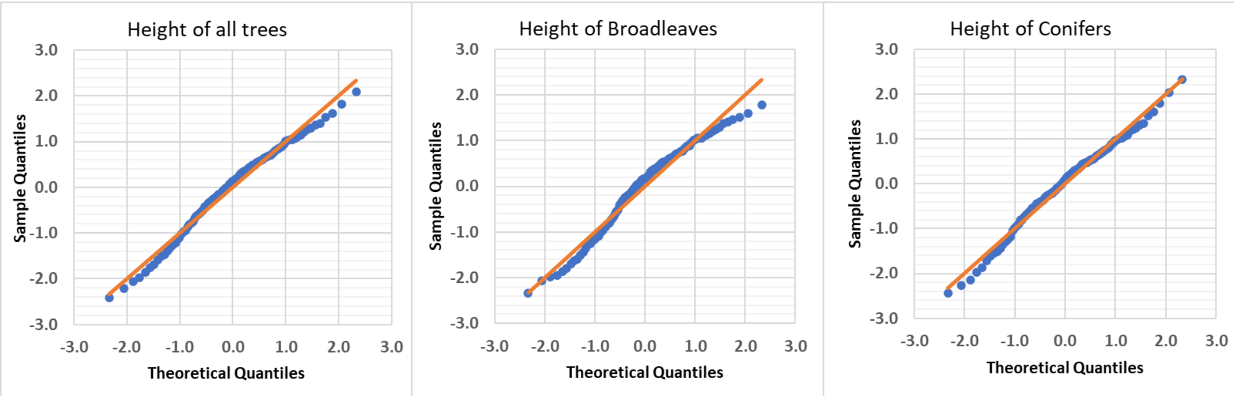

Figure 14: Normal QQ plot of the height of all trees measured from fieldwork.

3.1.2.1 Biometric AGB

AGB for individual trees from biometric data has been calculated using species-specific allometric equations. The unit of AGB for individual trees was in kilograms. Then, the biometric AGB per plot has been calculated by summing individual trees and converting the total value to tons per hectare unit. *Table 10* below depicts the descriptive statistics of biometric AGB calculated on individual tree level and plot level.

Table 10: Descriptive statistics of biometric AGB from individual trees and biometric AGB for plots.

	Tree AGB(kg/tree)			**Plot AGB (tons/ha)**			
	All Trees	Broadleaves	Conifers	All Plots	Broadleaves	Conifers	Mixed
Count	1584	656	928	94	30	31	33
Mean	747.19	1075.17	515.34	245.67	308.61	196.31	234.82
Minimum	47.69	56.12	47.69	71.96	124.48	71.96	89.08
Maximum	10610.42	10610.42	4758.42	640.71	621.29	640.71	528.03
Standard Error	23.30	47.33	18.00	12.51	23.46	19.41	17.97
Standard Deviation	927.44	1212.21	548.27	121.31	128.51	108.06	103.24
Sample Variance	860136.55	1469450.03	300599.85	14715.33	16514.56	11677.33	10658.19
Range	10562.73	10554.30	4711.73	568.75	496.81	568.75	438.95
Kurtosis	16.56	9.46	13.75	1.41	-0.08	10.0	1.13
Skewness	3.20	2.41	3.07	1.32	0.74	2.91	1.16
W statistics	0.686	0.770	0.715	0.877	0.680	0.944	0.906
p-value	2.85e-47	2.75e-29	2.75e-29	2.69e-07	6.02e-07	0.12	0.008
Normal Distribution	False	False	False	False	False	True	False

The normality of biometric AGB has also been tested. *Table 10* depicts the Shapiro-Wilk normality test result of the biometric AGB. The distribution of AGB has been visualized by using a histogram with a density curve in *Figure 15*, along with a normal Q-Q plot for all plots. AGB density curve shows that biometric AGB is left-skewed. The normal Q-Q plot also reveals that plot AGB data is skewed to the left at lower values and higher values and right-skewed at middle values. From the Shapiro-Wilk normality test, AGB distribution for all plots, broadleaves dominated plots, and conifers dominated plots have been found to be significantly different from the normal distribution. However, AGB for mixed plots resulted in W statistics of 0.942 with a p-value of 0.099, which is higher than 0.05. Therefore, the AGB of mixed plots is normally distributed.

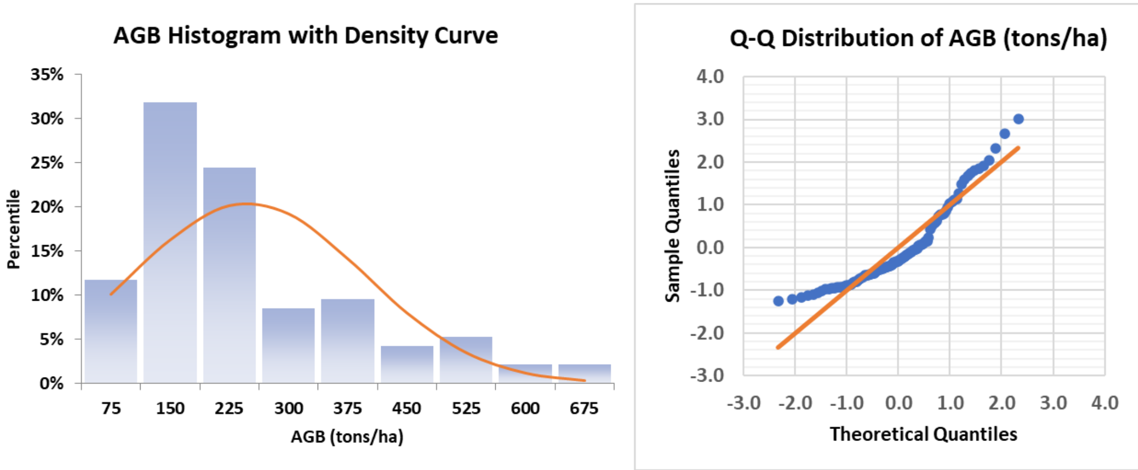

Figure 15: Histogram of plot AGB with density curve and normal Q-Q plot.

3.2 Results from UAV RGB Analysis

UAV RGB images have been processed to generate Orthomosaic, DSM, DTM. The following sections describe the results obtained from the delineation of individual tree crown projection area from Orthomosaic and acquiring tree height from CHM (in section 3.2.1). Then, the results from the CPA-DBH relationship model to estimate DBH and the validation of the model have been described in section 3.2.2. And finally, the AGB estimated from the parameters obtained from UAV processing results have been described in section 3.2.3.

3.2.1 Crown Projection Area and Tree Height from UAV

A total of 562 individual trees have digitized been manually from 54 plots. *Table 11* below depicts the statistical description of CPAs obtained by manual digitization. CPA ranged from 4.95 m^2 to 270.59 m^2. We have performed a normality test on the CPAs obtained from Orthomosaic. The Shapiro-Wilk test resulted in a W statistics of 0.805 at a p-value of 1.73e-25, which indicates that the CPA data are not normally distributed. The normal Q-Q plot of CPAs presented in *Figure 16* shows that the data are skewed to the left at the lower and upper ends and right-skewed at the middle. Moreover, the CPAs have been used to extract the height of the corresponding tree from the CHM. The description of tree height obtained from CHM is also presented in *Table 11*. Tree heights from CHM were also not normally distributed. Shapiro-Wilk test performed with 0.974 W statistics at 2.13e-8 p-value. The normal Q-Q plot in *Figure 16* shows that the CHM heights are right-skewed at the higher values and consistent with the distribution of height data measured in the field.

Table 11: Descriptive statistics of CPA from Orthomosaic and tree height from CHM.

	CPA	CHM Height
Count	562	562
Mean	47.04	19.11
Minimum	4.95	4.61
Maximum	270.59	33.32
Standard Error	1.73	0.24
Standard Deviation	41.01	5.76
Sample Variance	1681.53	33.19
Kurtosis	4.94	-0.56
Skewness	1.95	-0.33
W Statistics	0.805	0.974
p-value	1.73e-25	2.13e-8
Normal Distribution	False	False

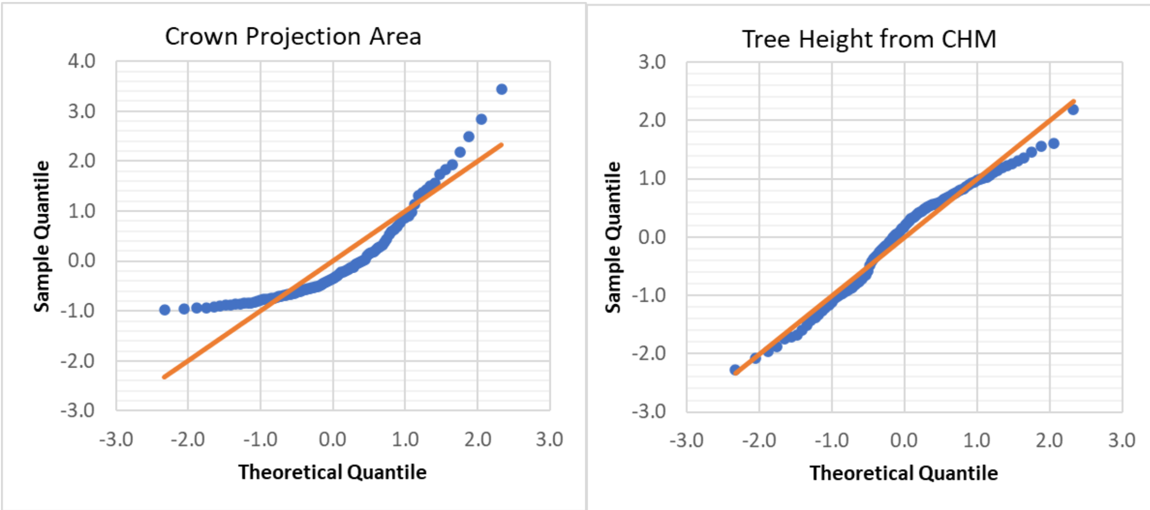

Figure 16: Normal Q-Q plot of CPA from orthophoto and tree height from CHM.

3.2.2 Crown Projection Area – DBH Relationship and Validation

A relationship between CPA and DBH has been derived by performing regression analysis. From 562 CPAs (193 broadleaves and 269 conifers) that have been digitized manually, 254 trees have been used for model development and validation. The model was developed separately for broadleaves and conifers. The dataset of broadleaves and conifers was split into two parts; 90 broadleaves and 94 coniferous trees for model development and 30 broadleaves and 40 coniferous trees for model validation. *Table 12* presents all the regression models applied to determine the CPA-DBH relationship from broadleaves and coniferous trees. In the case of broadleaves, the power regression model performed better than the rest of the models at an R^2 of 0.89 with an RMSE of 4.28 cm. Binomial (2nd order polynomial) regression model performed better for the conifers at an R^2 of 0.92 with an RMSE of 2.44 cm. Therefore, the power function has been used for broadleaves, and the binomial equation has been used to determine the CPA-DBH relationship of conifers. *Figure 17* presents the scatterplot of the CPA-DBH relationship with the fitted regression function curve for broadleaves and conifers.

Table 12: Regression models applied to determine the CPA-DBH relationship of broadleaves and conifers.

	Model	Equation	R^2
Broadleaves	Linear	$y = 0.2378x + 34.569$	0.88
	Logarithmic	$y = 18.819\ln(x) - 25.305$	0.86
	Exponential	$y = 37.194e^{0.0042x}$	0.83
	Binomial	$y = -0.0003x^2 + 0.3129x + 31.432$	0.86
	Power	$\mathbf{y = 11.446x^{0.3612}}$	**0.89**
Conifers	Linear	$y = 0.4638x + 25.592$	0.9
	Logarithmic	$y = 13.711\ln(x) - 4.0136$	0.84
	Exponential	$y = 27.688e^{0.0106x}$	0.81
	Binomial	$\mathbf{y = -0.002x^2 + 0.6662x + 22.68}$	**0.92**
	Power	$y = 12.891x^{0.3436}$	0.91

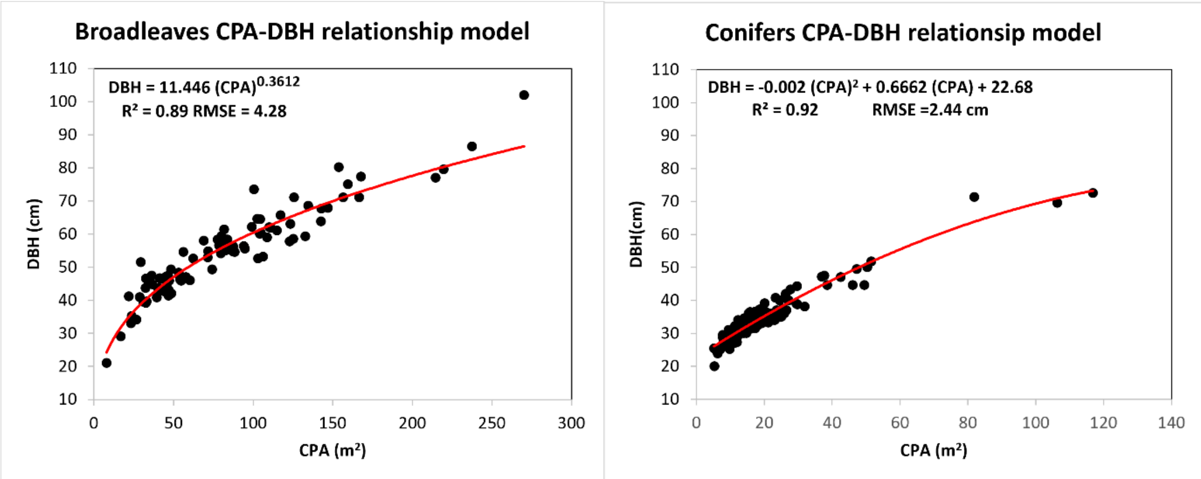

Figure 17: The regression model between CPA and DBH of broadleaves and conifers.

Each CPA-DBH relationship model developed for broadleaves and conifers has been validated on a dataset independent of the model dataset. *Figure 18* depicts the result of model validation. The validation models confirmed the correlation between biometric DBH and estimated DBH with an R^2 of 0.79 for broadleaves and 0.85 for the conifers with an RMSE of 4.76 cm and 2.06 cm accordingly. *Figure 18* also shows how the biometric DBH and estimated DBH fit compared to a 1-1 line. The dotted line represents the 1-1 line of the graph. The red line represented the fitted line from the linear regression between biometric DBH and estimated DBH. We performed a t-test between the biometric DBH and model estimated DBH and found no statistically significant difference. The results of the t-test are presented in *Appendix E*.

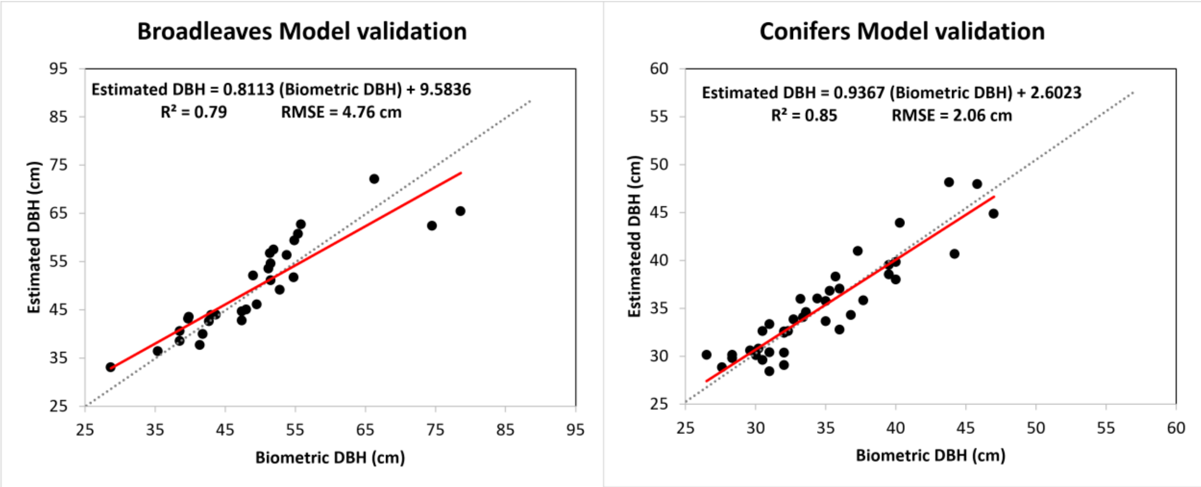

Figure 18: The regression between biometric DBH and model estimated DBH to validate the model.

3.2.3 AGB Estimation Results from UAV Parameters

DBH from the CPA-DBH relationship model and tree height from CHM has been applied to estimate AGB for individual trees. Both parameters have been used as input variables for the species-specific allometric equations provided in *Table 7*. Then the AGB of trees of each plot was summed, and the total AGB per plot was converted into tons/ha unit. *Table 13* below presents the descriptive statistics of plot AGB calculated from UAV RGB. The plot AGB ranged from 84.04 tons/ha to 472.15 tons/ha, which is also consistent with the field-measured AGB.

Table 13: Description of plot AGB estimated from UAV RGB images.

	UAV AGB
Count	57
Mean	227.83
Standard Error	10.13
Standard Deviation	76.51
Sample Variance	5853.08
Minimum	84.04
Maximum	472.15
Kurtosis	1.45
Skewness	0.77
W statistics	0.95
p-Value	0.2
Normal Distribution	True

3.2.4 Accuracy of AGB Estimated from UAV

3.2.4.1 Accuracy of Individual tree AGB Estimated from UAV

AGB of individual trees estimated from UAV RGB images using species-specific allometric equations has been plotted against the biometric AGB in *Figure 19*. The regression between estimated AGB and biometric AGB shows a positive correlation with an R^2 of 0.81 with an RMSE of 304.2 kg. Therefore, it can be implied that the DBH modeled from UAV images and height obtained from UAV CHM can explain 81% variation on field-measured DBH.

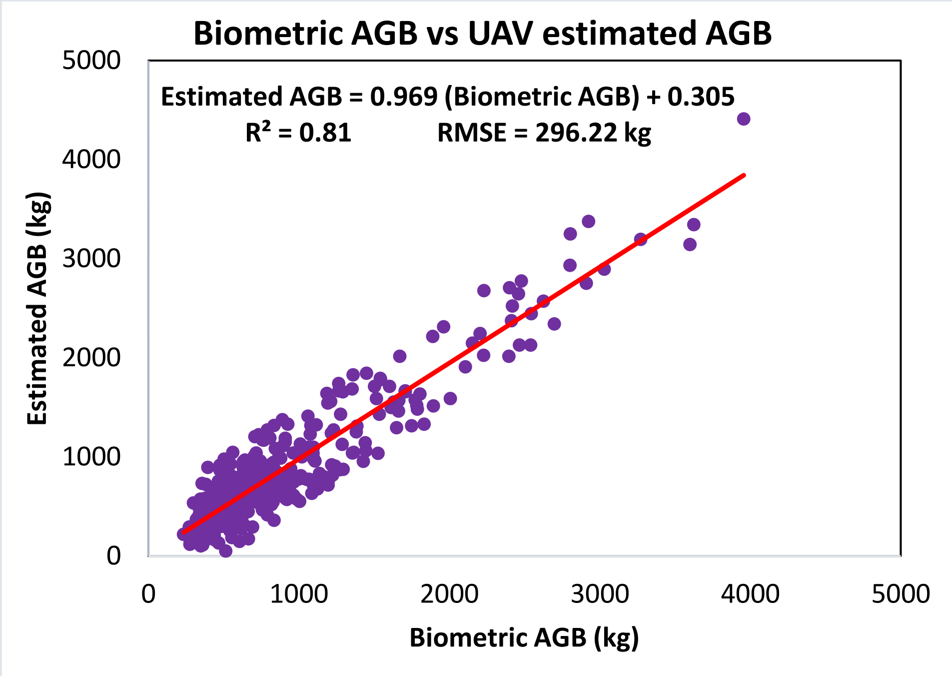

Figure 19: Linear regression between UAV estimated AGB and biometric AGB of individual trees.

3.2.4.2 Accuracy of plot AGB Estimated from UAV

On the other hand, the results of AGB estimation from accuracy assessment on plot level showed a different scenario compared to the accuracy on individual trees. A t-test between the UAV estimated AGB and the biometric AGB had been done at (α = 0.05), assuming unequal variance between both parameters. The test result showed a significant difference between the means of UAV AGB and biometric AGB. Details of the t-test are presented in *Table 14*.

Table 14: Results of the T-test between UAV estimated AGB and biometric AGB assuming unequal variance.

	UAV AGB	*Biometric AGB*
Mean	227.83	266.85
Variance	5853.08	15864.44
Observations	57	57
Hypothesized Mean Difference	0	
df	92	
t Stat	-1.999397675	
P(T<=t) one-tail	0.024257699	
t Critical one-tail	1.661585397	
P(T<=t) two-tail	0.048515398	
t Critical two-tail	1.986086317	

The AGB per plot measured from UAV parameters and biometric data have been visualized in *Figure 20*. Some plots have similar AGB as compared to the biometric data. In contrast, some plots, such as plot 5, 6, 11, 13, 15, 17, 18, 19, 20, 24, 30, 49, 50 and 51 had lower estimated AGB compared to biometric AGB. This discrepancy in estimated AGB with biometric AGB can be attributed to the number of trees that could not be assessed with UAV images. *Figure 21* also depicts the poor relationship between biometric plot AGB and UAV modeled plot AGB fitted on a 1-1 line. Regression between biometric AGB and estimated AGB resulted an R^2 of 0.35 with RMSE = 57.18 tons/ha.

The underestimation of AGB by UAV RGB images was further analyzed. It was found that UAV RGB images were able to estimate AGB of coniferous plots better than broadleaves and mixed. However, most of the underestimation was observed to be in mixed plots. The relationship between biometric AGB and UAV AGB was analyzed for coniferous, broadleaves and mixed plots. It was found that coniferous plot AGB had a higher correlation at R^2 of 0.52. Broadleaves and mixed plots depicted very poor correlation at R^2 of 0.18 and 0.02 accordingly. The regression graphs are presented in *Appendix D*.

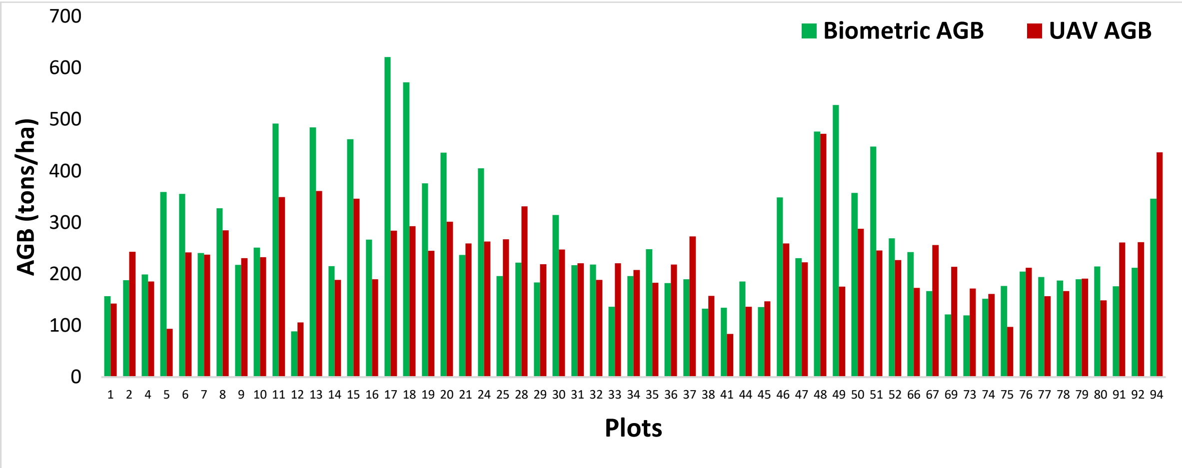

Figure 20: AGB per plot calculated from UAV parameters with a red tone and AGB estimated from biometric data with a green tone.

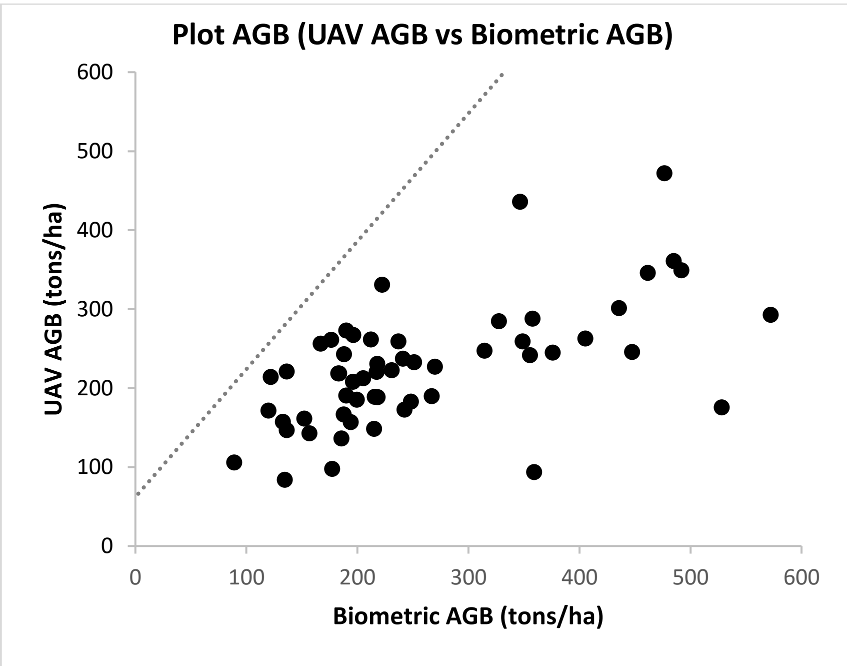

Figure 21: Scatterplot of UAV estimated AGB and Biometric AGB on the plot.

3.3 Results from AGB and PALSAR-2 Backscatter Coefficients

HH and HV backscatter coefficients from nine representative pixels from a 3x3 pixel window have been collected for each plot, and the mean of the coefficients has been calculated representing each plot. The output of regression models between HH backscatter coefficients and biometric AGB and between HV backscatter coefficients and biometric AGB has been described in the following.

3.3.1 Regression between AGB and HH Backscatter Coefficients

The linear regression analysis between HH backscatter coefficients and biometric AGB showed a weak relationship between both parameters with an R^2 of 0.43 and an RMSE of 69.95 tons/ha at a p-value of 1.98e-11. The scatterplot of the linear regression between HH backscatter and biometric AGB is presented in *Figure 22*, and the summary statistics are presented in *Appendix F*.

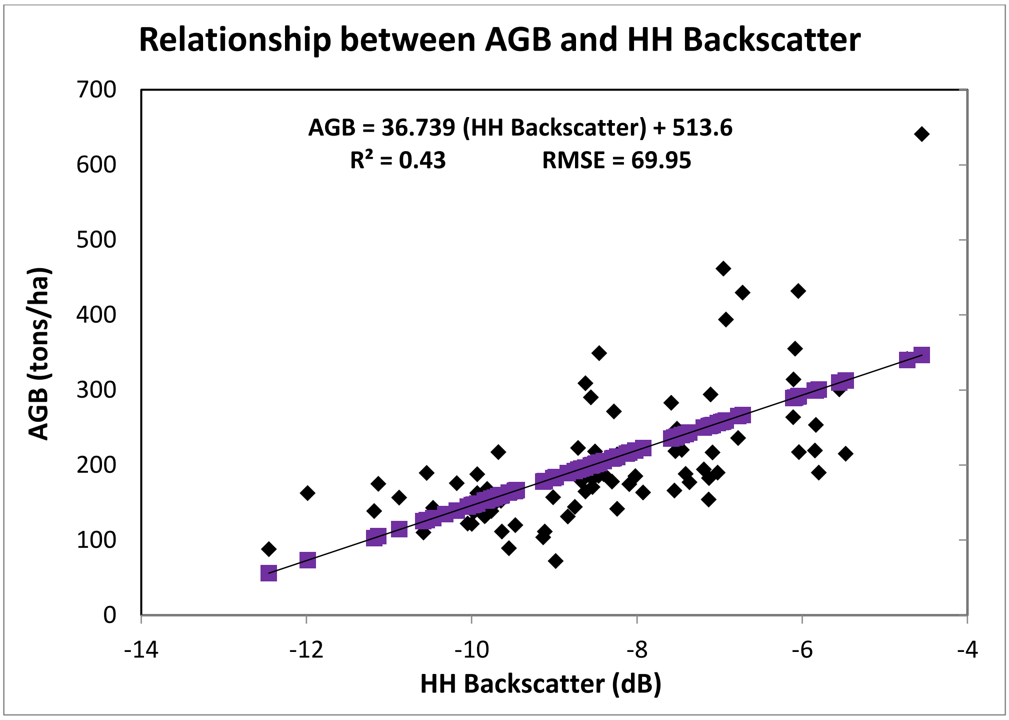

Figure 22: A linear regression to estimate AGB using HH backscatter coefficients from PALSAR-2.

A linear regression analysis between $\log_{10}$(AGB) and HH backscatter has also been performed to estimate AGB. This regression was performed to complement the values of HH backscatter in dB obtained by applying a logarithmic formula. The regression analysis also showed a weak relationship between HH backscatter and $\log_{10}$(AGB) with an R^2 of 0.47 at a p-value of 6.66e-13. The regression backscatter is presented in *Figure 23*, and the summary statistics in *Appendix G*.

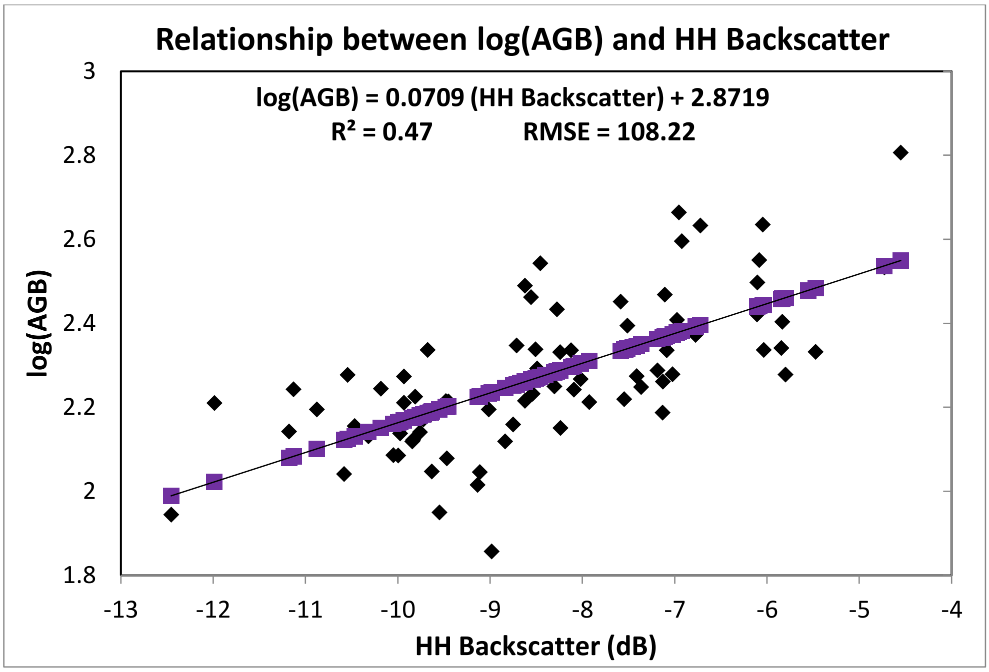

Figure 23: A linear regression between HH Backscatter coefficients and log(AGB).

3.3.2 Regression between AGB and HV Backscatter Coefficients

The linear regression between HV backscatter coefficients and biometric AGB showed a better relationship than regression using HH backscatter coefficients. The regression has shown an R^2 of 0.74 with an RMSE of 47.39 ton/ha at a p-value of 3.09e-25. *Figure 24* below presents the scatterplot of the linear regression between HV backscatter coefficients and biometric AGB. The summary statistics of the regression are depicted in *Appendix H*.

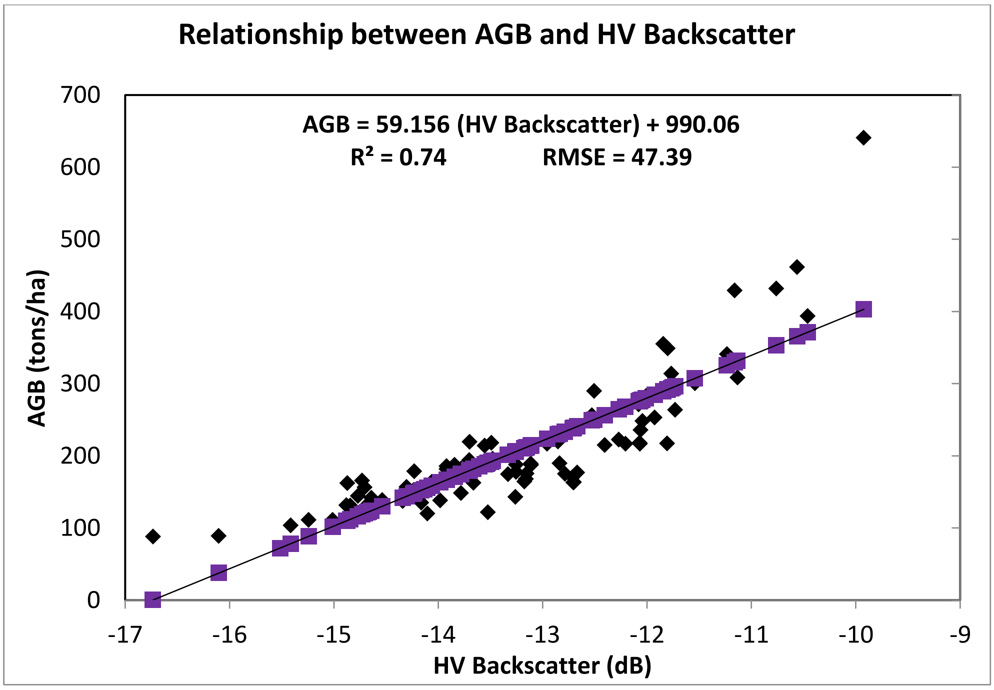

Figure 24: A linear regression between PALSAR-2 HV backscatter coefficients and biometric AGB.

Similar to the HH backscatter, a linear regression between $\log_{10}$(AGB) and HV backscatter has also been performed. The linear regression showed a strong relationship between both parameters with an R^2 of 0.84 at a p-value of 1.27e-33. The scatterplot or regression between HV backscatter coefficients and biometric AGB is presented in *Figure 25*. The summary statistics of the regression are also presented in *Appendix I*.

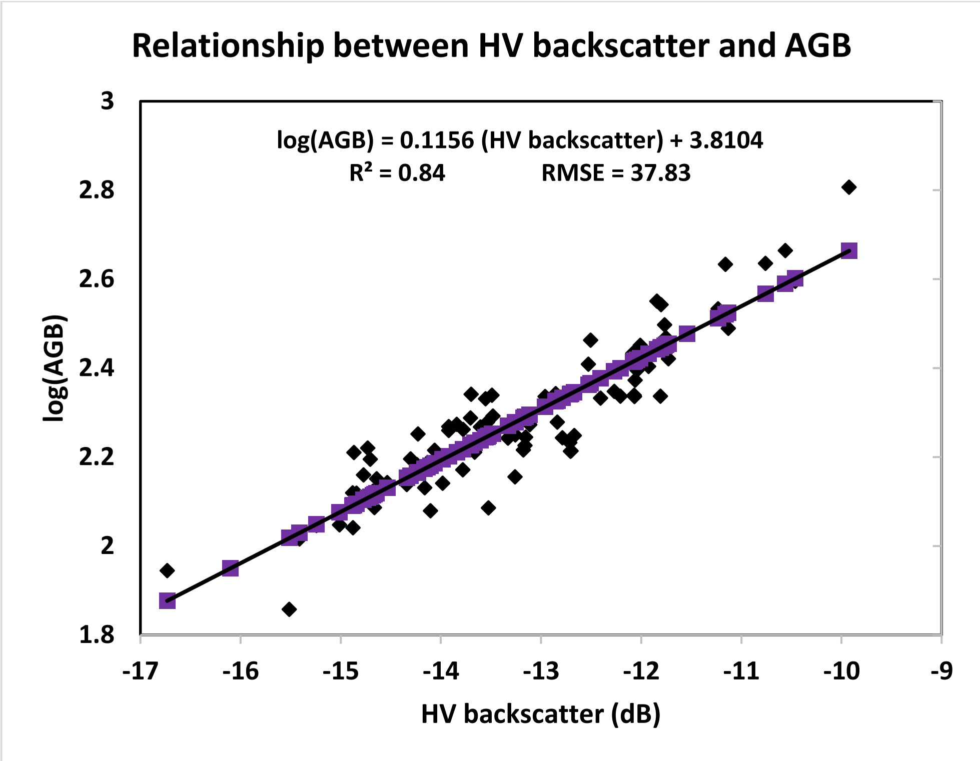

Figure 25: A linear regression between PALSAR-2 HV backscatter coefficients and log(AGB).

3.3.3 Model Development

The regression analysis among HH and HV backscatter coefficients and biometric AGB showed that the linear regression between HV backscatter coefficients and $\log_{10}$(AGB) has the most robust relationship. Therefore, a simple linear regression model has been developed using the $\log_{10}$(AGB) and HV backscatter coefficients to estimate AGB using HV backscatter. The dataset has been split into two parts to develop the model and validate it; 50 observations for model development and 33 observations for model validation. The regression model between logarithmic AGB and HV backscatter depicted a high accuracy with an R^2 of 0.85, which implies that the model explains 85% of the variation in logarithmic AGB. The graphical representation of the model is depicted in *Figure 26*, and the summary statistics of the linear regression are shown in *Table 15*.

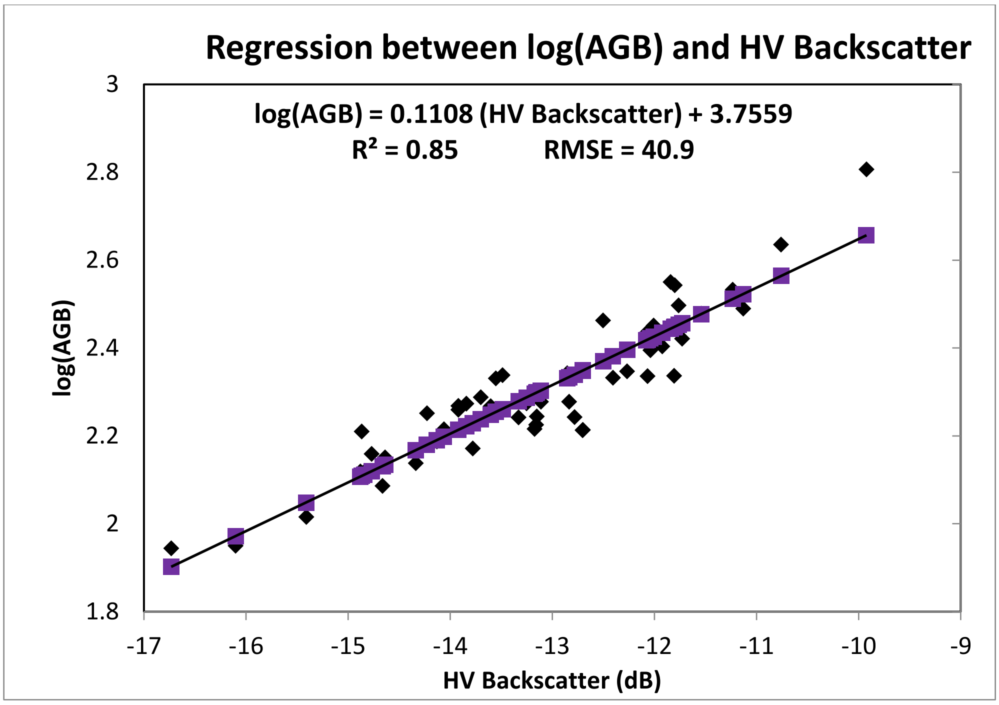

Figure 26: A linear regression between PALSAR-2 HV backscatter coefficients and log(AGB).

Table 15: Summary statistics of regression between HV backscatter coefficients and log(AGB) for model development.

SUMMARY OUTPUT

Regression Statistics	
Multiple R	0.92
R Square	0.85
Adjusted R Square	0.85
Standard Error	0.07
Observations	50

ANOVA

	df	SS	MS	F	Significance F
Regression	1	1.16	1.16	273.20	1.90553E-21
Residual	48	0.20	0.004		
Total	49	1.36			

	Coefficients	Standard Error	t Stat	P-value
Intercept	3.76	0.09	42.39	1.07583E-39
HV_Backscatter	0.11	0.01	16.53	1.90553E-21

3.3.4 Model Validation and Accuracy Assessment

The regression model developed in section 3.3.3 has been used to estimate AGB on a logarithmic scale. The model has been applied on 33 plots separated for validation. The validation dataset was independent of data used in the model development, and the accuracy of the model has been assessed by estimating AGB on validation data using the regression equation.

The results of regression between biometric (observed) AGB and model estimated AGB on validation dataset showed a positive relationship at an R^2 of 0.86 at a p-value of 9.6-15 with an RMSE of 26.63 tons/ha. Thus, it can be implied that the model developed to estimate AGB is consistent and can explain 86% variability in the validation dataset. The scatterplot of the regression analysis is shown in Figure 27, and the summary statistics of the model validation are shown in *Appendix J*.

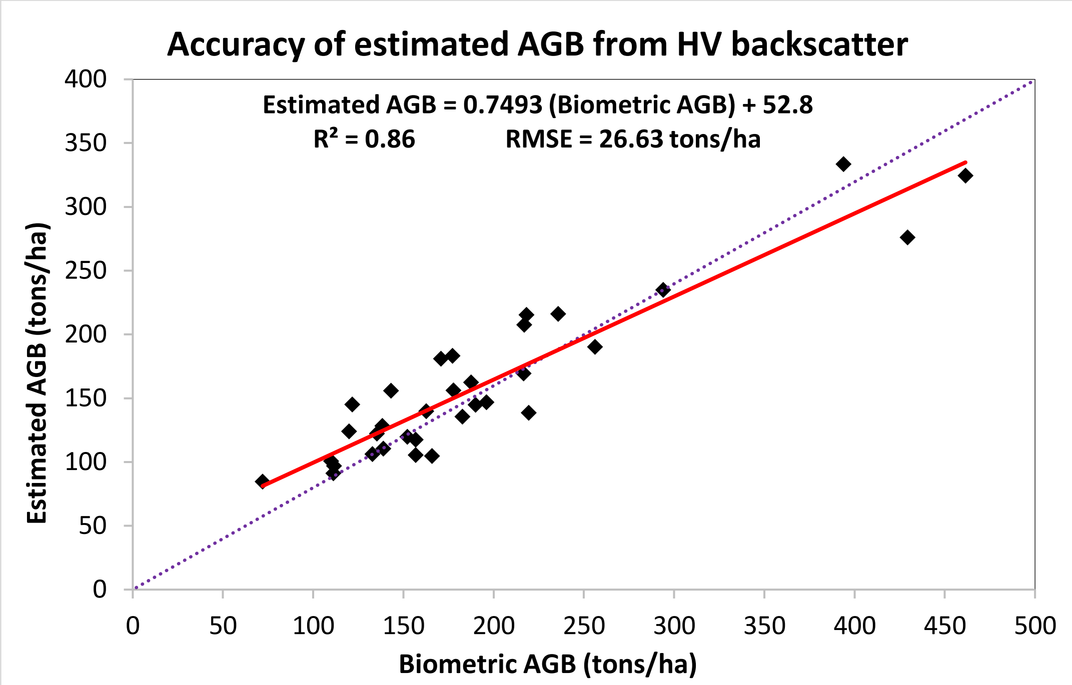

Figure 27: The regression model validation between biometric AGB and estimated AGB.

3.3.5 Plot AGB estimate from ALOS-2 PALSAR-2 image

AGB of plots has been modeled from HV polarization ALOS-2 PALSAR-2 backscatter coefficients. The AGB values were modeled in logarithmic form from the relationship model between HV backscatter coefficients and log10(AGB). The $\log_{10}$(AGB) values have been transformed into AGB in tons/ha unit. The PALSAR-2 images modeled plot AGB with an average of 205.67 tons/ha. The plot AGB ranged from 79.77 tons/ha to 453.37 tons/ha. *Table 16* represents the summary of AGB modeled by the ALOS-2 PALSAR-2 image.

Table 16: Summary of AGB modeled by ALOS-2 PALSAR-2 image on plots.

ALOS-2 PALSAR-2 estimated AGB	
No of plots	83
Mean	205.67
Standard Error	8.027
Standard Deviation	73.13
Sample Variance	5347.60
Minimum	79.77
Maximum	453.37
Kurtosis	0.99
Skewness	0.97

3.3.6 Estimation of Saturation Point

A logarithmic regression between AGB and HV backscatter coefficients has been plotted in *Figure 28*. The logarithmic regression curve is presented in the purple curve in the graph. The slope of the logarithmic curve was calculated from changes in AGB with respect to changes in HV backscatter coefficients. At the AGB of 157.2 tons/ha, the slope of the curve converges at 0.02. However, with increasing AGB values, the slope decreases, and at 314.4 tons/ha AGB the slope of the logarithmic curve converges at 0.01, which can be seen with the vertical red line in *Figure 28*.

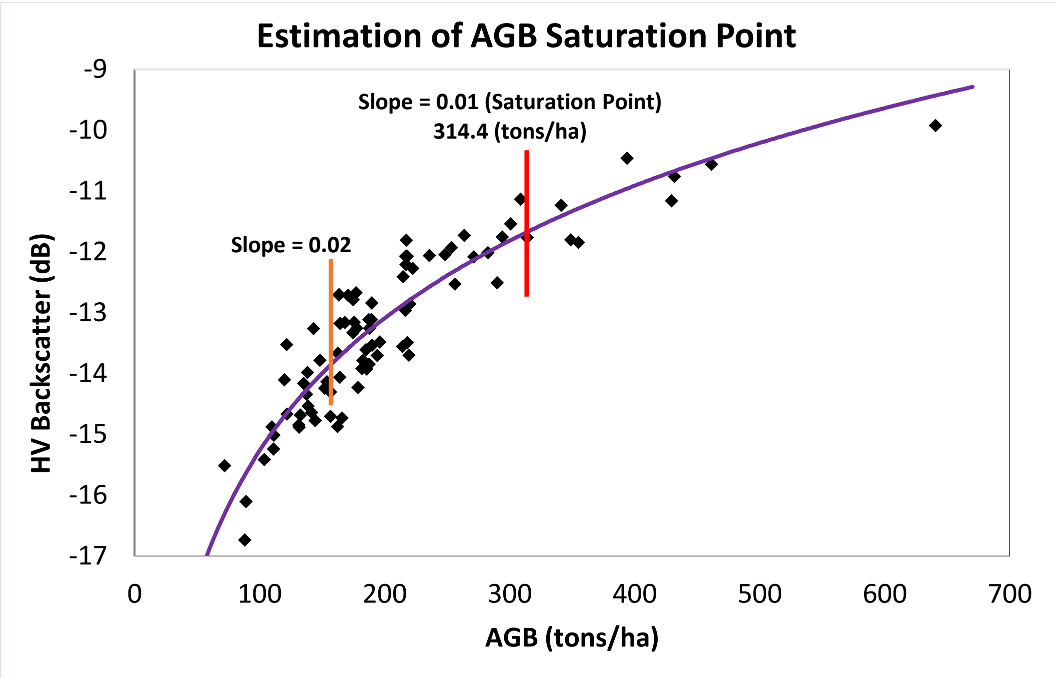

Figure 28: Determination of AGB saturation point with respect to HV backscatter coefficients.

3.3.7 Backscatter – AGB relationship on Coniferous, Broadleaf, and Mixed Forest

AGB modeled by HV backscatter coefficients for conifers, broadleaves, and mixed plots were plotted against biometric AGB of the same plot. AGB modeled on conifers showed the most robust relationship compared to broadleaves and mixed dominated plots. The linear regression models between modeled AGB and biometric AGB on broadleaves, conifers, and mixed forest plots resulted in R^2 of 0.82, 0.90, and 0.81 correspondingly with RMSE of 38.44 tons/ha, 45.05 tons/ha, and 31.67 tons/ha. The backscatter plot of the regression between modeled AGB and biometric AGB for broadleaves, conifers, and mixed plots are presented in *Figure 29*.

The performance of HV backscatter coefficients to model AGB on broadleaves, conifers, and mixed are generally consistent with all plot types combined. Based on the linear regression results, it can be implied that conifers stand can be modeled more accurately compared to broadleaves or a mixed forest stand.

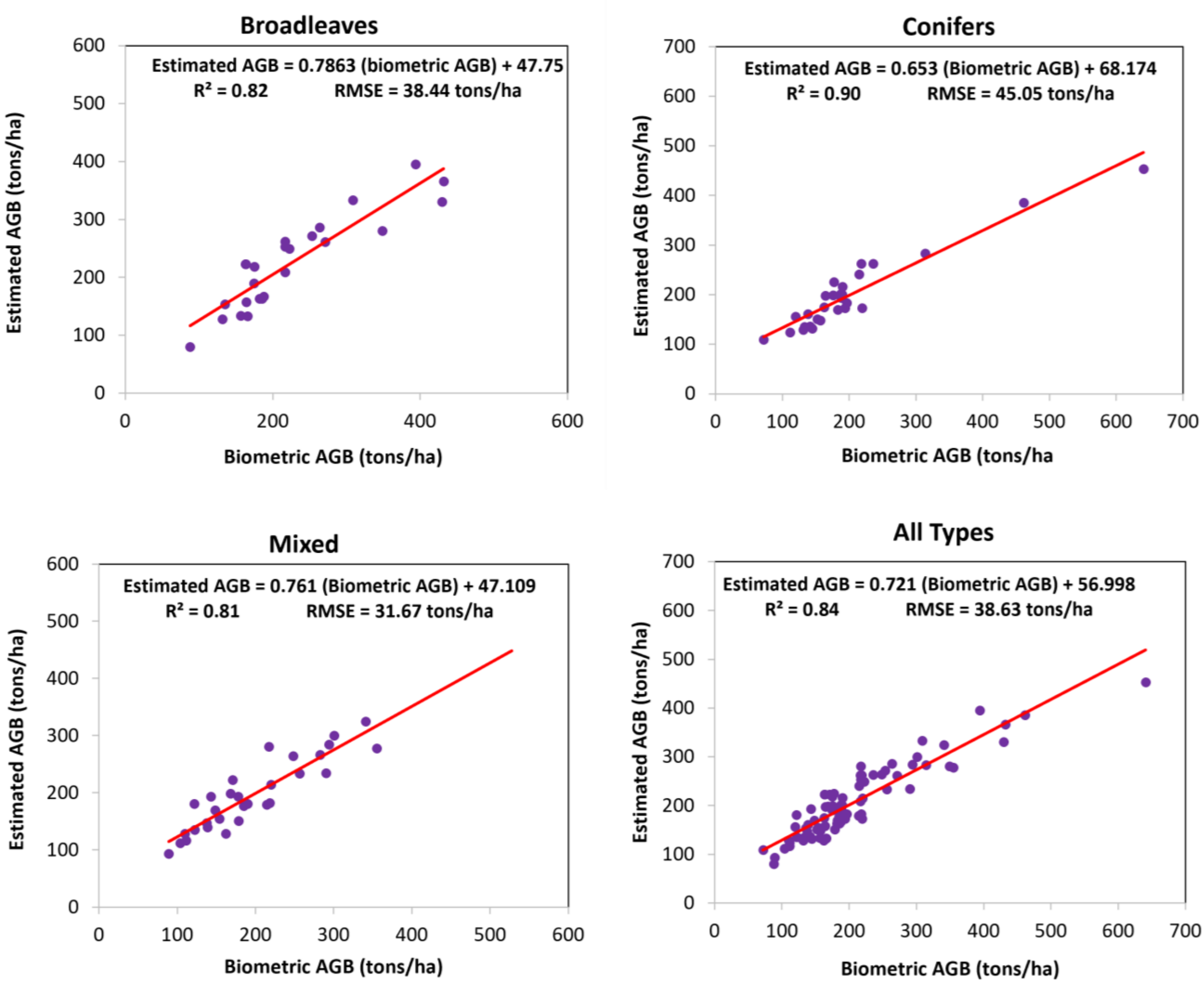

Figure 29: Relationship of HV backscatter modeled AGB and biometric AGB on broadleaves, conifers, and mixed plot.

3.4 Comparing AGB Estimation from UAV and ALOS-2 PALSAR-2

Forty-nine plots were common in the modeling and estimation of AGB from UAV and PALSAR-2 images. A one-way ANOVA test among the biometric AGB, UAV estimate AGB, and PALSAR-2 estimated AGB was conducted to determine whether there is any statistically significant difference between the means of AGB from these three sources of estimation methods. The result of the one-way ANOVA F-test showed no statistically significant difference of mean AGB from the field, AGB estimated from UAV, and the AGB estimated from PALSAR-2 ($F(2,144) = 0.02$, $p = 0.99$). *Table 17* presents the result of the one-way ANOVA test. However, we cannot rely on the result of this statistical analysis. Plot AGB estimated from PALSAR-2 had high accuracy ($R^2 = 0.85$), where plot AGB modeled from UAV showed very poor relationship ($R^2 = 0.35$) with reality. Therefore, technically, AGB poorly modeled from UAV cannot be compared with more accurate AGB modeled from PALSAR-2.

Table 17: One-way ANOVA test of AGB from the field, UAV, and PALSAR-2.

SUMMARY

Groups	Count	Sum	Average	Variance
Field AGB	49	10625.3	216.84	7574.04
SAR AGB	49	10636.32	217.07	5264.11
UAV AGB	49	10742.92	219.24	5045.31

ANOVA

Source of Variation	SS	df	MS	F	P-value	F crit
Between Groups	172.24	2	86.12	0.01	0.99	3.06
Within Groups	858406.33	144	5961.16			
Total	858578.57	146				

Even though the mean is not statistically significant, we have visualized AGB from each plot in *Figure 30* to understand the estimation of AGB from different plots. We have split the column chart according to forest structure: coniferous, broadleaves and mixed. The column chart showed that UAV underestimated AGB in many plots due to the exclusion of suppressed trees. However, UAV also overestimated some plots, resulting in a higher mean AGB value almost equivalent to the mean of biometric AGB and PALSAR-2 AGB. The column charts also showed that AGB estimated from PALSAR-2 is consistently close to the biometric AGB in each plot.

In *Figure 31*, the columns represent the percentage of residuals of plot AGB estimated by UAV and PASLAR-2 images. The negative axis indicates the underestimation of AGB, and the positive axis indicates the overestimation of plot AGB. The overestimation or underestimation of AGB is higher in the UAV model than in the PALSAR-2 model.

The visualization in *Figure 30* and *Figure 31* depicted that the overestimation or underestimation of AGB modeled by UAV RGB images is mostly in broadleaf and mixed plots. The highest underestimation was observed in plot 5, which was a mixed forest stand. Plot 67 and plot 94 depicted very high overestimation by UAV. Both of these plots are dominated by broadleaves. In most of the coniferous stands, UAV was able to identify all the trees in a plot; therefore, the plot AGB estimated from the UAV was similar to the biometric plot AGB. It was also depicted that PALSAR-2 underestimated AGB in plots with higher biometric AGB and overestimated AGB in most plots with lower AGB values.

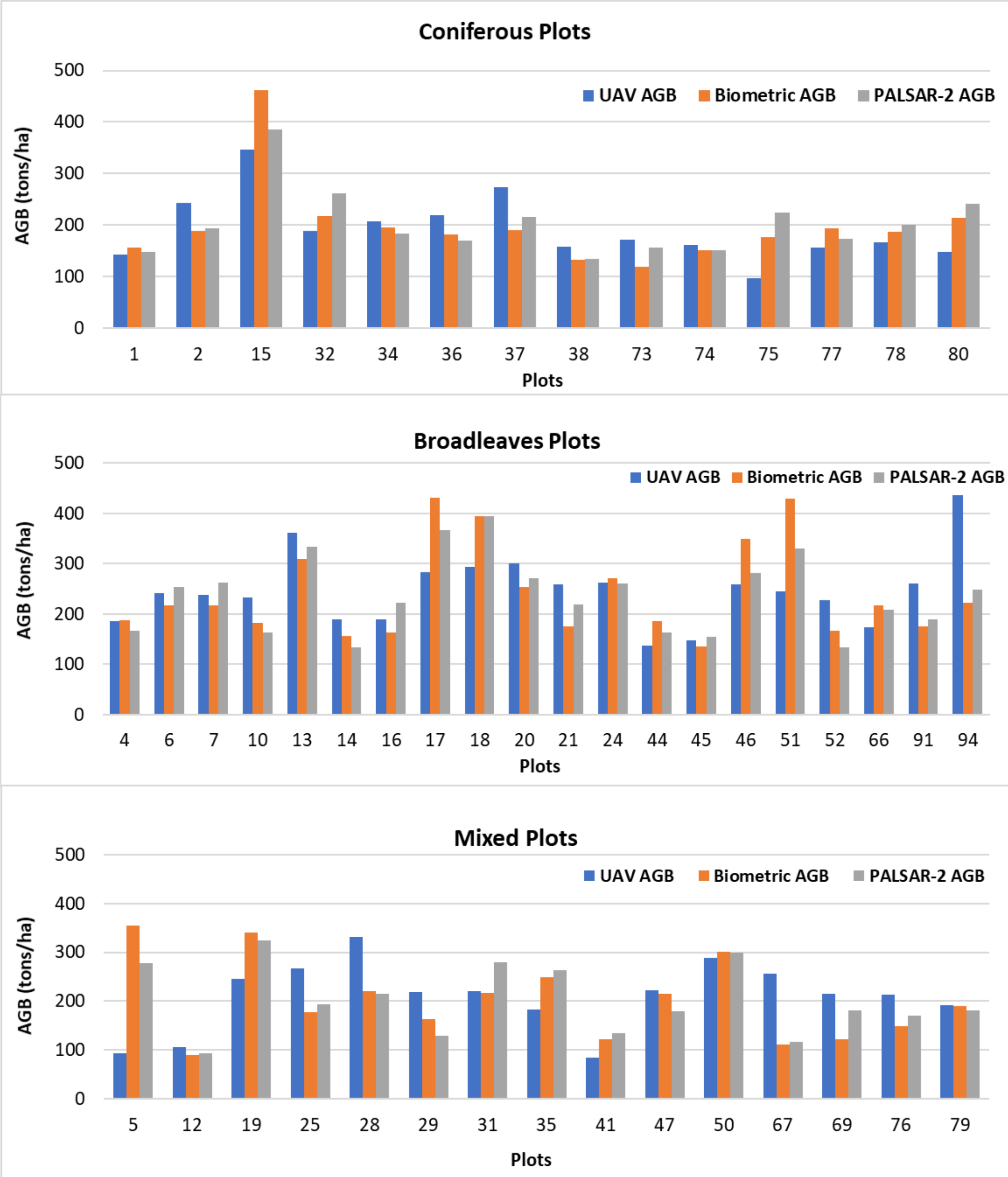

Figure 30: Biometric AGB, UAV estimated AGB and PALSAR-2 estimated AGB for plots.

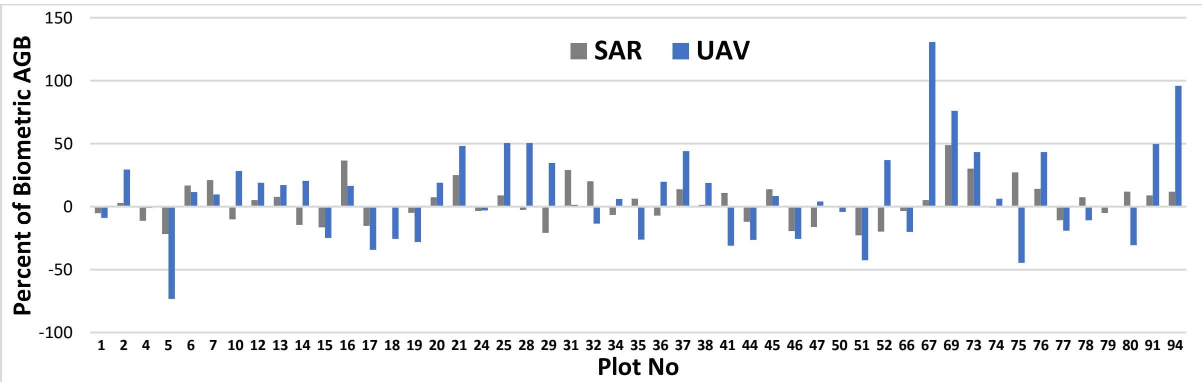

Figure 31: Percentage of residuals of plot AGB estimated by UAV and PALSAR-2 images.

4 DISCUSSION

Our study used two remote sensing methods to estimate AGB on an area basis (tons/ha). UAV RGB and PALSAR-2 images are depicted to estimate AGB in many studies (Berhe, 2018; Nguyen, 2010; Poley & McDermid, 2020; Stelmaszczuk-Górska et al., 2018). However, UAV RGB based AGB assessment is an individual tree based approach (Mlambo et al., 2017a; Poley & McDermid, 2020; Shashkov et al., 2019) where PALSAR-2 backscatter is based on the mean AGB of an area (Beaudoin et al., 1994; Joshi et al., 2015; Watanabe et al., 2006). Nevertheless, the resolution of PALSAR-2 is much lower than the resolution from UAV. The limitations and advantages of both sensors have drawn us to compare the AGB estimated from both sensors.

Accurate estimation of AGB from field data is crucial to develop the AGB estimation models and to validate the output of modeled AGB from UAV and PALSAR-2. This study used species-specific allometric equations to calculate the AGB of individual trees from field-measured data. The same allometric equations were used to estimate AGB from UAV RGB images. However, in the case of PALSAR-2, plot AGB has been used from field-measured individual tree AGBs. Most of the allometric equations were taken from Zianis et al. (2005). Allometric equations that were developed for the Netherlands were prioritized. Moreover, while selecting the allometric equations, we also focused on the range of DBH and tree height that was used by the studies. Tree species such as *Fagus sylvatica* and *Pseudotsuga menziesii* had allometric equations developed from the Netherlands. Allometric equations for the rest of the trees were developed on the forests of different countries. However, we have chosen the equations from a similar biome. It was challenging to find suitable allometric equations based on the range of DBH and height in our field data. Our field data has DBH ranged from 10 cm to 101 cm, where most of the allometric equations were developed from comparatively younger trees (Bunce, 1968; Cienciala et al., 2006; Djomo & Chimi, 2017; GlobAllomeTree, 2021; Hack & Goodlett, 1960; Novák et al., 2011; Zianis et al., 2005). Therefore, we selected the allometric equations that represent the similar forest biome with the range of DBH as close as possible with the range of our biometric measurements. Moreover, we have cross-checked our AGB estimations with the previous AGB estimation studies conducted in the same study area (Gaden, 2020; Torres Rodriguez, 2020). We found that our results were consistent with the previous studies.

Our study used species-specific allometric equations with DBH as the only parameter to calculate the AGB of tree species except for Beech (*Fagus sylvatica*). Chave et al. (2005) argued that the AGB of trees in a temperate forest could be estimated using simple relationship models without using height information rather than complex models. Many studies have found that DBH is a highly related variable to AGB and can be used alone in AGB estimation (Brown, 1997a; Bunce, 1968; Chave et al., 2005; Djomo & Chimi, 2017; Jucker et al., 2017; Zianis et al., 2005). Moreover, the estimation of tree height in the field can be challenging due to branches' canopy density and interference while trying to see the top. However, we have used DBH and height as variables to estimate AGB for one species: Beech. Most of the allometric equations for Beech were suitable for a smaller DBH range; therefore, we have decided to use DBH and height in the allometric equation for Beech.

4.1 Estimation of AGB using UAV RGB images

The first objective of our study was to model and estimate aboveground biomass using UAV RGB images. Several approaches could have been chosen to model AGB from UAV. Our approach was to model individual tree AGB based on the tree crown projection area. We have chosen this approach because it a standard method of estimating AGB from UAV images (Poley & McDermid, 2020). The output of the AGB estimation from UAV RGB depends on several processing steps and the quality of data. Therefore, we ensured high quality data by applying maximum overlap while collecting UAV images so that the point cloud with high quality can be achieved.

4.1.1 Estimating DBH from CPA-DBH Models

In this study, non-linear functions showed a better relationship between CPA-DBH than the linear function. The power model provided a higher coefficient of determination (R2) of 0.89 with RMSE 4.28 cm for broadleaves. Moreover, the quadratic function has resulted in being the model that best described the CPA-DBH relationship for conifers (R^2 = 0.92, RMSE = 2.44 cm). Shimano (1997) argued that the linear relationship model between CPA-DBH might not be acceptable despite having a good fit in a closed canopy system. The forest of our study area is a closed canopy system which is why the non-linear CPA-DBH relationship model depicted a better fit.

The use of a polynomial function to fit the tree growth parameter such as the crown, DBH is often considered unrealistic to the situation (Chave et al., 2005; Shimano, 1997; Venus & Causton, 1979). Venus & Causton (1979) argued that low-degree polynomial functions such as binomial function seem to over-simplify the situation to a linear function, and models fitted with high-degree polynomial functions are often biologically unfeasible. Our study used a second-order polynomial function to fit the model to estimate DBH from CPA for conifers. Besides, according to Shimano (1997), the second order polynomial model is more fitting due to the assumptions of the "unit-pipe system" described by (Shinozaki et al., 1964). The trees in our study area were densely planted. In a dense forest stand, the relationship between CPA-DBH is proportional when the tree is young, and they compete for canopy area after growing at a certain age (Shimano, 1997). Thus, the canopy growth rate becomes slower. In a closed forest, the rule of "self-thinning" (White, 1981) also applies, which influenced the CPA-DBH relationship. Moreover, Shimano (1997) concluded that the relationship between crown projection area and DBH could be described better using a power-sigmoid model. Our study has found that the power model described the CPA-DBH relationship in broadleaf trees. Other non-linear functions also depicted closer values of the coefficient of determination and RMSE to the selected models. The best fit models that have been used to estimate DBH from CPA were chosen based on the statistical performance of the models. Higher coefficient of determination and less root mean square error (RMSE) were considered to choose the model that can best describe the relationship between parameters.

Previous studies on the study area have also found strong relationships between CPA and DBH of the trees. Torres Rodriguez (2020) found that a power function with an R^2 of 0.87 and RMSE 4.55 cm can describe the CPA-DBH relationship in conifers, and a second-order polynomial function with an R^2 of 0.85 and RMSE 6.15 cm can describe the CPA-DBH relationship of broadleaf species. Our findings are also consistent with the findings of Torres Rodriguez (2020).

4.1.2 AGB modeled from UAV

DBH of trees from 57 plots was estimated from the CPA-DBH relationship, and the species-specific allometric equations used to calculate biometric AGB were used to estimate the AGB of trees. The regression between biometric AGB and UAV estimated AGB showed that UAV estimated AGB could explain 81% variation in biometric AGB. However, the result of the t-test between biometric AGB and UAV estimated AGB showed a statistically significant difference between the means of both AGB measurements; see *Appendix K*. The difference in AGB measurements can be attributed to the generalization of estimated DBH from the CPA-DBH relationship models. We used one general CPA-DBH relationship model for all conifers and one for broadleaves rather than using species-specific CPA-DBH relationships.

From the comparison between biometric AGB and UAV estimated AGB on plots, it was observed that there is a discrepancy between both measurements, evident from Figure 20 and Figure 21. Therefore, we analyzed the estimated AGB further to explain the situation. We assessed the relationship between both measurements based on forest types: conifers, broadleaves, and mixed. The regression analysis between biometric AGB and UAV modeled AGB resulted in an R^2 of 0.46 for conifers plots, 0.4 for broadleaves plots and 0.14 for mixed plots. Details of the regression are presented in *Appendix L*. During fieldwork, we have recorded trees with DBH of 10 cm or higher that were suppressed under a large tree. The trees that were concealed from above by taller trees could explain the poor relationship between UAV modeled plot AGB and field-measured plot AGB. This phenomenon was observed mostly on mixed forest stands; large broadleaves concealed many conifers in the forest. We also noticed that in pure broadleaf plots, trees like Birch (*Betula pendula*), Beech (*Fagus sylvatica*) were concealed entirely or partially by more large Beech or Oak (*Quercus petraea*) trees. Similarly, large conifers also suppressed smaller trees, mostly in dense conifer stands.

Plots at which the AGB was underestimated by UAV were 5, 6, 11, 13, 15, 17, 18, 19, 20, 24, 30, 49, 50 and 51 (see *Figure 20*). We checked their canopy density and forest species type. We have found that most of them are broadleaves and mixed; only "Plot 15" was coniferous. The overall canopy density of these plots ranged from 66-91%. We also cross-checked the number of trees recorded in-field for these plots with the number of trees measured by UAV. We found that at least two trees were excluded from modeling by UAV in those plots. Plot 5, 7, 18, and 49 showed high underestimation. For example, only two out of 18 trees were measured by UAV in plot 5 (*Figure 32*). In plots 17 and 18, large trees with 40-50 cm of DBH were not assessed by UAV and lead to high underestimation.

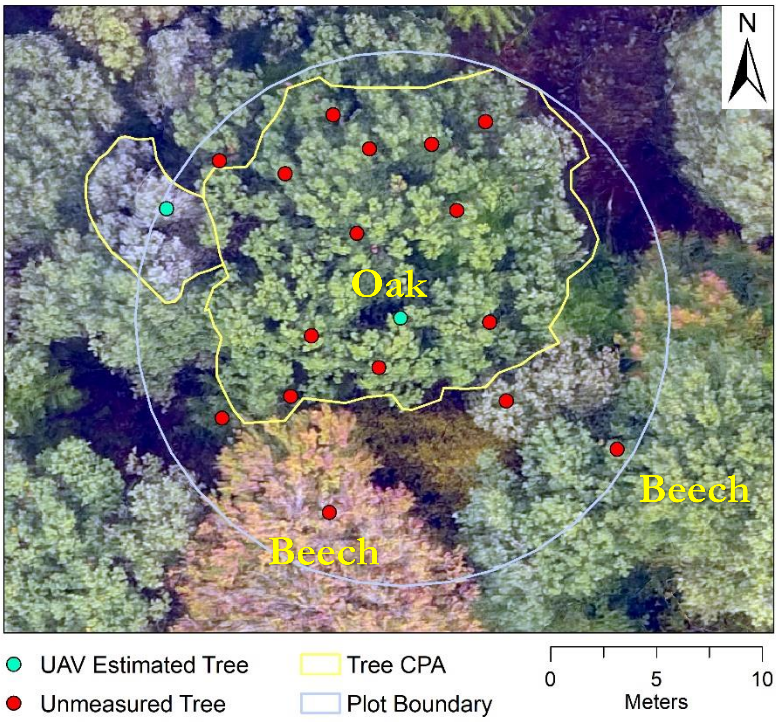

Figure 32: Example of trees concealed by taller Beech or Oak trees in a plot.

AGB was overestimated by UAV in some plots: 25, 28, 33, 37, 67, 69, 91, and 94. These plots also had a similar canopy density range as the plots underestimated by UAV. We also checked the number of trees assessed by UAV; most of the plots had trees not measured by UAV. However, the DBH of trees in those plots was overestimated by the CPA-DBH relationship, leading to the overestimation of AGB. It is worth mentioning that the study area is a combination of semi-natural forest and a production forest. We did not separate trees from the semi-natural and production area. The semi-natural forest mostly contained the mixed and broadleaves plots where the production forest is mostly coniferous stands. Besides, stem density in production forest is higher than the semi-natural forest, but the canopy density in the semi-natural forest are mostly higher than the coniferous stands. In our analysis, we did not consider the rule of self-thinning in the assumptions. Thus, we are unsure whether there is any difference in the CPA-DBH relationship for the semi-natural and production forest.

To explain the overestimation, we further analyzed the species-specific AGB estimation by UAV. We have found that Beech was the broadleaf species that were overestimated by the allometric equation used from DBH and height estimated by UAV. Moreover, Beech was the most frequent species in plots that were overestimated by UAV. Torres Rodriguez (2020) also found similar properties of Beech overestimated by the CPA-DBH relationship in the same study area. The overestimation of Beech could be attributed to the misjudgment of the crown while delineating the CPA. In a Beech-dominated plot, it is difficult to identify the borders between two crowns. It could have happened that crowns of partially visible crowns were included in the CPA delineation due to the smooth surface of the Beech canopy on the Orthomosaic. The inclusion of the partial crown of Beech could lead to a higher modeled DBH value, resulting in an overestimated AGB. Douglas-fir (*Pseudotsuga menziesii*) was the coniferous species that overestimated AGB from UAV based model. UAV overestimated AGB on plot 33 and 37, which were pure Douglas-fir stand. In the field, Douglas-fir was the most frequent coniferous species in mixed forest stands where they compete for the crown area with broadleaves. In-field, many Douglas-fir trees with large DBH in mixed forest stands have a smaller crown diameter or area compared to similar trees in coniferous stands. The small crown area could be due to the occlusion by broadleaves. Trees with large DBH and small crown projection area in mixed plots could have led to the overestimation of AGB in the coniferous plots.

4.2 Estimating AGB using PALSAR-2 image

Literature often studied the relationship between backscatter and AGB using linear functions (Collins et al., 2009; Ji et al., 2020; Nesha et al., 2020) and logarithmic functions (Masolele et al., 2018; Schlund et al., 2018; Stelmaszczuk-Górska et al., 2018). Therefore, we also used linear and logarithmic relationship models to estimate AGB from backscatter coefficients. The relationship between the biometric AGB and backscatter coefficients is further discussed in sub-section 4.2.1. The relationship model was also affected by the selection of plot representative pixels from the backscatter images. We had to make some assumptions while fitting a 3 x 3 window to extract backscatter coefficients. The assumptions and uncertainties of plot backscatter coefficients extraction are described in sub-section 4.2.2.

4.2.1 Relation between Backscatter Coefficients and AGB

Our findings depicted higher relationship between HV backscatter coefficient and AGB ($R^2 = 0.74$) over HH backscatter coefficient with AGB ($R^2 = 0.43$) using linear regression. On the other hand, $\log_{10}$(AGB) and backscatter coefficients revealed a better relationship with a higher coefficient of determination ($R^2 = 0.86$ for HV backscatter and $R^2 = 0.47$ for HH backscatter) and low RMSE. Both linear and logarithmic regression depicted a significant relationship between AGB and HV backscatter coefficients. Many studies have reported a logarithmic relationship between backscatter coefficients and AGB (Dobson et al., 1992; Hamdan et al., 2014; Mitchard et al., 2009). The scatterplot between HV backscatter coefficients and AGB in *Figure 28* clearly shows that the relationship between HV backscatter and biometric AGB is non-linear. Therefore, we applied a logarithmic relationship between HV backscatter and biometric AGB. Since we transformed the AGB into $\log_{10}$(AGB), the regression between backscatter coefficients and $\log_{10}$(AGB) was transformed to linear.

The inherent properties of HV backscatter allowed estimating biomass more accurately; HV backscatter is less influenced by soil moisture, vegetation moisture, and topography (Beaudoin et al., 1994; Collins et al., 2009; Mitchard et al., 2009; Sandberg et al., 2011; Van Zyl, 1993). In the HV polarization combination, the signal is transmitted horizontally and received vertically by the sensor. The signal transmit and receive method allowed to assess volume information of the forest, mainly canopy with branches. Ji et al. (2020) studied the sensitivity of L-band HV polarization backscatter in assessing forest structure. They found that the HV backscatter is sensitive to canopy density; mean canopy density from 40% or higher resulted in higher correlations with backscatter while canopy density below 40% showed moderate correlations.

Our analysis revealed the relationship between HV backscatter and AGB for different forest stand structures, such as conifers, broadleaves, and mixed (see *Figure 29*). We have found a higher relationship with conifers ($R^2 = 0.9$) than broadleaves ($R^2 = 0.82$) or mixed ($R^2 = 0.81$). Yu & Saatchi (2016) studied the sensitivity of L-band SAR backscatter to the AGB estimation. They found that backscatter has enhanced sensitivity to the temperate conifers over other forest types. Hussin et al. (1991) were able to explain 97% of the variability in slash pine ABG in their study by using simultaneous linear equations. Our study also affirms a strong relationship between backscatter and AGB in the conifers using a logarithmic relationship. Golshani et al. (2019) studied the relationship of PALSAR-2 parameters with AGB of broadleaves forest. They concluded that the relationship of backscatter coefficients is affected by the forest structure, and different models are required to estimate AGB more reliably. Imhoff (1995) compared the response of backscatter for broadleaves, conifers, and combined forest structure. The results found by Imhoff (1995) showed a higher relationship between HV backscatter and conifers at $R^2 = 0.96$ compared to broadleaves at $R^2 = 0.83$ and combined at $R^2 = 0.73$. However, Imhoff (1995) used the third-order polynomial regressions function to derive those relationships, where we used logarithmic relationships. Imhoff (1995) found that the crown layer of the forest dominated the backscatter at a higher biomass level. He also referred to the shape and structure of crowns; the soil surface is obscured in the backscatter for the dense crown.

In the field, we have measured 94 plots representing conifers, broadleaves, and mixed stand. However, we have used only 83 plots in analysis using backscatter coefficients. The plots that were excluded from analysis were open forests with low canopy density and canopy gaps. These plots with sparse vegetation or canopy gaps reflected similar to or even more than the plots with high AGB (Beaudoin et al., 1994). Hamdan et al. (2014) and Masolele et al. (2018) also found a similar phenomenon. They depicted that the relationship between AGB and backscatter coefficients is explained better with continuous AGB instead of forests with sparse vegetation. Some of the excluded plots were dense yet not included due to inaccurate measurement of plot location; uncertainty due to the use of the 'Avenza Map'.

The AGB–backscatter relationship was developed based on a circular plot with a 12.62 m radius to have about 500 m^2 area per plot. The resolution of the PALSAR-2 image was 7x7 m; thus, a 3x3 pixel square was used to obtain plot backscatter coefficients (more details in section 4.2.2). Similar plot size and shape were also used in studies to model AGB from L-band backscatter (Hamdan et al., 2014; Masolele et al., 2018; Nesha et al., 2020). Moreover, the study area forest was comparatively homogeneous, mainly in the production forest area. In our field data, most plots consist of trees of only one or two species; almost every pure coniferous or broadleaves plot observed had the same situation. Besides, our goal is to compare the modeled AGB from PALSAR-2 with AGB modeled from UAV. Therefore, we did not consider taking a larger plot area than 500 m^2. As a consequence, we are unsure whether increasing the plot area size would make any difference in AGB–backscatter relationship in our study.

4.2.2 Plot Backscatter Extraction

As mentioned earlier, the backscatter coefficients per plot were extracted by setting a 3x3 pixel window (see *Figure 11*). Thus, for each plot, backscatter coefficients of 9 pixels were collected, and the average was calculated to use in AGB estimation models. In this process, the 3x3 pixel square is adjusted on the plot and the center of the pixel shifts. *Figure 33* showed the shift in plot center due to the establishment of the backscatter extraction window.

The size of the pixel window depended on the field plot area and the final pixel size of the backscatter image after processing and geocoding. In our case, the final image pixel resolution was 7x7 m. A 3x3 pixel window represents the plot with a 25.24 m diameter and reduces the error due to smoothing the average backscatter values. A pixel window of 5x5 might increase the chance of taking backscatter information of trees on the plot boundary. However, it also increases the chance of taking unmeasured trees and smoothening the average backscatter plot (Hamdan et al., 2014; Nesha, 2019). The plots on the edges of the forest or plots near gaps might have been affected due to a larger pixel window. There are trees with significantly large biomass representing bright pixels on the backscatter image on the edges of the forests, while the fields and gaps nearby are without AGB representing dark pixels. Setting a 5x5 window increases the possibility of taking those dark pixels in averaging backscatter values and generating a lower average backscatter value for higher AGB.

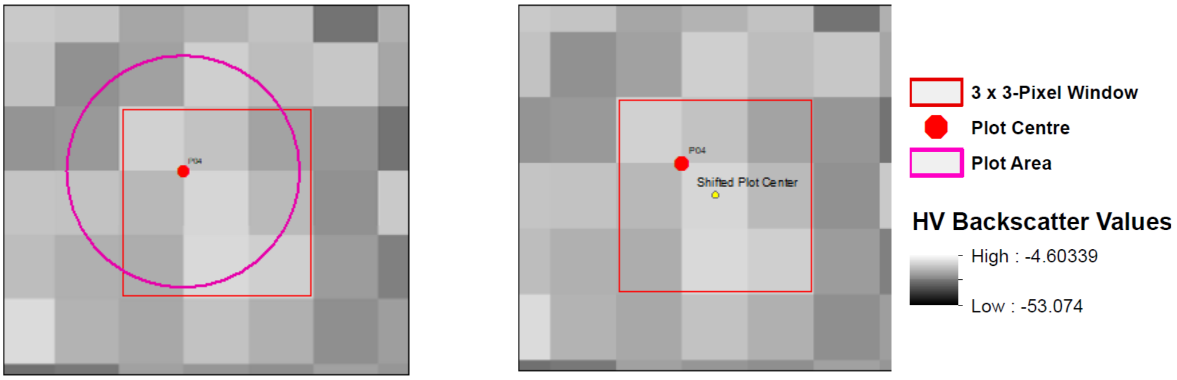

(a) The original position of the plot center at the intersection of the four pixels (red point).

(b) Shifted position of the plot center (yellow point) and the establishment of 3 by 3 pixels window.

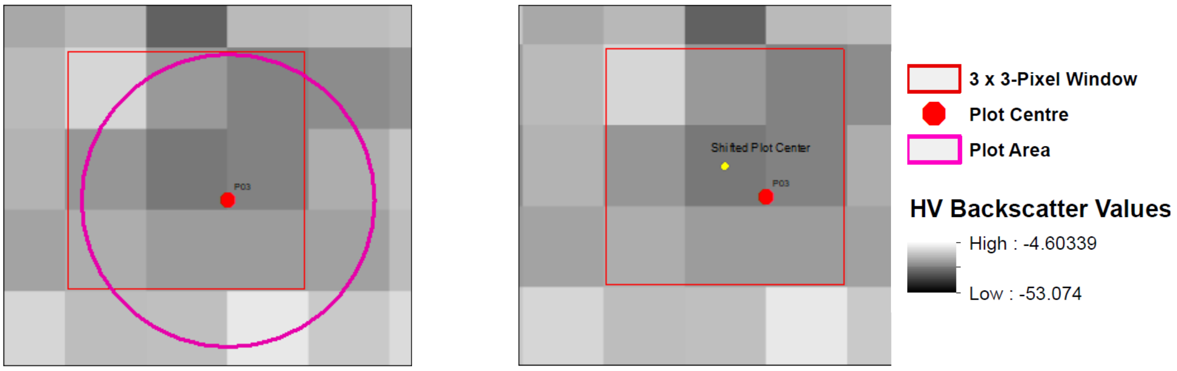

(c) The original position of the plot center at the edge of two pixels (red point).

(d) Shifted position of the plot center (yellow point) and the establishment of 3 by 3 pixels window.

Figure 33: Shifting of plot center to establish 3x3 pixel window for backscatter extraction. (As adopted from Nesha, 2019)

4.2.3 AGB Saturation Point

In the scatterplots of the linear regression between backscatter coefficients and AGB, it was observed that there is inconsistent variance in AGB with respect to the backscatter coefficients (see *Figure 22, Figure 23,* and *Figure 24*). The inconsistency in the AGB-backscatter relationship was observed to be higher in HH backscatter rather than HV backscatter relationships. Many studies have found that the backscatter values saturate at a certain AGB value (Imhoff, 1995; Joshi et al., 2015; Masolele et al., 2018; Nesha et al., 2020; Watanabe et al., 2006). We have found that for HV backscatter and $\log_{10}$(AGB), biomass saturates at 314.4 tons/ha (Figure 29). Our saturation point was higher compared to the saturation point found by (Imhoff, 1995; Masolele et al., 2018; Nesha et al., 2020). Biomass saturation is explained as the influence of soil moisture and canopy structure on the backscatter coefficients (Hamdan et al., 2015; Imhoff, 1995). Ji et al. (2020) studied the dependency of PALSAR-2 HV backscatter on the forest structure of a temperate forest. Their analysis results revealed that the HV backscatter coefficients are sensitive to the stand's mean canopy density and height. Yu & Saatchi (2016) also argued that the surface volume and soil moisture could significantly influence the backscatter in a temperate forest. In our model, the study area plots were mostly dense with a canopy density of 60% and higher; therefore, the saturation point was observed higher than in other studies (Golshani et al., 2019; Imhoff, 1995; Stelmaszczuk-Górska et al., 2018).

4.2.4 Accuracy of AGB estimation from HV backscatter

The biomass estimated from the HV backscatter represented a positive correlation with biometric AGB. However, the scatterplot of biometric AGB and SAR estimated AGB plotted against a 1-1 line showed a bias in SAR estimated AGB (*Figure 27*). We also depicted that the HV backscatter model overestimated plot AGB when the model function is applied on the plots of the validation dataset. The distribution of field-measured AGB could explain the overestimation of AGB. The distribution of our field measured data in Figure 14 showed that the plot AGB is skewed to the left on the density curve. That indicates a low number of plot samples with higher AGB. We have only four sample plots that represented the 400–640 tons/ha AGB range. Having less representative plots of higher AGB could have influenced the overestimation of AGB by PALSAR-2 backscatter, as there was insufficient data to reduce the influence of high AGB plots.

4.3 Comparing the plot based AGB estimations from UAV and PALSAR-2

We expected the underestimation of the UAV model on plot AGB estimation based on our field measured data. However, the overestimation in some plots is very high that indicates significant weakness of the UAV model. *Figure 31* depicted that plot 5 and plot 51 was underestimated at a higher rate. Plot 5 had a total of 18 species, of which 12 were conifers: Spruce and Douglas-fir. Those conifers were dominated by the broadleaves and obscured from the UAV Orthomosaic. Plot 51 was a broadleaf stand dominated by *Fraxinus spp.* UAV-based AGB estimation results on plot 51 depicted that underestimating *Fraxinus spp.* AGB led to underestimating overall plot AGB. Plot 67, dominated by Beech and Oak, depicted 130% overestimation. The overestimation of plot AGB was influenced by inaccurate CPA delineation that was already discussed earlier in section 4.1.2.

The PALSAR-2 model also overestimated and underestimated AGB, even though the variation in AGB overestimation or underestimation is low. Moreover, it is worth mentioning that we have backscatter saturates at 314.4 tons/ha AGB. Therefore, plots with 314.4 tons/ha or above AGB would be assessed inaccurately.

To compare plot AGB estimation from UAV RGB and PALSAR-2 images, the models should have comparable accuracy. In terms of the accuracy on area basis AGB estimation, UAV lacks far behind PALSAR-2. The output of this study leads to a conclusion that PALSAR-2 images are much better than UAV RGB images in an area-based AGB estimation. However, this should not necessarily be the final verdict. Based on our analysis, we have observed that UAV RGB images can accurately model individual tree AGB, and underestimation occurred when taller trees conceal smaller trees in high canopy density stand. An L-band SAR image is better than UAV RGB images for a forest with intermingling tree crowns. However, in an open or non-intermingling crown stand, UAV can estimate AGB accurately, which is also evident from our coniferous plots. Moreover, forest soil moisture could influence the backscatter coefficients in an open forest and introduce errors in AGB modeling from L-band SAR images. A comparative study on the open forest or forest stands with non-intermingling crowns could clarify whether SAR images would perform better than UAV RGB images on such forest stands.

4.4 Limitations and Uncertainties of the Study

As this study aimed to compare AGB estimated from UAV and PALSAR-2 images, we used the methods from both sensors that are standard and commonly used for AGB estimation. We used generalized models rather than using complex methods and multiple models for AGB estimation from both sensors. Using complex methods and models would require more analysis efforts. However, these simplifications of models in the analysis seemed to affect the AGB estimation accuracy that we have discussed above. Moreover, the study also had some uncertainties in the field data and image processing that have not been discussed yet. In the following, we have discussed the uncertainties associated with field-measured data, AGB calculation from allometric equations, and image processing.

4.4.1 Uncertainties in Field-Measured data

We have used UAV RGB Orthomosaic loaded in a mobile application named Avenza Maps to record plot center location in the field data collection. UAV Orthomosaic that we used was processed in medium quality. We use caution while identifying the plot center location on the Orthomosaic by using distance and bearing from identifiable permanent objects or landmarks such as buildings, constructions, edge of the field, intersect of roads, or unique trees. Moreover, the Avenza Maps also relied on the mobile internet connection to give us a relatively accurate location. We were able to identify the plot center location precisely by visually interpreting the Orthomosaic and reestablishing the plot center on an orthorectified Orthomosaic processed with GCPs. Plot center location identification was comparatively easy when a tree is one the center of the plot. However, despite taking cautions, a few plots were difficult to identify the precise plot center location, mainly for plots with no tree on the center. In these plots, inaccurate plot center location resulted in inaccurate calculation of individual tree geolocation. We were able to fix some of these plot locations by cross-checking with the bearing and distance of individual trees, and some plots required revisit on the field.

To locate individual trees in a plot, we have used the distance and bearing from the plot center. We measured the distance and bearing of the tree trunk from the plot center. However, in reality, it seemed that many trees were leaning from the trunk location, or the canopy did not have the trunk in center. This leaning of trees caused some difficulties in identifying trees. Also, the locations of trees that cannot be seen from UAV images were not possible to verify. The location of these trees was not crucial as they are not visible in the UAV image. Use Shunnto Compass to measure the bearing of the tree trunk from the plot center. Inaccurate bearing reading could lead to inaccurate calculation of tree geolocation.

We use laser range finders to measure the height of trees. However, measuring tree heights was challenging on the field where the top of the tree was not visible, especially in dense forests. Therefore, multiple measurements were taken from different locations from which tree top can be seen to ensure the accuracy in tree height measurement. However, interference of the lower canopy could have caused inaccuracies in the measurement of tree heights.

4.4.2 Uncertainties in AGB Calculation using Allometry and Converting into Plot AGB

As we discussed earlier, the allometric equations to calculate AGB was selected to represent the age and DBH range of the trees. The allometric equations were also selected from areas of the same biome as the Haagse Bos. Allometric equations were not completely satisfactory for the DBH range of our study area. However, it seemed that these are the best we could use to estimate AGB unless we divide the trees into multiple DBH ranges and use multiple equations for each species based on the DBH range. It is worth mentioning that allometric equations have inherent uncertainties as they are the models developed base on sample data. Moreover, we used species-specific allometric equations to calculate AGB. It is sometimes very challenging to distinguish species from UAV RGB Orthomosaic. For example, distinguishing Spruce and Douglas-fir or Beech and Oak was very challenging from the UAV RGB Orthomosaic of our study area. If a tree was misidentified as a different species, the allometric equation applied for that tree would represent incorrect AGB. However, we managed to reduce the uncertainty of species misidentification by using the plot photos taken during the fieldwork.

Moreover, we have estimated the AGB of individual trees of a plot and finally converted the AGB into tons/ha unit based on the plot AGB. The conversion of plot AGB into a unit higher than the plot area propagates some errors (Chave et al., 2004). The errors of tree measurement, error associated with allometric equations, error in sampling and representativeness of the large forest area by a small plot could have accumulated on the uncertainties in AGB calculation of the study area.

4.4.3 Uncertainties associated with UAV Images

We have discussed most of the uncertainties with UAV images in sections 4.2.1 and 4.2.2. The UAV images were collected on different dates for different flight blocks. Even though a similar weather condition was followed, the amount of sunlight and cloud was not uniform on all days. Besides, images collected from different flight blocks did not have the same ground sampling distance (*Table 8*). The quality of the point cloud was affected by the ground sampling distance and the amount of sunlight or clouds in the sky. We also noticed that some of the forest areas in Orthomosaics were blurred. The blur was created by the shaking of the camera/UAV on flight primarily due to wind. Moreover, the GCPs used in the flight blocks were not uniform in all blocks. For some flight blocks, it was possible to attain higher geolocation accuracy where we had to settle with comparatively low geolocation accuracy in the rest of them. Since we omitted plots where the images were blurred, and the CPA was digitized manually, these uncertainties had minimal effect on the study outcomes.

4.4.4 Uncertainties associated with PALSAR-2 Image

The ALOS-2 PALSAR-2 image scanned the study area in May, while the UAV images and field data collection were conducted in September and October. This could introduce a temporal inconsistency between the PALSAR-2 image, UAV images and field data as the deciduous trees of the forest change a lot from May (Spring) to September (Fall).

The geocoding of the PALSAR-2 image was done prior to plot backscatter coefficient extraction and used in the analysis. The geocoding and georeferencing of the PASLAR-2 image could introduce some errors due to the use of a 30 m resolution SRTM digital elevation model. The PALSAR-2 image obtained has a pixel spacing of 4.29 m. After terrain correction, the resolution of HH and HV backscatter images was reduced to 7 m due to the use of 30 m resolution DEM.

In addition, the backscatter images had speckle noise that was reduced by applying a 3x3 Lee filter. Speckle filtering also smoothened the backscatter values by taking neighboring pixels' backscatter values into account. As a consequence, the backscatter values used in modeling AGB from the PALSAR-2 image integrate the uncertainties associated with noise filtering in addition to the uncertainties associated with geocoding and georeferencing of the images.

4.5 Implications of the Study for Future Use

The study compared the AGB estimated from UAV and L-band SAR of a temperate forest. The outcome of this study can be used for the implementation of Carbon Accounting in the Netherlands, the EU Forest Strategy, or the REDD+ MRV. This study indicates that UAV could be effective for small study areas; however, to measure a vast area, the use of SAR could be a low-cost method. Further implications of the study are explained below.

The UAV model depicted a high relationship between the CPA and DBH, thus leading to an accurate AGB estimation of the trees. However, the study also depicted that a large portion of forest biomass is not assessed by using UAV RGB images. The model's outcome depends on various factors during the fieldwork for UAV Image acquisition, such as flight planning, time of the day or sun angle, cloud condition, and wind. Moreover, the UAV images processed are required to be of high quality. Despite having a very high-resolution Orthomosaic, the UAV image could be useless unless the quality is maintained. For example, we had images with very accurate geolocation due to the GCPs, yet the blur in some parts of the Orthomosaic made those forests incompatible for assessment. It is worth mentioning that the processing of UAV images to acquire an orthorectified mosaic is quite burdensome and requires the understanding of photogrammetry; thus, replication of the process is not easy and fast. Considering the efforts it takes to acquire a good quality orthophoto, the use of UAV RGB for a large area would be highly challenging.

Moreover, the method that we used to estimate required manual digitization of trees in each plot. In reality, it is time-consuming and impractical if we want to map the whole forest. Therefore, automatic segmentation approaches are taken in that case. However, it will be challenging to identify tree types if automatic segmentation is used, especially for a mixed forest like the study area. Thus, the error due to segmentation will integrate, and errors in the CPA-DBH relationship model could increase.

On the other hand, the AGB estimation of the L-band SAR image depicted reasonably good accuracy, as we could explain 86% variation in biometric AGB based on our model. Furthermore, the implementation of the methods to develop the AGB–backscatter relationship was comparatively straightforward. Therefore, the development of the models can be replicated easily. However, we would recommend using more representative samples of higher AGB to improve the model. Considering the processing steps and ease of model establishment, we recommend SAR for a large area to estimate AGB.

5 CONCLUSION

This study compared the plot-based forest AGB estimated from UAV RGB and ALOS-2 PALSAR-2 images. First, we used UAV RGB images to build CPA-DBH relationship models to estimate DBH of trees grouped in conifers and broadleaves and obtained tree height from CHM. Then, we calculated AGB using species-specific allometric equations from the estimated DBH and height and transformed the individual tree AGBs into plot AGB. On the other hand, we have estimated AGB per plot from ALOS-2 PALSAR-2 image using the backscatter–AGB regression model for HH and HV polarizations. HV polarization backscatter depicted a higher accuracy than HH polarization backscatter to estimate AGB. Further, we investigated the accuracy of AGB modeled from both images. Several research questions were established to compare AGB estimated from UAV RGB and ALOS-2 PALSAR-2 images. The conclusions of our research based on the research questions are in the following:

RQ 1: What is the relationship between crown projection area from UAV and field measured DBH?

Crown projection area of trees has been digitized on-screen from the UAV Orthomosaic. By applying different regression functions, it was found that the power regression function explained the CPA-DBH relationship to estimate DBH for broadleaves ($R^2 = 0.89$, RMSE = 4.28 cm), and the binomial regression function explained the CPA-DBH relationship better in conifers ($R^2 = 0.92$, RMSE = 2.44 cm).

RQ 2: What is the modeled plot AGB from UAV RGB images?

The plot AGB was obtained by summing up the individual tree AGBs per plot that was calculated from the DBH and height estimated from the UAV images. The AGB of 57 plots modeled by the UAV RGB images ranged from 84.04 tons/ha to 470.15 tons/ha, with an average of 227.83 tons/ha.

RQ 3: What is the relationship between ALOS-2 PALSAR-2 backscatter and field measured AGB?

The relationship between -2 HH and HV polarization PALSAR-2 backscatter coefficients with AGB and $\log_{10}$(AGB) was modeled using linear regression functions. This study found that the regression between HV polarization backscatter and $\log_{10}$(AGB) has the highest relationship at an R^2 of 0.84 and RMSE = 37.83 tons/ha. The linear regression between HV backscatter and AGB also depicted a higher accuracy ($R^2 = 0.74$, RMSE = 47.39). However, HH backscatter with AGB ($R^2 = 0.43$) and with $\log_{10}$(AGB) at $R^2 = 0.47$ depicted poor relationships. The relationship between HV backscatter and $\log_{10}$(AGB) was used to model AGB.

RQ 4: What is the saturation point of AGB estimation in relation to ALOS-2 PALSAR-2 backscatter coefficients?

The study found that PALSAR-2 HV backscatter coefficients saturate to estimate AGB at 314.4 tons/ha. The saturation point indicates that the HV backscatter coefficients of the PALSAR-2 image have limitations in estimating AGB beyond 314.4 tons/ha.

RQ 5: What is the modeled plot AGB from ALOS-2 PALSAR-2 image?

HV backscatter and $\log_{10}$(AGB) relationship model was developed at R^2 of 0.85 and RMSE = 40.9 tons/ha. The model estimated plot AGB with a mean AGB of 205 tons/ha for 83 plots, and the plot AGB ranged from 79.77 tons/ha to 453.37 tons/ha.

RQ 6: What is the accuracy of AGB estimation from UAV?

The AGB modeled from UAV images was validated. Validation results depicted that modeled AGB of individual trees can explain 81% of the variability at an RMSE of 304.2 kg. On plots, the overall accuracy of UAV images was poor at R^2 of 0.35. These findings implied that UAV lacks in assessing plot AGB accurately.

RQ 7: What is the accuracy of AGB estimation from ALOS-2 PALSAR-2?

The model validation results for the estimated AGB for HV backscatter and $\log_{10}$(AGB) model depicted that the HV backscatter coefficients could explain 86% of field AGB at an RMSE of 26.63 tons/ha. However, the results also depicted a bias in the relationship model that overestimated AGB in some plots.

RQ 8: Is there a significant difference between estimated AGBs from backscatter images of ALOS-2 PALSAR-2 and UAV RGB images?

A one-way ANOVA test among the AGB estimated from UAV, PALSAR-2 and biometric data were performed to assess any differences in the AGB estimation. The ANOVA test results depicted that there was statistically no significant difference in mean AGB from the biometric data, AGB estimated from UAV images, and AGB estimated from PALSAR-2 image ($F(2,144) = 0.02$, $p = 0.99$). However, further analysis revealed significant overestimation by UAV images, especially on broadleaves and mixed forest stand, contributing to a higher mean AGB.

RQ 9: What is the difference in the accuracy of estimated AGB from UAV and ALOS-2 PALSAR-2 on coniferous, broadleaf, and mixed forest stand?

AGB modeled from UAV RGB and ALOS-2 PALSAR-2 images depicted overall higher accuracy on conifers than broadleaves and mixed forest stand. Even though UAV depicted poor accuracy in modeling plot AGB, the AGB estimation on coniferous plots depicted a comparatively better relationship at $R^2 = 0.52$ than broadleaves ($R^2 = 0.18$) and mixed ($R^2 = 0.02$). AGB modeled from the PALSAR-2 image depicted the highest correlation in conifers ($R^2 = 0.90$) compared to broadleaves ($R^2 = 0.82$) and mixed ($R^2 = 0.81$) forest stands.

Before reaching a final verdict, it should be noted that AGB estimation from UAV RGB images was an individual tree-based assessment, where from SAR images, AGB estimation was on the area basis. It was evident from the results that UAV RGB images could estimate individual tree AGB accurately; however, it lacked behind in estimation on the plot basis due to the intermingling crowns and obscured crowns by taller trees. PALSAR-2 images, on the other hand, performed better on area-based AGB estimation despite having an AGB saturation by the backscatter coefficients. Therefore, it can be concluded that for a temperate forest with intermingling crowns and a dense canopy, the L-band SAR image could be a better approach to estimate area-based AGB over UAV RGB images.

REFERENCES

Abdollahnejad, A., Panagiotidis, D., & Surovỳ, P. (2018). Estimation and extrapolation of tree parameters using spectral correlation between UAV and Pléiades data. *Forests*, *9*(2). https://doi.org/10.3390/f9020085

Beaudoin, A., Le Toan, T., Goze, S., Nezry, E., Lopes, A., Mougin, E., Hsu, C. C., Han, H. C., Kong, J. A., & Shin, R. T. (1994). Retrieval of forest biomass from SAR data. *International Journal of Remote Sensing*, *15*(14), 2777–2796. https://doi.org/10.1080/01431169408954284

Berhe, T. H. (2018). *Towards a UAV based Standalone System for Estimating and mapping Aboveground Biomass/carbon Stock in Berkelah Tropical Fain Forest, Malaysia (M.Sc Thesis)* [University of Twente]. https://ezproxy.utwente.nl:2315/library/2018/msc/nrm/berhe.pdf

Boisvenue, C., Smiley, B. P., White, J. C., Kurz, W. A., & Wulder, M. A. (2016). Integration of Landsat time series and field plots for forest productivity estimates in decision support models. *Forest Ecology and Management*, *376*, 284–297. https://doi.org/10.1016/j.foreco.2016.06.022

Bonham, C. D. (2013). Measurements for terrestrial vegetation. In *John Wiley & Sons, Ltd* (2nd Editio). https://doi.org/1

Brovkina, O., Cienciala, E., Surový, P., & Janata, P. (2018). Unmanned aerial vehicles (UAV) for assessment of qualitative classification of Norway spruce in temperate forest stands. *Geo-Spatial Information Science*, *21*(1), 12–20. https://doi.org/10.1080/10095020.2017.1416994

Brown, S. (1997a). Estimating biomass and biomass change of tropical forests: a primer. In *FAO Forestry Paper* (Vol. 134, Issue August). http://www.fao.org/docrep/W4095E/W4095E00.htm

Brown, S. (1997b). Forests and climate change: role of forest lands as carbon sinks. *Biomass and Bioenergy*, *13*, 117–153.

Brown, Sandra. (2002). Measuring carbon in forests: Current status and future challenges. *Environmental Pollution*, *116*(3), 363–372. https://doi.org/10.1016/S0269-7491(01)00212-3

Bunce, R. G. H. (1968). Biomass and Production of Trees in a Mixed Deciduous Woodland: I. Girth and Height as Parameters for the Estimation of Tree Dry Weight. *The Journal of Ecology*, *56*(3), 759. https://doi.org/10.2307/2258105

Chave, J., Andalo, C., Brown, S., Cairns, M. A., Chambers, J. Q., Eamus, D., Fölster, H., Fromard, F., Higuchi, N., Kira, T., Lescure, J. P., Nelson, B. W., Ogawa, H., Puig, H., Riéra, B., & Yamakura, T. (2005). Tree allometry and improved estimation of carbon stocks and balance in tropical forests. *Oecologia*, *145*(1), 87–99. https://doi.org/10.1007/s00442-005-0100-x

Chave, Jerome, Condit, R., Aguilar, S., Hernandez, A., Lao, S., & Perez, R. (2004). Error propagation and sealing for tropical forest biomass estimates. *Philosophical Transactions of the Royal Society B: Biological Sciences*, *359*(1443), 409–420. https://doi.org/10.1098/rstb.2003.1425

Cienciala, E., Černý, M., Tatarinov, F., Apltauer, J., & Exnerová, Z. (2006). Biomass functions applicable to Scots pine. *Trees - Structure and Function*, *20*(4), 483–495. https://doi.org/10.1007/s00468-006-0064-4

Collins, J. N., Hutley, L. B., Williams, R. J., Boggs, G., Bell, D., & Bartolo, R. (2009). Estimating landscape-scale vegetation carbon stocks using airborne multi-frequency polarimetric synthetic aperture radar (SAR) in the savannahs of north Australia. *International Journal of Remote Sensing*, *30*(5), 1141–1159. https://doi.org/10.1080/01431160802448935

Cutler, M. E. J., Boyd, D. S., Foody, G. M., & Vetrivel, A. (2012). Estimating tropical forest biomass with a combination of SAR image texture and Landsat TM data: An assessment of predictions between regions. *ISPRS Journal of Photogrammetry and Remote Sensing*, *70*, 66–77. https://doi.org/10.1016/j.isprsjprs.2012.03.011

d'Oliveira, M. V. N., Broadbent, E. N., Oliveira, L. C., Almeida, D. R. A., Papa, D. A., Ferreira, M. E., Zambrano, A. M. A., Silva, C. A., Avino, F. S., Prata, G. A., Mello, R. A., Figueiredo, E. O., de Castro Jorge, L. A., Junior, L., Albuquerque, R. W., Brancalion, P. H. S., Wilkinson, B., & Oliveira-da-Costa, M. (2020). Aboveground biomass estimation in Amazonian tropical forests: A comparison of aircraft-and gatoreye UAV-borne LIDAR data in the Chico mendes extractive reserve in Acre, Brazil. *Remote Sensing*, *12*(11). https://doi.org/10.3390/rs12111754

Dandois, J. P., Olano, M., & Ellis, E. C. (2015). Optimal altitude, overlap, and weather conditions for computer vision uav estimates of forest structure. *Remote Sensing*, *7*(10), 13895–13920. https://doi.org/10.3390/rs71013895

Dash, J. P., Pearse, G. D., & Watt, M. S. (2018). UAV multispectral imagery can complement satellite data for monitoring forest health. *Remote Sensing*, *10*(8). https://doi.org/10.3390/rs10081216

de Gouvenain, R. C., & Silander, J. A. (2017). Temperate Forests. *Reference Module in Life Sciences*. https://doi.org/10.1016/b978-0-12-809633-8.02310-4

Djomo, A. N., & Chimi, C. D. (2017). Tree allometric equations for estimation of above, below and total biomass in a tropical moist forest: Case study with application to remote sensing. *Forest Ecology and Management*, *391*, 184–193. https://doi.org/10.1016/j.foreco.2017.02.022

Dobson, M. C., Ulaby, F. T., Le Toan, T., Beaudoin, A., Kasischke, E. S., & Christensen, N. (1992). Dependence of Radar Backscatter on Coniferous Forest Biomass. *IEEE Transactions on Geoscience and Remote Sensing*, *30*(2), 412–415. https://doi.org/10.1109/36.134090

Du, H., Zhou, G., Ge, H., Fan, W., Xu, X., Fan, W., & Shi, Y. (2012). Satellite-based carbon stock estimation for bamboo forest with a non-linear partial least square regression technique. *International Journal of Remote Sensing*, *33*(6), 1917–1933. https://doi.org/10.1080/01431161.2011.603379

Eineder, M., Hajnsek, I., Krieger, G., Moreira, A., & Papathanassiou, K. (2014). Tandem-L: satellite mission proposal for monitoring dynamic processes on the Earth's surface. In *German Aerospace Center (DLR) [online]* (2nd Esitio, Issue May). http://www.dlr.de/hr/en/desktopdefault.aspx/tabid-8113/14171_read-35837/

European Commission. (2020). *A European Green Deal*. European Commission - European Commission. https://ec.europa.eu/info/strategy/priorities-2019-2024/european-green-deal_en

European Environment Agency. (2019). *Climate change is one of the biggest challenges of our times*. https://www.eea.europa.eu/themes/climate/climate-change-is-one-of

FAO. (2020). Global Forest Resources Assessment 2020. In *Global Forest Resources Assessment 2020* (Vol. 163). https://doi.org/10.4060/ca8753en

FFPRI. (2012). Measurement, reporting and verification of forest carbon. In *REDD Plus Cook Book - How to Measure and Monitor Forest Carbon*. https://www.ffpri.affrc.go.jp/redd-rdc/en/reference/cookbook.html

Fu, L., Duan, G., Ye, Q., Meng, X., Luo, P., Sharma, R. P., Sun, H., Wang, G., & Liu, Q. (2020). Prediction of individual tree diameter using a nonlinear mixed-effects modeling approach and airborne LiDAR Data. *Remote Sensing*, *12*(7). https://doi.org/10.3390/rs12071066

Gaden, K. (2020). *Assessing Potential Of UAV Multispectral Imagery For Estimation Of AGB And Carbon Stock In Conifer Forest Over UAV RGB Imagery*. http://essay.utwente.nl/85200/1/gaden.pdf

Gibbs, H. K., Brown, S., Niles, J. O., & Foley, J. A. (2007). Monitoring and estimating tropical forest carbon stocks: Making REDD a reality. *Environmental Research Letters*, *2*(4). https://doi.org/10.1088/1748-9326/2/4/045023

GlobAllomeTree. (2021). *GlobAllomeTree - Assessing volume, biomass, and carbon stocks of trees and forests*. http://www.globallometree.org/

Gobakken, T., & Næsset, E. (2008). Assessing effects of laser point density, ground sampling intensity, and field sample plot size on biophysical stand properties derived from airborne laser scanner data. *Canadian Journal of Forest Research*, *38*(5), 1095–1109. https://doi.org/10.1139/X07-219

Golshani, P., Maghsoudi, Y., & Sohrabi, H. (2019). Relating ALOS-2 PALSAR-2 Parameters to Biomass and Structure of Temperate Broadleaf Hyrcanian Forests. *Journal of the Indian Society of Remote Sensing*, *47*(5), 749–761. https://doi.org/10.1007/s12524-019-00948-0

González-Jaramillo, V., Fries, A., & Bendix, J. (2019). AGB estimation in a tropical mountain forest (TMF) by means of RGB and multispectral images using an unmanned aerial vehicle (UAV). *Remote Sensing*, *11*(12). https://doi.org/10.3390/rs11121413

Government of the Netherlands. (2021). *Dutch vision on global climate action | Climate change | Government.nl*. https://www.government.nl/topics/climate-change/dutch-vision-on-global-climate-action

Grüner, E., Wachendorf, M., & Astor, T. (2020). The potential of UAV-borne spectral and textural information for predicting aboveground biomass and N fixation in legume-grass mixtures. *PLoS ONE*, *15*(6), 1–21. https://doi.org/10.1371/journal.pone.0234703

Grznárová, A., Mokroš, M., Surový, P., Slavík, M., Pondelík, M., & Mergani, J. (2019). The crown diameter estimation from fixed wing type of uav imagery. *International Archives of the Photogrammetry, Remote Sensing and Spatial Information Sciences - ISPRS Archives*, *42*(2/W13), 337–341. https://doi.org/10.5194/isprs-archives-XLII-2-W13-337-2019

Guerra-Hernández, J., González-Ferreiro, E., Sarmento, A., Silva, J., Nunes, A., Correia, A. C., Fontes, L., Tomé, M., & Díaz-Varela, R. (2016). Using high resolution UAV imagery to estimate tree variables in Pinus pinea plantation in Portugal. *Forest Systems*, *25*(2). https://doi.org/10.5424/fs/2016252-08895

Hack, J. T. T., & Goodlett, J. C. (1960). Geomorphology and forest ecology of a mountain region in the central Appalachians. In *USGS Professional Paper* (Vol. 347, p. 66). https://pubs.er.usgs.gov/publication/pp347%0Ainternal-pdf://228.60.152.3/report-2.pdf

Hamdan, O., Khali Aziz, H., & Mohd Hasmadi, I. (2014). L-band ALOS PALSAR for biomass estimation of Matang Mangroves, Malaysia. *Remote Sensing of Environment*, *155*, 69–78. https://doi.org/10.1016/j.rse.2014.04.029

Hamdan, O., Mohd Hasmadi, I., Khali Aziz, H., Norizah, K., & Helmi Zulhaidi, M. S. (2015). L-band saturation level for aboveground biomass of dipterocarp forests in peninsular Malaysia. *Journal of Tropical Forest Science*, *27*(3), 388–399.

Hirata, Y., Tabuchi, R., Patanaponpaiboon, P., Poungparn, S., Yoneda, R., & Fujioka, Y. (2014). Estimation of aboveground biomass in mangrove forests using high-resolution satellite data. *Journal of Forest Research*, *19*(1), 34–41. https://doi.org/10.1007/s10310-013-0402-5

Hojo, A., Takagi, K., Avtar, R., Tadono, T., & Nakamura, F. (2020). Synthesis of l-band sar and forest heights derived from TanDEM-X DEM and 3 digital terrain models for Biomass Mapping. *Remote Sensing*, *12*(3). https://doi.org/10.3390/rs12030349

Huang, X., Ziniti, B., Torbick, N., & Ducey, M. J. (2018). Assessment of forest above ground biomass estimation using multi-temporal C-band Sentinel-1 and Polarimetric L-band PALSAR-2 data. *Remote Sensing*, *10*(9). https://doi.org/10.3390/rs10091424

Hussin, Y. A., Reich, R. M., & Hoffer, R. M. (1991). Estimating slash pine biomass using radar backscatter. *IEEE Transactions on Geoscience and Remote Sensing*, *29*(3), 427–431. https://doi.org/10.1109/36.79433

Imhoff, M. L. (1995). Radar backscatter and biomass saturation: ramifications for global biomass inventory. *IEEE Transactions on Geoscience and Remote Sensing*, *33*(2), 511–518. https://doi.org/10.1109/36.377953

IPCC. (2014). Climate Change 2014 Mitigation of Climate Change. In *Climate Change 2014 Mitigation of*

Climate Change. https://doi.org/10.1017/cbo9781107415416

Ji, Y., Huang, J., Ju, Y., Guo, S., & Yue, C. (2020). Forest structure dependency analysis of L-band SAR backscatter. *PeerJ*, *8*. https://doi.org/10.7717/peerj.10055

Joshi, N. P., Mitchard, E. T. A., Schumacher, J., Johannsen, V. K., Saatchi, S., & Fensholt, R. (2015). L-Band SAR Backscatter Related to Forest Cover, Height and Aboveground Biomass at Multiple Spatial Scales across Denmark. *Remote Sensing*, *7*(4), 4442–4472. https://doi.org/10.3390/rs70404442

Jucker, T., Caspersen, J., Chave, J., Antin, C., Barbier, N., Bongers, F., Dalponte, M., van Ewijk, K. Y., Forrester, D. I., Haeni, M., Higgins, S. I., Holdaway, R. J., Iida, Y., Lorimer, C., Marshall, P. L., Momo, S., Moncrieff, G. R., Ploton, P., Poorter, L., … Coomes, D. A. (2017). Allometric equations for integrating remote sensing imagery into forest monitoring programmes. In *Global Change Biology* (Vol. 23, Issue 1, pp. 177–190). https://doi.org/10.1111/gcb.13388

Kaasalainen, S., Holopainen, M., Karjalainen, M., Vastaranta, M., Kankare, V., Karila, K., & Osmanoglu, B. (2015). Combining lidar and synthetic aperture radar data to estimate forest biomass: Status and prospects. *Forests*, *6*(1), 252–270. https://doi.org/10.3390/f6010252

Klimaatakkoord. (2019). *National Climate Agreement - The Netherlands - Publicatie - Klimaatakkoord*. https://www.klimaatakkoord.nl/documenten/publicaties/2019/06/28/national-climate-agreement-the-netherlands%0Ahttps://www.klimaatakkoord.nl/documenten/publicaties/2019/06/28/national-climate-agreement-the-netherlands%0Ainternal-pdf://0.0.2.78/national-clim

Komárek, J. (2020). The perspective of unmanned aerial systems in forest management: Do we really need such details? *Applied Vegetation Science*, *October 2019*, 14–17. https://doi.org/10.1111/avsc.12503

Lee, H., Wang, J., & Leblon, B. (2020). Using linear regression, random forests, and support vector machine with unmanned aerial vehicle multispectral images to predict canopy nitrogen weight in corn. *Remote Sensing*, *12*(13). https://doi.org/10.3390/rs12132071

Liao, Z., He, B., & Quan, X. (2020). Potential of texture from SAR tomographic images for forest aboveground biomass estimation. *International Journal of Applied Earth Observation and Geoinformation*, *88*, 102049. https://doi.org/10.1016/j.jag.2020.102049

Lin, J., Wang, M., Ma, M., & Lin, Y. (2018). Aboveground tree biomass estimation of sparse subalpine coniferous forest with UAV oblique photography. *Remote Sensing*, *10*(11). https://doi.org/10.3390/rs10111849

Lu, D. (2006). The potential and challenge of remote sensing-based biomass estimation. *International Journal of Remote Sensing*, *27*(7), 1297–1328. https://doi.org/10.1080/01431160500486732

Lucas, R. M., Mitchell, A. L., & Armston, J. (2015). Measurement of forest above-ground biomass using active and passive remote sensing at large (Subnational to global) scales. *Current Forestry Reports*, *1*(3), 162–177. https://doi.org/10.1007/s40725-015-0021-9

Manakos, I., & Lavender, S. (2014). Remote sensing in support of the geo-information in Europe. In *Remote Sensing and Digital Image Processing* (Vol. 18). https://doi.org/10.1007/978-94-007-7969-3_1

Masolele, R. N., Hussin, Y. A., & Kloosterman, D. E. H. (2018). ALOS-2 PALSAR-2 L-band cross-polarized radar data analysis for modelling above-ground biomass/carbon stock and carbon sequestration of tropical rainforest, Berkelah, Malaysia [University of Twente, The Netherlands]. In *Semantic Scholar* (Issue February). https://library.itc.utwente.nl/papers_2018/msc/nrm/masolele.pdf

Mitchard, E. T. A., Saatchi, S. S., Woodhouse, I. H., Nangendo, G., Ribeiro, N. S., Williams, M., Ryan, C. M., Lewis, S. L., Feldpausch, T. R., & Meir, P. (2009). Using satellite radar backscatter to predict above-ground woody biomass: A consistent relationship across four different African landscapes. *Geophysical Research Letters*, *36*(23). https://doi.org/10.1029/2009GL040692

Mlambo, R., Woodhouse, I. H., Gerard, F., & Anderson, K. (2017a). Structure from motion (SfM) photogrammetry with drone data: A low cost method for monitoring greenhouse gas emissions from forests in developing countries. *Forests*, *8*(3). https://doi.org/10.3390/f8030068

Mlambo, R., Woodhouse, I. H., Gerard, F., & Anderson, K. (2017b). Structure from motion (SfM) photogrammetry with drone data: A low cost method for monitoring greenhouse gas emissions from forests in developing countries. *Forests*, *8*(3), 68. https://doi.org/10.3390/f8030068

Morrison, I. K. (1991). Organic matter and mineral distribution in an old-growth Acer saccharum forest near the northern limit of its range . *Canadian Journal of Forest Research*, *21*(7), 1153–1153. https://doi.org/10.1139/x91-162

Mtui, Y. P., Erdbrügger, J., Hussin, Y. A., Van Leeuwen, L. M., Kloosterman, H., & Ismail, M. H. (2017). Comparison of forest tree parameters extracted from uav optical and tls data in both tropical rain and temperate forests. *38th Asian Conference on Remote Sensing - Space Applications: Touching Human Lives, ACRS 2017*, *2017-Octob*.

Næsset, E., McRoberts, R. E., Pekkarinen, A., Saatchi, S., Santoro, M., Trier, Ø. D., Zahabu, E., & Gobakken, T. (2020). Use of local and global maps of forest canopy height and aboveground biomass to enhance local estimates of biomass in miombo woodlands in Tanzania. *International Journal of Applied Earth Observation and Geoinformation*, *89*, 102109. https://doi.org/10.1016/j.jag.2020.102109

Natuurmonumenten. (2021). *Nature reserve Haagse Bos*. https://www.natuurmonumenten.nl/natuurgebieden/haagse-bos#r=1

Nesha, M. K. (2019). *Estimating and mapping aboveground biomass/carbon stock using ALOS-2 PALSAR-2 in the mangrove forest in East Kalimantan, Indonesia* (Issue February) [University of Twente]. https://library.itc.utwente.nl/papers_2019/msc/nrm/nesha.pdf

Nesha, M. K., Hussin, Y. A., van Leeuwen, L. M., & Sulistioadi, Y. B. (2020). Modeling and mapping aboveground biomass of the restored mangroves using ALOS-2 PALSAR-2 in East Kalimantan, Indonesia. *International Journal of Applied Earth Observation and Geoinformation*, *91*, 102158. https://doi.org/10.1016/j.jag.2020.102158

Nguyen, T. N. (2010). Estimation and mapping of above ground biomass for the assessment and mapping of carbon stocks in tropical forest using SAR data : a case study in Afram headwaters forest, Ghana. In *University of Twente Faculty of Geo-Information and Earth Observation (ITC)*. https://doi.org/Shelfmark 2010 THANH NGA

Ningthoujam, R. K., Balzter, H., Tansey, K., Feldpausch, T. R., Mitchard, E. T. A., Wani, A. A., & Joshi, P. K. (2017). Relationships of S-band radar backscatter and forest aboveground biomass in different forest types. *Remote Sensing*, *9*(11). https://doi.org/10.3390/rs9111116

Novák, J., Slodičák, M., & Dušek, D. (2011). Aboveground biomass of substitute tree species stand with respect to thinning - European larch (Larix decidua Mill.). *Journal of Forest Science*, *57*(1), 8–15. https://doi.org/10.17221/24/2010-jfs

Nuthammachot, N., Askar, A., Stratoulias, D., & Wicaksono, P. (2020). Combined use of Sentinel-1 and Sentinel-2 data for improving above-ground biomass estimation. *Geocarto International*, *0*(0), 1–11. https://doi.org/10.1080/10106049.2020.1726507

Odipo, V. O., Nickless, A., Berger, C., Baade, J., Urbazaev, M., Walther, C., & Schmullius, C. (2016). Assessment of aboveground woody biomass dynamics using terrestrial laser scanner and L-band ALOS PALSAR data in South African Savanna. *Forests*, *7*(12). https://doi.org/10.3390/f7120294

Ota, T., Ogawa, M., Shimizu, K., Kajisa, T., Mizoue, N., Yoshida, S., Takao, G., Hirata, Y., Furuya, N., Sano, T., Sokh, H., Ma, V., Ito, E., Toriyama, J., Monda, Y., Saito, H., Kiyono, Y., Chann, S., & Ket, N. (2015). Aboveground biomass estimation using structure from motion approach with aerial photographs in a seasonal tropical forest. *Forests*, *6*(11), 3882–3898.

https://doi.org/10.3390/f6113882

Parker, W. V. (2013). *Discover the Benefits of Radar Imaging*. http://www.pacificcollege.edu/acupuncture-massage-news/press-releases/668-discover-the-benefits-of-electro-acupuncture.html

Perkins, K. M., Munguia, N., Moure-Eraso, R., Delakowitz, B., Giannetti, B. F., Liu, G., Nurunnabi, M., Will, M., & Velazquez, L. (2018). International perspectives on the pedagogy of climate change. *Journal of Cleaner Production*, *200*, 1043–1052. https://doi.org/10.1016/j.jclepro.2018.07.296

Poley, L. G., & McDermid, G. J. (2020). A systematic review of the factors influencing the estimation of vegetation aboveground biomass using unmanned aerial systems. *Remote Sensing*, *12*(7). https://doi.org/10.3390/rs12071052

Rahman, M. Z. A., Bakar, M. A. A., Razak, K. A., Rasib, A. W., Kanniah, K. D., Kadir, W. H. W., Omar, H., Faidi, A., Kassim, A. R., & Latif, Z. A. (2017). Non-destructive, laser-based individual tree aboveground biomass estimation in a tropical rainforest. *Forests*, *8*(3). https://doi.org/10.3390/f8030086

Rizvi, A. R., Baig, S., Barrow, E., & Kumar, C. (2015). *Synergies between Climate Mitigation and Adaptation in Forest Landscape Restoration*. 75.

Rodríguez-Veiga, P., Quegan, S., Carreiras, J., Persson, H. J., Fransson, J. E. S., Hoscilo, A., Ziółkowski, D., Stereńczak, K., Lohberger, S., Stängel, M., Berninger, A., Siegert, F., Avitabile, V., Herold, M., Mermoz, S., Bouvet, A., Le Toan, T., Carvalhais, N., Santoro, M., … Balzter, H. (2019). Forest biomass retrieval approaches from earth observation in different biomes. *International Journal of Applied Earth Observation and Geoinformation*, *77*, 53–68. https://doi.org/10.1016/j.jag.2018.12.008

Ruiz, L. A., Hermosilla, T., Mauro, F., & Godino, M. (2014). Analysis of the influence of plot size and LiDAR density on forest structure attribute estimates. *Forests*, *5*(5), 936–951. https://doi.org/10.3390/f5050936

Sandberg, G., Ulander, L. M. H., Fransson, J. E. S., Holmgren, J., & Le Toan, T. (2011). L- and P-band backscatter intensity for biomass retrieval in hemiboreal forest. *Remote Sensing of Environment*, *115*(11), 2874–2886. https://doi.org/10.1016/j.rse.2010.03.018

Santi, E., Chiesi, M., Fontanelli, G., Lapini, A., Paloscia, S., Pettinato, S., Ramat, G., & Santurri, L. (2021). Mapping woody volume of mediterranean forests by using sar and machine learning: A case study in central Italy. *Remote Sensing*, *13*(4), 1–19. https://doi.org/10.3390/rs13040809

Santi, E., Paloscia, S., Pettinato, S., Cuozzo, G., Padovano, A., Notarnicola, C., & Albinet, C. (2020). Machine-learning applications for the retrieval of forest biomass from airborne P-band SAR data. *Remote Sensing*, *12*(5). https://doi.org/10.3390/rs12050804

Schlund, M., Scipal, K., & Quegan, S. (2018). Assessment of a Power Law Relationship between P-Band SAR Backscatter and Aboveground Biomass and Its Implications for BIOMASS Mission Performance. *IEEE Journal of Selected Topics in Applied Earth Observations and Remote Sensing*, *11*(10), 3538–3547. https://doi.org/10.1109/JSTARS.2018.2866868

Shapiro, S. S., & Wilk, M. B. (1965). An analysis of variance test for normality (complete samples). *Biometrika*, *52*(3–4), 591–611. https://doi.org/10.1093/biomet/52.3-4.591

Shashkov, M., Ivanova, N., Shanin, V., & Grabarnik, P. (2019). *Ground Surveys Versus UAV Photography: The Comparison of Two Tree Crown Mapping Techniques*. 48–56. https://doi.org/10.1007/978-3-030-11720-7_8

Shen, X., Cao, L., Yang, B., Xu, Z., & Wang, G. (2019). Estimation of forest structural attributes using spectral indices and point clouds from UAS-based multispectral and RGB imageries. *Remote Sensing*, *11*(7). https://doi.org/10.3390/rs11070800

Shimano, K. (1997). Analysis of the relationship between DBH and crown projection area using a new model. *Journal of Forest Research*, *2*(4), 237–242. https://doi.org/10.1007/BF02348322

Shinozaki, K., Yoda, K., Hozumi, K., & Kira, T. (1964). A Quantitative Analysis of Plant Form-the Pipe Model Theory : Ii. Further Evidence of the Theory and Its Application in Forest Ecology. *A Quantitative Analysis of Plant Form-the Pipe Model Theory : Ii. Further Evidence of the Theory and Its Application in Forest Ecology*, *14*(4), 133–139. https://doi.org/10.18960/seitai.14.4_133

Smith, P., Bustamante, M., Ahammad, H., Clark, H., Dong, H., Elsiddig, E. A., Haberl, H., Harper, R., House, J., Jafari, M., Masera, O., Mbow, C., Ravindranath, N. H., Rice, C. W., Abad, C. R., Romanovskaya, A., Sperling, F., & Tubiello, F. (2015). Agriculture, Forestry and Other Land Use (AFOLU). In *Climate Change 2014 Mitigation of Climate Change*. https://doi.org/10.1017/cbo9781107415416.017

Stelmaszczuk-Górska, M. A., Urbazaev, M., Schmullius, C., & Thiel, C. (2018). Estimation of above-ground biomass over boreal forests in Siberia using updated in Situ, ALOS-2 PALSAR-2, and RADARSAT-2 data. *Remote Sensing*, *10*(10). https://doi.org/10.3390/rs10101550

Stovall, A. E. L., Vorster, A. G., Anderson, R. S., Evangelista, P. H., & Shugart, H. H. (2017). Non-destructive aboveground biomass estimation of coniferous trees using terrestrial LiDAR. *Remote Sensing of Environment*, *200*, 31–42. https://doi.org/10.1016/j.rse.2017.08.013

Torres Rodriguez, A. (2020). *Effect of crown size and shape of different temperate tree species on modelling AGB and AGC using UAV images*. http://essay.utwente.nl/85243/

Tyrrell, M. L., Ross, J., & Kelty, M. (2012). Carbon dynamics in the temperate forest. In *Managing Forest Carbon in a Changing Climate* (pp. 77–107). https://doi.org/10.1007/978-94-007-2232-3_5

UNEP. (2018a). Advancing on REDD+ Module 1: National Forest Monitoring Systems for REDD+. In *REDD+ Academy Learning Journals* (Issue August). https://www.unredd.net/documents/global-programme-191/redd-academy-3509/redd-academy-learning-journals/english/17232-fundamentals-on-redd-module-1-climate-change-and-the-role-of-forests-1.html

UNEP. (2018b). Fundamentals on REDD+ Module 2: Understanding REDD+ and the UNFCCC. In *REDD+ Academy Learning Journals* (Issue December). https://www.unredd.net/documents/global-programme-191/redd-academy-3509/redd-academy-learning-journals/english/17233-fundamentals-on-redd-module-2-understanding-redd-and-the-unfccc-1.html

Urry, J. (2015). Climate Change and Society. In *Why the Social Sciences Matter*. https://doi.org/10.1057/9781137269928_4

Van Zyl, J. J. (1993). The Effect of Topography on Radar Scattering from Vegetated Areas. *IEEE Transactions on Geoscience and Remote Sensing*, *31*(1), 153–160. https://doi.org/10.1109/36.210456

Venus, J. C., & Causton, D. R. (1979). Plant growth analysis: The use of the Richards function as an alternative to polynomial exponentials. *Annals of Botany*, *43*(5), 623–632. https://doi.org/10.1093/oxfordjournals.aob.a085673

Watanabe, M., Shimada, M., Rosenqvist, A., Tadono, T., Matsuoka, M., Romshoo, S. A., Ohta, K., Furuta, R., Nakamura, K., & Moriyama, T. (2006). Forest structure dependency of the relation between L-band σ 0 and biophysical parameters. *IEEE Transactions on Geoscience and Remote Sensing*, *44*(11), 3154–3164. https://doi.org/10.1109/TGRS.2006.880632

Westoby, M. J., Brasington, J., Glasser, N. F., Hambrey, M. J., & Reynolds, J. M. (2012). "Structure-from-Motion" photogrammetry: A low-cost, effective tool for geoscience applications. *Geomorphology*, *179*, 300–314. https://doi.org/10.1016/j.geomorph.2012.08.021

White, J. (1981). The allometric interpretation of the self-thinning rule. *Journal of Theoretical Biology*, *89*(3), 475–500. https://doi.org/10.1016/0022-5193(81)90363-5

Workie, T. G. (2011). *Assessment of aboveground carbon stock in coniferous and broadleaf forests, using high spatial resolution satellite images*. 85. http://www.itc.nl/library/papers_2011/msc/gem/workie.pdf

Yang, Z., Liu, Q., Luo, P., Ye, Q., Duan, G., Sharma, R. P., Zhang, H., Wang, G., & Fu, L. (2020).

Prediction of individual tree diameter and height to crown base using nonlinear simultaneous regression and airborne LiDAR data. *Remote Sensing*, *12*(14). https://doi.org/10.3390/rs12142238

Yu, Y., & Saatchi, S. (2016). Sensitivity of L-band SAR backscatter to aboveground biomass of global forests. *Remote Sensing*, *8*(6). https://doi.org/10.3390/rs8060522

Yurtseven, H., Çoban, S., Akgül, M., & Akay, A. O. (2019). Individual tree measurements in a planted woodland with terrestrial laser scanner. *Turkish Journal of Agriculture and Forestry*, *43*(2), 192–208. https://doi.org/10.3906/tar-1805-5

Zhu, Y., Liu, K., Myint, S. W., Du, Z., Li, Y., Cao, J., Liu, L., & Wu, Z. (2020). Integration of GF2 optical, GF3 SAR, and UAV data for estimating aboveground biomass of China's largest artificially planted mangroves. *Remote Sensing*, *12*(12). https://doi.org/10.3390/RS12122039

Zianis, D., Muukkonen, P., Mäkipää, R., & Mencuccini, M. (2005). Biomass and stem volume equations for tree species in Europe. *Silva Fennica Monographs*, *4*, 1–63. https://silvafennica.fi/pdf/smf004.pdf

APPENDICES

Appendix A: Field data collection datasheet.

Datasheet for forest tree parameters in Haagse bos								
Observer name:				Date		Plot #:		
Central point		Longitude (X):			Latitude (Y):			
Plot radius:		Plot dominant species:						
Forest density:				Closed / Medium / Open				
Canopy Closure (%)		Centre:	North:	South:		East:		West:
General comment:								
Tree #	Species	DBH (cm)	Height (m)	Crown diameter (m)		Tree position		Comment
				N-S	E-W	Distance from centre point (m)	North bearing (degrees)	

Appendix B: Quality report of UAV RGB image processing of Block 2 and Block 3.

Quality Report

Generated with Pix4Dmapper version 4.5.6

Important: Click on the different icons for:

Help to analyze the results in the Quality Report

Additional information about the sections

Click here for additional tips to analyze the Quality Report

Summary

Project	B45
Processed	2020-09-29 10:58:03
Camera Model Name(s)	FC330_3.6_4000x3000 (RGB)
Average Ground Sampling Distance (GSD)	4.49 cm / 1.77 in
Area Covered	0.575 km^2 / 57.5429 ha / 0.22 sq. mi. / 142.2651 acres
Time for Initial Processing (without report)	53m:49s

Quality Check

Images	median of 58179 keypoints per image	
Dataset	1470 out of 1470 images calibrated (100%), all images enabled	
Camera Optimization	0% relative difference between initial and optimized internal camera parameters	
Matching	median of 5730.64 matches per calibrated image	
Georeferencing	yes, 9 GCPs (9 3D), mean RMS error = 0.011 m	

Preview

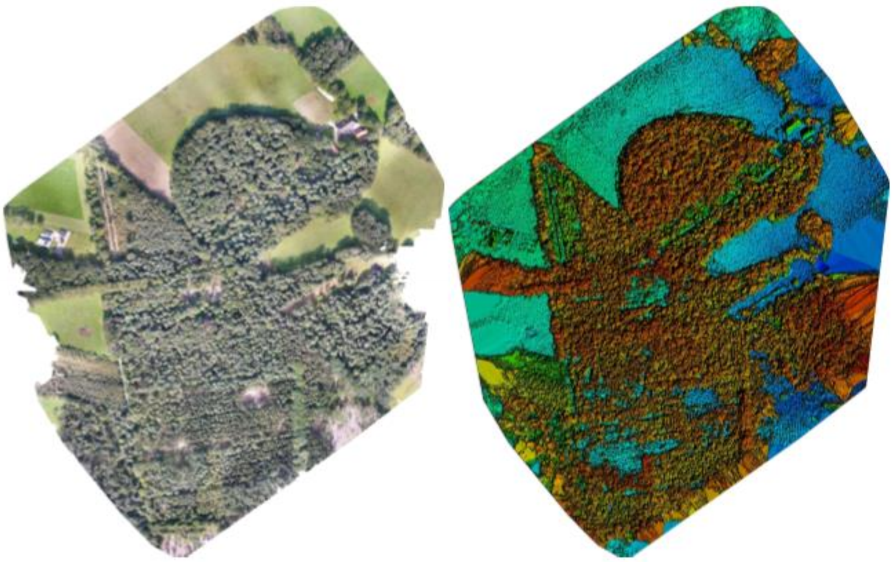

Figure 1: Orthomosaic and the corresponding sparse Digital Surface Model (DSM) before densification.

Calibration Details

Number of Calibrated Images	1470 out of 1470
Number of Geolocated Images	1470 out of 1470

Initial Image Positions

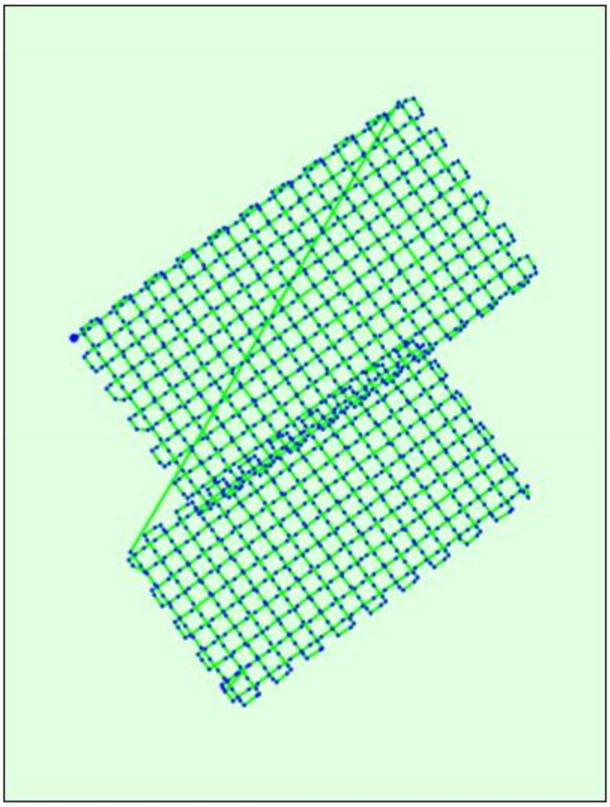

Figure 2: Top view of the initial image position. The green line follows the position of the images in time starting from the large blue dot.

Computed Image/GCPs/Manual Tie Points Positions

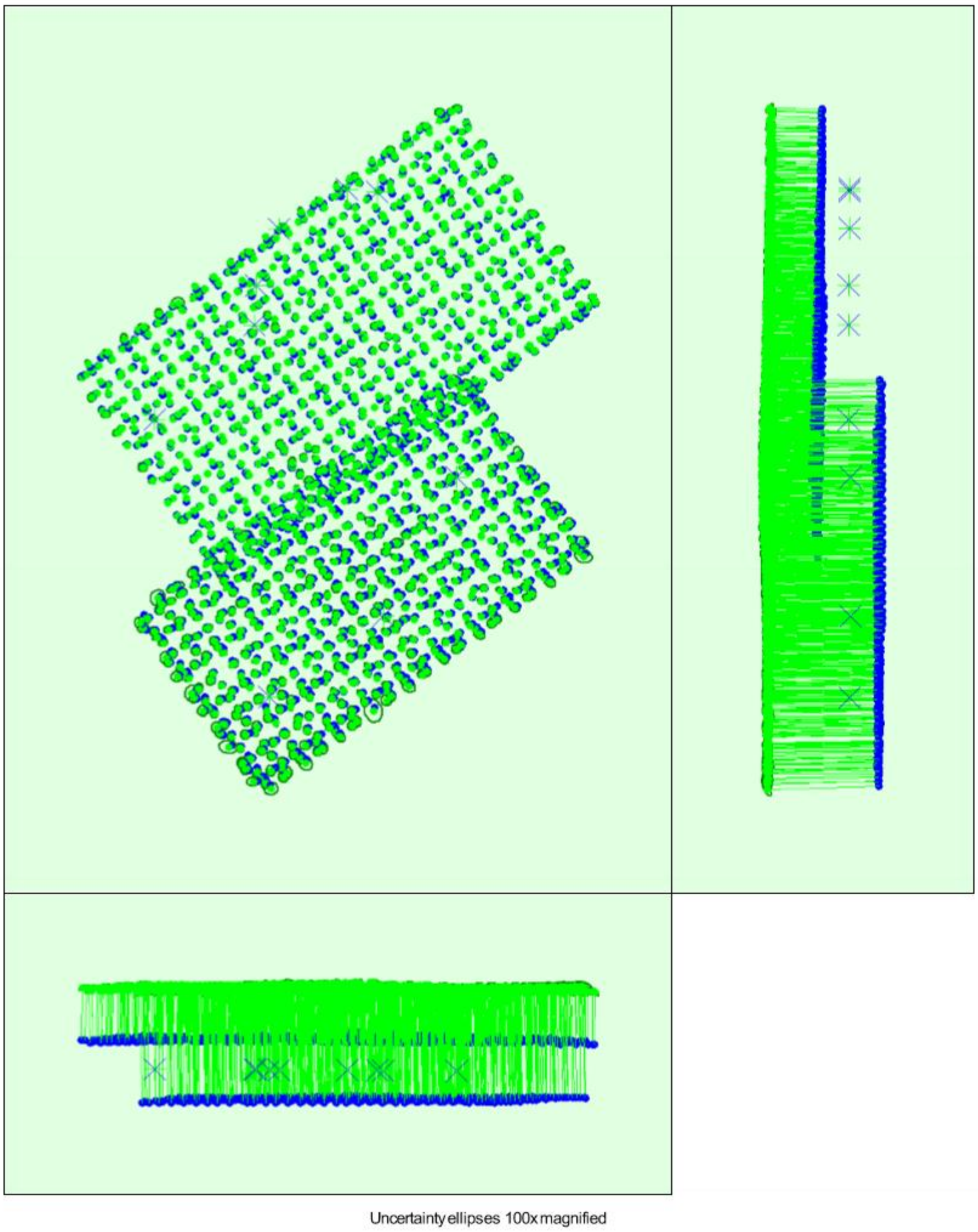

Figure 3: Offset between initial (blue dots) and computed (green dots) image positions as well as the offset between the GCPs initial positions (blue crosses) and their computed positions (green crosses) in the top-view (XY plane), front-view (XZ plane), and side-view (YZ plane). Dark green ellipses indicate the absolute position uncertainty of the bundle block adjustment result.

Absolute camera position and orientation uncertainties

	X[m]	Y[m]	Z[m]	Omega [degree]	Phi [degree]	Kappa [degree]
Mean	0.042	0.042	0.039	0.021	0.021	0.008
Sigma	0.012	0.013	0.006	0.007	0.007	0.003

Overlap

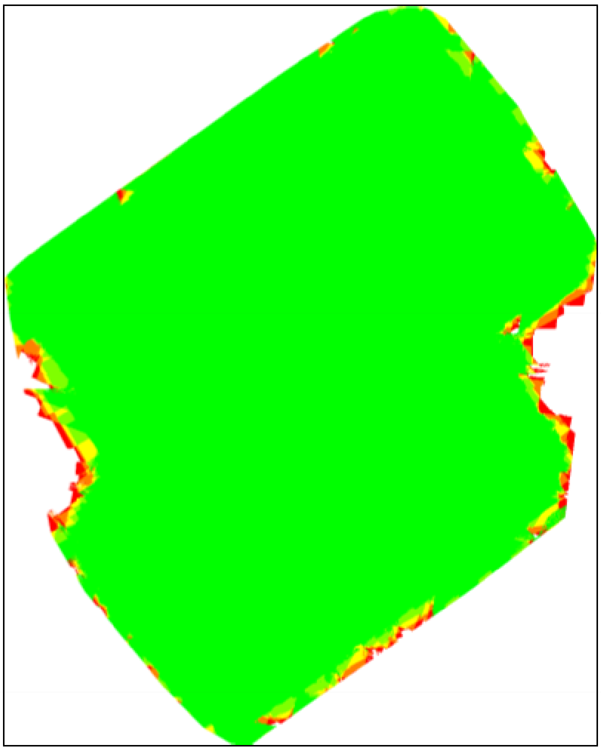

Figure 4: Number of overlapping images computed for each pixel of the orthomosaic.
Red and yellow areas indicate low overlap for which poor results may be generated. Green areas indicate an overlap of over 5 images for every pixel. Good quality results will be generated as long as the number of keypoint matches is also sufficient for these areas (see Figure 5 for keypoint matches).

Bundle Block Adjustment Details

Number of 2D Keypoint Observations for Bundle Block Adjustment	9028785
Number of 3D Points for Bundle Block Adjustment	3255308
Mean Reprojection Error [pixels]	0.246

Internal Camera Parameters

FC330_3.6_4000x3000 (RGB). Sensor Dimensions: 6.317 [mm] x 4.738 [mm]

EXIF ID: FC330_3.6_4000x3000

	Focal Length	Principal Point x	Principal Point y	R1	R2	R3	T1	T2
Initial Values	2285.722 [pixel] 3.610 [mm]	2000.006 [pixel] 3.159 [mm]	1500.003 [pixel] 2.369 [mm]	-0.001	-0.002	0.000	-0.001	-0.001
Optimized Values	2285.760 [pixel] 3.610 [mm]	1976.929 [pixel] 3.122 [mm]	1449.416 [pixel] 2.289 [mm]	0.004	-0.012	0.006	-0.000	-0.000
Uncertainties (Sigma)	0.633 [pixel] 0.001 [mm]	0.108 [pixel] 0.000 [mm]	0.105 [pixel] 0.000 [mm]	0.000	0.000	0.000	0.000	0.000

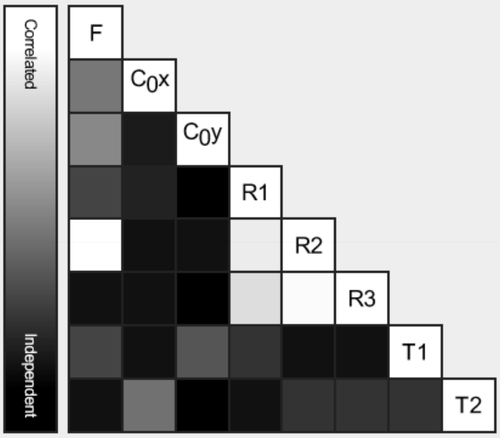

The correlation between camera internal parameters determined by the bundle adjustment. White indicates a full correlation between the parameters, ie. any change in one can be fully compensated by the other. Black indicates that the parameter is completely independent, and is not affected by other parameters.

The number of Automatic Tie Points (ATPs) per pixel, averaged over all images of the camera model, is color coded between black and white. White indicates that, on average, more than 16 ATPs have been extracted at the pixel location. Black indicates that, on average, 0 ATPs have been extracted at the pixel location. Click on the image to the see the average direction and magnitude of the re-projection error for each pixel. Note that the vectors are scaled for better visualization. The scale bar indicates the magnitude of 1 pixel error.

2D Keypoints Table

	Number of 2D Keypoints per Image	Number of Matched 2D Keypoints per Image
Median	58179	5731
Min	21009	474
Max	70560	14175
Mean	55103	6142

3D Points from 2D Keypoint Matches

	Number of 3D Points Observed
In 2 Images	2375288
In 3 Images	458351
In 4 Images	165227
In 5 Images	79996
In 6 Images	46345
In 7 Images	31095
In 8 Images	20009
In 9 Images	14691
In 10 Images	11181
In 11 Images	8733
In 12 Images	6855
In 13 Images	5636
In 14 Images	4413
In 15 Images	3617
In 16 Images	2933
In 17 Images	2541
In 18 Images	2124
In 19 Images	1807
In 20 Images	1563
In 21 Images	1448
In 22 Images	1272

In 23 Images	1055
In 24 Images	981
In 25 Images	825
In 26 Images	739
In 27 Images	673
In 28 Images	626
In 29 Images	502
In 30 Images	498
In 31 Images	500
In 32 Images	370
In 33 Images	353
In 34 Images	281
In 35 Images	259
In 36 Images	240
In 37 Images	220
In 38 Images	211
In 39 Images	184
In 40 Images	172
In 41 Images	150
In 42 Images	131
In 43 Images	146
In 44 Images	109
In 45 Images	109
In 46 Images	80
In 47 Images	81
In 48 Images	67
In 49 Images	64
In 50 Images	53
In 51 Images	58
In 52 Images	60
In 53 Images	44
In 54 Images	37
In 55 Images	48
In 56 Images	32
In 57 Images	28
In 58 Images	26
In 59 Images	16
In 60 Images	30
In 61 Images	12
In 62 Images	13
In 63 Images	16
In 64 Images	13
In 65 Images	12
In 66 Images	6
In 67 Images	11
In 68 Images	4
In 69 Images	4
In 70 Images	8
In 71 Images	5
In 72 Images	4
In 73 Images	5
In 74 Images	2
In 76 Images	3
In 77 Images	2
In 78 Images	2
In 83 Images	1
In 85 Images	1
In 86 Images	1

2D Keypoint Matches

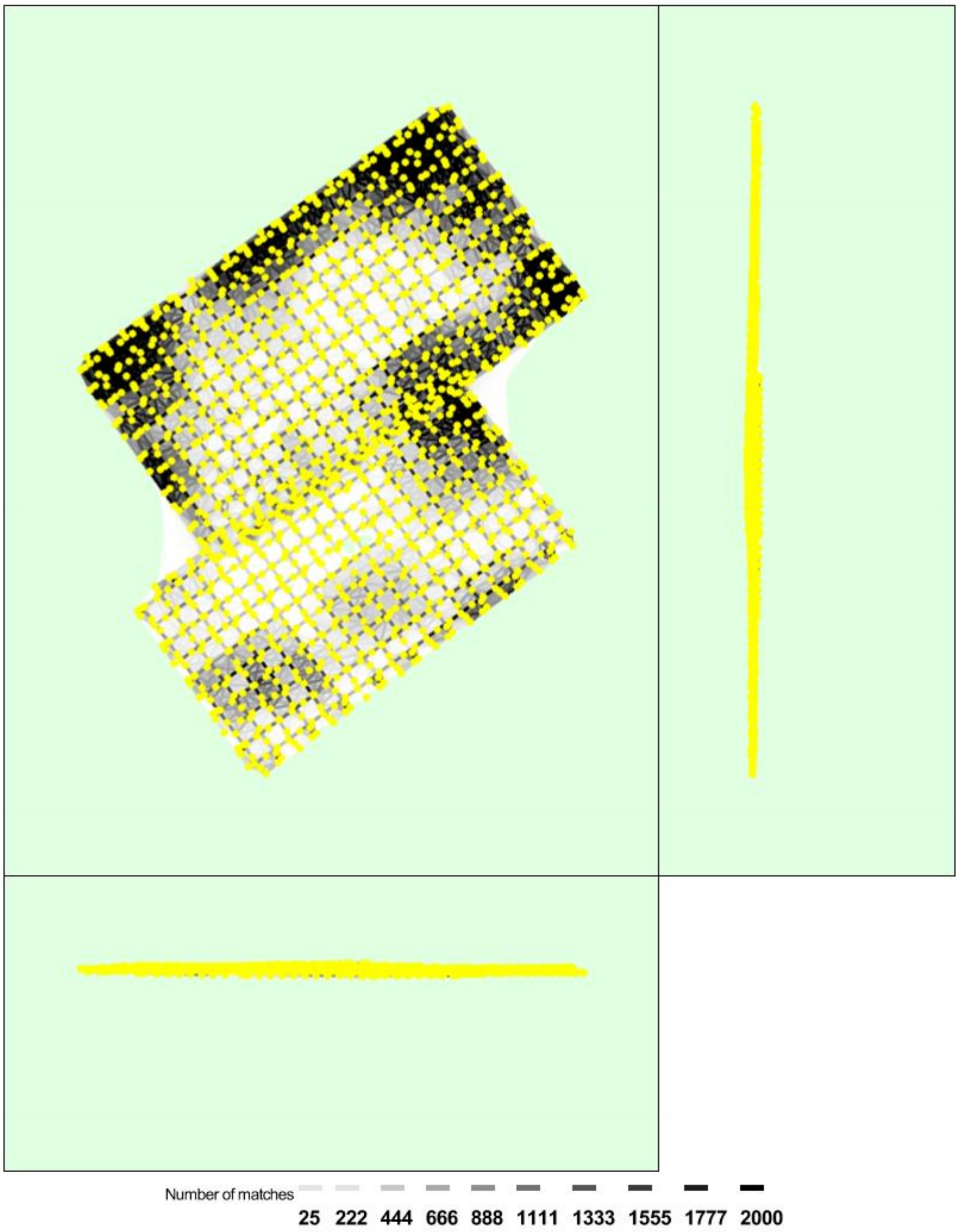

Figure 5: Computed image positions with links between matched images. The darkness of the links indicates the number of matched 2D keypoints between the images. Bright links indicate weak links and require manual tie points or more images.

Geolocation Details

Ground Control Points

GCP Name	Accuracy XY/Z [m]	Error X [m]	Error Y [m]	Error Z [m]	Projection Error [pixel]	Verified/Marked
GCP0002 (3D)	0.020/ 0.020	-0.010	0.021	0.010	0.634	25 / 25
GCP0004 (3D)	0.020/ 0.020	-0.016	-0.007	0.008	0.713	21 / 21
GCP0009 (3D)	0.020/ 0.020	0.032	0.023	-0.003	0.764	45 / 48
GCP0010 (3D)	0.020/ 0.020	0.002	-0.016	0.000	0.584	40 / 41
GCP0011 (3D)	0.020/ 0.020	0.006	-0.007	0.002	0.927	32 / 33
GCP0012 (3D)	0.020/ 0.020	0.005	0.003	-0.001	0.912	28 / 28
GCP0013 (3D)	0.020/ 0.020	0.008	-0.021	-0.005	0.986	21 / 21
GCP0014 (3D)	0.020/ 0.020	-0.001	0.009	-0.002	0.769	51 / 51
GCP0015 (3D)	0.020/ 0.020	-0.025	-0.007	-0.005	0.855	59 / 59
Mean [m]		-0.000025	-0.000158	0.000521		
Sigma [m]		0.015462	0.014713	0.005051		
RMS Error [m]		0.015462	0.014713	0.005078		

0 out of 4 check points have been labeled as inaccurate.

Check Point Name	Accuracy XY/Z [m]	Error X [m]	Error Y [m]	Error Z [m]	Projection Error [pixel]	Verified/Marked
GCP0001		-0.0071	-0.0297	-0.0372	0.7465	6 / 6
GCP0003		-0.0303	0.0048	0.0017	0.6021	18 / 18
GCP0006		0.0732	0.0581	0.1026	1.0878	23 / 24
GCP0007		0.0649	0.0568	0.0189	1.2451	23 / 25
Mean [m]		0.025160	0.022507	0.021522		
Sigma [m]		0.044711	0.037001	0.051013		
RMS Error [m]		0.051304	0.043308	0.055368		

Localisation accuracy per GCP and mean errors in the three coordinate directions. The last column counts the number of calibrated images where the GCP has been automatically verified vs. manually marked.

Absolute Geolocation Variance

Min Error [m]	Max Error [m]	Geolocation Error X [%]	Geolocation Error Y [%]	Geolocation Error Z [%]
-	-15.00	0.00	0.00	44.01
-15.00	-12.00	0.00	0.00	0.00
-12.00	-9.00	0.00	0.00	0.00
-9.00	-6.00	0.00	0.07	0.00
-6.00	-3.00	6.05	11.56	0.00
-3.00	0.00	45.85	36.60	0.00
0.00	3.00	42.11	41.56	0.00
3.00	6.00	5.99	10.07	0.00
6.00	9.00	0.00	0.14	0.00
9.00	12.00	0.00	0.00	0.00
12.00	15.00	0.00	0.00	0.00
15.00	-	0.00	0.00	55.99
Mean [m]		1.048167	0.135834	-100.984718
Sigma [m]		1.925558	2.369330	38.494397
RMS Error [m]		2.192356	2.373220	108.072808

Min Error and Max Error represent geolocation error intervals between -1.5 and 1.5 times the maximum accuracy of all the images. Columns X, Y, Z show the percentage of images with geolocation errors within the predefined error intervals. The geolocation error is the difference between the initial and computed image positions. Note that the image geolocation errors do not correspond to the accuracy of the observed 3D points.

Geolocation Bias	X	Y	Z
Translation [m]	1.048167	0.135834	-100.984718

Bias between image initial and computed geolocation given in output coordinate system.

Relative Geolocation Variance

Relative Geolocation Error	Images X [%]	Images Y [%]	Images Z [%]
[-1.00, 1.00]	99.39	97.21	0.00
[-2.00, 2.00]	100.00	100.00	0.00
[-3.00, 3.00]	100.00	100.00	0.00
Mean of Geolocation Accuracy [m]	5.000000	5.000000	10.000000
Sigma of Geolocation Accuracy [m]	0.000000	0.000000	0.000000

Images X, Y, Z represent the percentage of images with a relative geolocation error in X, Y, Z.

Geolocation Orientational Variance	RMS [degree]
Omega	0.320
Phi	0.323
Kappa	4.148

Geolocation RMS error of the orientation angles given by the difference between the initial and computed image orientation angles.

Initial Processing Details

System Information

Hardware	CPU: Intel(R) Core(TM) i7-9750H CPU @ 2.60GHz RAM: 16GB GPU: Intel(R) UHD Graphics 630 (Driver: 26.20.100.7811), NVIDIA Quadro T1000 (Driver: 26.21.14.3213)
Operating System	Windows 10 Home, 64-bit

Coordinate Systems

Image Coordinate System	WGS 84 (EGM96 Geoid)
Ground Control Point (GCP) Coordinate System	Amersfoort / RD New (EGM96 Geoid)
Output Coordinate System	Amersfoort / RD New (EGM96 Geoid)

Processing Options

Detected Template	No Template Available
Keypoints Image Scale	Full, Image Scale: 1
Advanced: Matching Image Pairs	Aerial Grid or Corridor
Advanced: Matching Strategy	Use Geometrically Verified Matching: yes
Advanced: Keypoint Extraction	Targeted Number of Keypoints: Automatic
Advanced: Calibration	Calibration Method: Standard Internal Parameters Optimization: All prior External Parameters Optimization: All Rematch: Auto, no

Point Cloud Densification details

Processing Options

Image Scale	multiscale, 1/2 (Half image size, Default)
Point Density	Optimal
Minimum Number of Matches	3
3D Textured Mesh Generation	yes
3D Textured Mesh Settings:	Resolution: Medium Resolution (default) Color Balancing: no

LOD	Generated: no
Advanced: 3D Textured Mesh Settings	Sample Density Divider: 1
Advanced: Image Groups	group1
Advanced: Use Processing Area	yes
Advanced: Use Annotations	yes
Time for Point Cloud Densification	05h:35m:29s
Time for Point Cloud Classification	NA
Time for 3D Textured Mesh Generation	02h:10m:17s

Results

Number of Processed Clusters	4
Number of Generated Tiles	4
Number of 3D Densified Points	78684624
Average Density (per m^3)	49.72

DSM, Orthomosaic and Index Details

Processing Options

DSM and Orthomosaic Resolution	1 x GSD (4.49 [cm/pixel])
DSM Filters	Noise Filtering: yes Surface Smoothing: yes, Type: Sharp
Raster DSM	Generated: yes Method: Inverse Distance Weighting Merge Tiles: yes
Orthomosaic	Generated: yes Merge Tiles: yes GeoTIFF Without Transparency: no Google Maps Tiles and KML: no
Time for DSM Generation	56m:33s
Time for Orthomosaic Generation	02h:17m:23s
Time for DTM Generation	00s
Time for Contour Lines Generation	00s
Time for Reflectance Map Generation	00s
Time for Index Map Generation	00s

Appendix C: HV and HH backscatter/NRCS retrieval in dB using Equation 1 in SNAP Software.

Appendix D: Relationship between UAV AGB and Biometric AGB on plot for Conifers, Broadleaves, and Mixed forest stand.

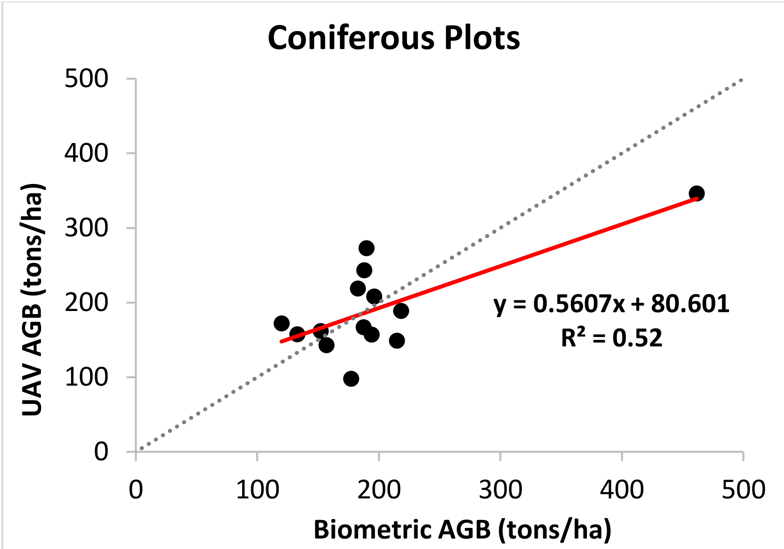

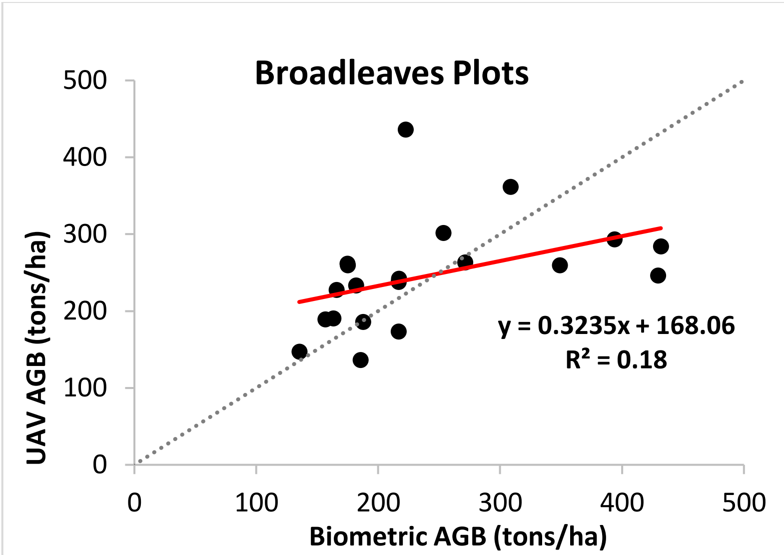

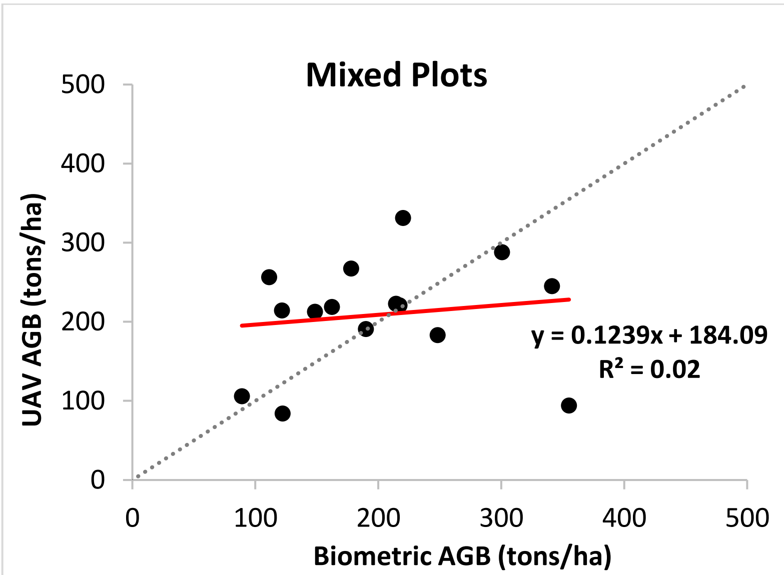

Appendix E: Summary of T-test between CPA-DBH modeled DBH and field-measured DBH.

t-Test: Two-Sample Assuming Unequal Variances

	Biometric DBH	Estimated DBH
Mean	49.0	51.2
Variance	241.36	115.26
Observations	117	117
Hypothesized Mean Difference	0	
df	206	
t Stat	-1.304	
P(T<=t) one-tail	0.097	
t Critical one-tail	1.652	
P(T<=t) two-tail	0.194	
t Critical two-tail	1.972	

Appendix F: Summary statistics of regression between HH backscatter coefficients and field AGB.

SUMMARY OUTPUT

Regression Statistics	
Multiple R	0.65
R Square	0.43
Adjusted R Square	0.42
Standard Error	70.80
Observations	83

ANOVA

	df	SS	MS	F	Significance F
Regression	1	303944.80	303944.80	60.63	1.97698E-11
Residual	81	406077.34	5013.30		
Total	82	710022.14			

	Coefficients	Standard Error	t Stat	P-value
Intercept	513.60	40.25	12.76	4.44154E-21
HH Backscatter	36.74	4.72	7.79	1.98E-11

Appendix G: Summary statistics of regression between HH backscatter coefficients and $\log_{10}$(AGB).

Regression Statistics	
Multiple R	0.69
R Square	0.47
Adjusted R Square	0.47
Standard Error	0.12
Observations	83

ANOVA

	df	*SS*	*MS*	*F*	*Significance F*
Regression	1	1.13	1.13	72.82	6.65521E-13
Residual	81	1.26	0.02		
Total	82	2.39			

	Coefficients	*Standard Error*	*t Stat*	*P-value*
Intercept	2.87	0.07	40.55	1.44775E-55
HH Backscatter	0.07	0.01	8.53	6.65521E-13

Appendix H: Summary statistics of regression between HV backscatter coefficients and field AGB.

SUMMARY OUTPUT

Regression Statistics	
Multiple R	0.86
R Square	0.74
Adjusted R Square	0.73
Standard Error	47.98
Observations	83

ANOVA

	df	SS	MS	F	Significance F
Regression	1	523585.78	523585.78	227.48	3.0948E-25
Residual	81	186436.35	2301.68		
Total	82	710022.14			

	Coefficients	Standard Error	t Stat	P-value
Intercept	990.06	52.24	18.95	1.65166E-31
HV_Backscatter	59.16	3.92	15.08	3.0948E-25

Appendix I: Summary statistics of regression between HV backscatter coefficients and $\log_{10}$(AGB).

Regression Statistics	
Multiple R	0.91
R Square	0.84
Adjusted R Square	0.83
Standard Error	0.07
Observations	83

ANOVA

	df	SS	MS	F	Significance F
Regression	1	2.00	2.00	415.19	1.2704E-33
Residual	81	0.39	0.005		
Total	82	2.39			

	Coefficients	Standard Error	t Stat	P-value
Intercept	3.81	0.08	50.44	5.92928E-63
HV_Backscatter	0.12	0.01	20.38	1.2704E-33

Appendix J: Summary statistics of regression between HV backscatter modeled AGB and the field AGB.

Regression Statistics	
Multiple R	0.93
R Square	0.86
Adjusted R Square	0.85
Standard Error	27.48
Observations	33

ANOVA

	df	SS	MS	F	Significance F
Regression	1	142929.77	142929.77	189.32	9.60026E-15
Residual	31	23403.71	754.96		
Total	32	166333.48			

	Coefficients	Standard Error	t Stat	P-value
Intercept	52.80	11.52	4.58	7.06425E-05
Biometric AGB	0.75	0.05	13.76	9.60026E-15

Appendix K: Summary of T-test between UAV modeled AGB and field-measured AGB on plots.

t-Test: Two-Sample Assuming Unequal Variances

	UAV AGB	Biometric AGB
Mean	227.83	266.85
Variance	5853.08	15864.44
Observations	57	57
Hypothesized Mean Difference	0	
df	92	
t Stat	-1.999	
P(T<=t) one-tail	0.024	
t Critical one-tail	1.662	
P(T<=t) two-tail	0.049	
t Critical two-tail	1.986	

Appendix L: Summary statistics of regression analysis between UAV modeled plot AGB and field-measured plot AGB for coniferous, broadleaves, and mixed forest stand.

(a) Summary statistics of regression analysis between UAV modeled plot AGB and field-measured plot AGB on coniferous forest plots.

SUMMARY OUTPUT

Regression Statistics	
Multiple R	0.68
R Square	0.46
Adjusted R Square	0.42
Standard Error	60.82
Observations	15

ANOVA

	df	SS	MS	F	Significance F
Regression	1	40666.81	40666.81	10.99	0.01
Residual	13	48095.75	3699.67		
Total	14	88762.56			

	Coefficients	Standard Error	t Stat	P-value
Intercept	23.07	53.84	0.43	0.68
X Variable 1	0.88	0.27	3.32	0.01

(b) Summary statistics of regression analysis between UAV modeled plot AGB and field-measured plot AGB on coniferous forest plots.

SUMMARY OUTPUT

Regression Statistics	
Multiple R	0.63
R Square	0.40
Adjusted R Square	0.37
Standard Error	102.91
Observations	24

ANOVA

	df	SS	MS	F	Significance F
Regression	1	155014.51	155014.51	14.64	0.00
Residual	22	233012.60	10591.48		
Total	23	388027.11			

	Coefficients	Standard Error	t Stat	P-value
Intercept	20.99	82.08	0.26	0.80
X Variable 1	1.21	0.32	3.83	0.00

(c) Summary statistics of regression analysis between UAV modeled plot AGB and field-measured plot AGB on coniferous forest plots.

SUMMARY OUTPUT

Regression Statistics	
Multiple R	0.37
R Square	0.14
Adjusted R Square	0.08
Standard Error	115.48
Observations	18

ANOVA

	df	SS	MS	F	Significance F
Regression	1	33720.83	33720.83	2.53	0.13
Residual	16	213386.51	13336.66		
Total	17	247107.34			

	Coefficients	Standard Error	t Stat	P-value
Intercept	139.60	75.05	1.86	0.08
X Variable 1	0.49	0.31	1.59	0.13